



University of Tennessee, Knoxville
**TRACE: Tennessee Research and Creative
Exchange**

Doctoral Dissertations

Graduate School

5-2023

Measurement-Based Monitoring and Control in Power Systems with High Renewable Penetrations

Chengwen Zhang

University of Tennessee, Knoxville, czhang70@vols.utk.edu

Follow this and additional works at: https://trace.tennessee.edu/utk_graddiss



Part of the [Power and Energy Commons](#)

Recommended Citation

Zhang, Chengwen, "Measurement-Based Monitoring and Control in Power Systems with High Renewable Penetrations." PhD diss., University of Tennessee, 2023.

https://trace.tennessee.edu/utk_graddiss/8131

This Dissertation is brought to you for free and open access by the Graduate School at TRACE: Tennessee Research and Creative Exchange. It has been accepted for inclusion in Doctoral Dissertations by an authorized administrator of TRACE: Tennessee Research and Creative Exchange. For more information, please contact trace@utk.edu.

To the Graduate Council:

I am submitting herewith a dissertation written by Chengwen Zhang entitled "Measurement-Based Monitoring and Control in Power Systems with High Renewable Penetrations." I have examined the final electronic copy of this dissertation for form and content and recommend that it be accepted in partial fulfillment of the requirements for the degree of Doctor of Philosophy, with a major in Electrical Engineering.

Yilu Liu, Major Professor

We have read this dissertation and recommend its acceptance:

Yilu Liu, Leon Tolbert, Fangxing Li, Lin Zhu

Accepted for the Council:

Dixie L. Thompson

Vice Provost and Dean of the Graduate School

(Original signatures are on file with official student records.)

**Measurement-Based Monitoring and Control in Power
Systems with High Renewable Penetrations**

A Dissertation Presented for the

Doctor of Philosophy

Degree

The University of Tennessee, Knoxville

Chengwen Zhang

May 2023

Copyright © 2023 by Chengwen Zhang

All rights reserved.

To my wife and my parents

ACKNOWLEDGMENTS

Pursuing my Ph.D. in the U.S. has been a joyful experience that opened my mind to infinite possibilities. I deeply appreciate the wonderful people around me who helped me through this journey.

First, I would like to acknowledge my advisor, Dr. Yilu Liu, without whom this adventure would not have been possible. I am fortunate to have her endless support and invaluable guidance. Her curious, honest, and insightful approach toward research is my lifetime inspiration, for which I will be forever grateful.

I would like to thank Dr. Leon Tolbert, Dr. Lin Zhu, and Dr. Fangxing Li, who served on my committee and guided me with patience, principles, and thoughtfulness throughout the years of my Ph.D. studies. I would like to also thank Dr. Fred Wang for his advice on microgrid controls and Dr. Mark Baldwin for his knowledge and curiosity in our exploration of large interconnection frequency dynamics.

I am grateful to have my fellow graduate students, researchers, and friends during these years. The time we spent together working, talking, hiking, and exploring, will be my wholeheartedly cherished memories.

With my deepest love and appreciation, I would like to thank my wife, Dr. Saier Li, my parents, Chenguang Zhang and Xiaohong Zheng, and my sister, Chengle Zhang, for their unconditional love and unwavering support.

ABSTRACT

Power systems are experiencing rapid changes in their generation mixes because of the increasing integration of inverter-based resources (IBRs) and the retirement of traditional generations. This opens opportunities for a cleaner energy outlook but also poses challenges to the safe operation of the power networks. Enhanced monitoring and control based on the increasingly available measurements are essential in assisting stable operation and effective planning for these evolving systems.

First, awareness of the evolving dynamic characteristics is quintessential for secure operation and corrective planning. A quantified monitoring study that keeps track of the inertial response and primary frequency response is conducted on the Eastern Interconnection (EI) for the past decade with field data. Whereas the inertia declined by at least 10%, the primary frequency response experienced an unexpected increase. The findings unveiled in the trending analysis also led to an improved event MW size estimation method, as well as discussions about regional dynamics.

Experiencing a faster and deeper renewable integration, the Continental Europe Synchronous Area (CESA) system has been threatened by more frequent occurrences of inter-area oscillations during light-load high-renewable periods. A measurement-based oscillation damping control scheme is proposed for CESA with reduced reliance on system models. The design, implementation, and hardware-in-the-loop (HIL) testing of the controller are discussed in detail.

Despite the challenges, the increasing presence of IBRs also brings opportunities for fast and efficient controls. Together with synchronized measurement, IBRs have the potential to flexibly complement traditional frequency and voltage control schemes for

improved frequency and voltage recovery. The design, implementation, and HIL testing of the measurement-based frequency and voltage control for the New York State Grid are presented.

In addition to the transmission level development, IBRs deployed in distribution networks can also be valuable assets in emergency islanding situations if controlled properly. A power management module is proposed to take advantage of measurements and automatically control the electric boundaries of islanded microgrids for maximized power utilization and improved frequency regulation. The module is designed to be adaptive to arbitrary non-meshed topologies with multiple source locations for increased flexibility, expedited deployment, and reduced cost.

TABLE OF CONTENTS

Chapter 1. Introduction	1
1.1 Background and Motivation	1
1.2 Dissertation Outline	5
Chapter 2. Monitoring the Trends of Inertia and Primary Frequency Response	7
2.1 Introduction.....	7
2.1.1 Background and Motivation	7
2.1.2 Power System Frequency Response – Time Scale of Interest.....	12
2.1.3 Estimation of Power System Inertia	13
2.1.4 Estimation of Primary Frequency Response.....	18
2.2 Data Sources and Preprocessing	18
2.2.1 FNET/GridEye.....	18
2.2.2 NERC Registry with Confirmed MW information.....	22
2.2.3 Data Preprocessing.....	22
2.3 Trend Analysis of Inertia	25
2.3.1 Considerations for the RoCoF and inertia calculation.....	25
2.3.2 Inertia Trend Results.....	30
2.4 Trend Analysis of Primary Frequency Response.....	32
2.4.1 Basics of the Calculation of Primary Frequency Response	34
2.4.2 Impact of Governor Dead-Bands and Event Specifications	35
2.4.3 Trends of Primary Frequency Response with Event Filters	46
2.4.4 Explanation for the Increase In Primary Frequency Response	48
2.5 Improved Event MW Estimation	50

2.5.1 Overview	52
2.5.2 Formulation of the MW Estimation Problem	53
2.5.3 Solving MW Estimation Equations	56
2.5.4 EI Case Study and Performance Comparison	57
2.6 Regional Frequency Dynamics	61
2.6.1 Purpose of Regional Dynamics Studies	61
2.6.2 Regional Dynamics in EI	62
2.6.3 Summary of Regional Dynamics in EI	81
2.7 Summary	83
Chapter 3. Measurement-based Wide-Area Damping Control – TERNA Case Study	86
3.1 Introduction	86
3.2 Design of the Wide-Area Damping Scheme	90
3.2.1 Choice of Control Input	90
3.2.2 Choice of Control Actuators	92
3.2.3 Design of the Wide-Area Damping Controller Parameters	92
3.3 Hardware Implementation of the WADC and the HIL Platform	96
3.3.1 Overview of the Hardware-in-the-Loop (HIL) Platform	96
3.3.2 Hardware Implementation of the Controller	98
3.3.3 Real-Time Simulation of the Continental Europe Synchronous Area... ..	102
3.4 Hardware-in-the-Loop Testing Results	106
3.4.1 Case 1: Base Case	109
3.4.2 Case 2: Constant Time Delay	109
3.4.3 Case 3: Random Time Delay	112

3.4.4 Case 4: Random Data Drop	114
3.4.5 Case 5: Chunk Data Loss and Supervisory Control.....	114
3.4.6 Case 6: Comparison of TCP and UDP.....	116
3.5 Summary	121
Chapter 4. Measurement-Based Voltage and Frequency Control with IBRs	122
4.1 Introduction.....	122
4.1.1 Hierarchical-Local Frequency Control	122
4.1.2 Gradient-Based Voltage Control.....	126
4.2 Implementation of the Control Schemes on Hardware.....	128
4.2.1 Hardware Implementation of the Controllers	128
4.2.2 Real-time Simulation of the 5000-bus New York State Grid	128
4.3 Hardware-in-the-Loop Testing Results.....	137
4.3.1 Frequency Control	137
4.3.2 Voltage Control.....	143
4.4 Summary	146
Chapter 5. Measurement-Based Real-Time Power Management for Microgrids with Dynamic Boundaries.....	149
5.1 Introduction.....	149
5.2 Structure of the Flexible Microgrid Controller.....	153
5.3 The Power Management Module.....	157
5.3.1 Structure of the Power Management Module	157
5.3.2 Dynamic Boundary Algorithms for Arbitrary Topologies	160
5.3.3 Power Sharing and Secondary Frequency Regulation.....	170

5.3.4 Extreme Power Imbalance Conditions.....	173
5.4 Testing Platform and Results	174
5.4.1 Converter-based Hardware Testbed (HTB).....	174
5.4.2 Testing Scenarios and Results	179
5.5 Summary	189
Chapter 6. Conclusions and Future Work.....	191
6.1 Conclusions.....	191
6.2 Future work.....	194
References.....	196
Vita.....	202

LIST OF TABLES

Table 2-1 Correlation coefficients between MW and RoCoF	31
Table 2-2 Changes in Generation of Coal, Gas, Solar, and Wind	51
Table 2-3 Curve-fitting results for EI with FNET/GridEye data	58
Table 2-4 MW estimation accuracy of different estimation methods.....	60
Table 2-5 Frequency dynamic specifics from the event in Florida	65
Table 2-6 Frequency dynamic specifics from the event in Southeast U.S.	68
Table 2-7 Frequency dynamic specifics from the event in the Mid-Atlantic	70
Table 2-8 Frequency dynamic specifics from the event in Northeastern U.S.	72
Table 2-9 Frequency dynamic specifics from the event in Midwest U.S.	74
Table 2-10 Frequency dynamic specifics from the event in West Central U.S.....	75
Table 2-11 Frequency dynamic specifics from the event in Central Southeast U.S.....	77
Table 2-12 Frequency dynamic specifics from the event in Upper Midwest U.S.....	78
Table 2-13 Frequency dynamic specifics from the event in West South Central U.S.....	80
Table 2-14 Specifications of the sample events across EI.....	82
Table 3-1 FFT Magnitude at the mode of interest	91
Table 3-2 Comparison of power flow solutions in OPAL-RT and PSS/e	105
Table 3-3 Comparison of oscillation frequency and damping ratio	108
Table 3-4 Testing cases conducted on the HIL platform.....	108
Table 3-5 Comparison of damping ratios before and after the application of WADC...	110
Table 4-1 Comparison of power flow results in OPAL-RT and PSS/E	132
Table 4-2 Closed-loop IBR response and communication delay.....	136
Table 4-3 IBRs in Areas I, J, and K.....	138

Table 4-4 IBR active power output in the 300 MW disturbance testing	140
Table 4-5 IBR active power output in the 800 MW disturbance testing	142
Table 5-1 Format of a topology matrix of a controllable area	165

LIST OF FIGURES

Figure 2-1 Typical primary frequency response and power contribution [26].....	14
Figure 2-2 Measurement of primary frequency response [26]	19
Figure 2-3 Deployment of FNET/GridEye Sensors.....	21
Figure 2-4 Generation trip event in Florida	24
Figure 2-5 Comparison of regional and interconnection frequency dynamics.....	27
Figure 2-6 Plot of RoCoF against MW for events in the year 2020	29
Figure 2-7 Mean and SD of the correlation coefficient with different RoCoF windows .	31
Figure 2-8 Trend of inertia in Eastern Interconnection from 2012 to 2021.....	33
Figure 2-9 Dead-bands and event frequency dynamics	36
Figure 2-10 Primary frequency response in consecutive generation trip events	38
Figure 2-11 Beta Trends from 2012 to 2021 calculated with all events	41
Figure 2-12 Boxplot of β values of individual events from 2012 to 2021	41
Figure 2-13 The $MW - \Delta f$ plot of events in year 2020.....	42
Figure 2-14 Correlation coefficient between MW and Δf	42
Figure 2-15 Plot of event β against starting frequency and MW size	44
Figure 2-16 Correlation coefficient – events with near nominal f_s	47
Figure 2-17 The trend of primary frequency response β_0	47
Figure 2-18 Correlation coefficient – events with low f_s	49
Figure 2-19 The trend of primary frequency response $\beta +$	49
Figure 2-20 Generation in Eastern Interconnection by fuel types	51
Figure 2-21 Relationship between β and starting frequency	54
Figure 2-22 Relationship between β and event MW size.....	54

Figure 2-23 Multiple roots to the auxiliary function	58
Figure 2-24 Comparison of the fitted curves of different orders	60
Figure 2-25 Location of the generation trip event in Florida.....	64
Figure 2-26 Frequency measurements captured by sensors in EI.....	64
Figure 2-27 Frequency deviations in Florida and Southeast following a FL disturbance	65
Figure 2-28 Frequency dynamics recorded by the closest sensor in Florida.....	65
Figure 2-29 Location of the generation trip events in the Southeast	67
Figure 2-30 Frequency deviations following generation trips in Southeast U.S.	67
Figure 2-31 Frequency dynamics recorded by the closest sensors in SC and NC.....	68
Figure 2-32 Location of the generation trip events in Mid-Atlantic.....	70
Figure 2-33 Frequency deviations following generation trips in the Mid-Atlantic	70
Figure 2-34 Location of the generation trip event in the Northeast.....	72
Figure 2-35 Frequency deviations following a generation trip in the Northeastern U.S..	72
Figure 2-36 Location of the generation trip event in the Midwest	74
Figure 2-37 Frequency deviations following a generation trip in the Midwest.....	74
Figure 2-38 Location of the generation trip event in West Central U.S.	75
Figure 2-39 Frequency deviations following a generation trip in West Central U.S.	75
Figure 2-40 Location of the generation trip event in Central-Southeast U.S.	77
Figure 2-41 Frequency deviations following a generation trip in Central-Southeast U.S.	77
Figure 2-42 Location of the generation trip event in Upper Midwest U.S.	78
Figure 2-43 Frequency deviations following a generation trip in Upper Midwest U.S. ..	78
Figure 2-44 Location of the generation trip event in the West South Central region.....	80
Figure 2-45 Frequency deviations following a generation trip in West South Central U.S.	

.....	80
Figure 2-46 Display of regional dynamic characteristics across EI	82
Figure 3-1 The December 3 rd , 2017 event dynamics as observed in Naples and Milan	88
Figure 3-2 Structure of the closed-loop system with the WADC [6], [47].....	93
Figure 3-3 Transfer function block diagram of the WADC	95
Figure 3-4 The HIL testing platform for the WADC.....	97
Figure 3-5 Overall structure of the controller	99
Figure 3-6 The graphical user interface of the damping controller	99
Figure 3-7 Implementation of the delay detector on CompactRIO	101
Figure 3-8 Supervisory control on the GUI	101
Figure 3-9 Implementation of the supervisory control function.....	101
Figure 3-10 Structure of the delay compensator.....	103
Figure 3-11 Input files to the OPAL-RT real-time digital simulator.....	105
Figure 3-12 Structure of a sample generation set in OpenModelica	105
Figure 3-13 Comparison of frequency deviation in OPAL-RT and PSS/e.....	107
Figure 3-14 Comparison of tie-line power oscillations in OPAL-RT and PSS/e.....	107
Figure 3-15 Frequency dynamics in the base case testing.....	110
Figure 3-16 Frequency response under 300ms additional communication delay.....	111
Figure 3-17 Frequency response under 500ms additional communication delay.....	111
Figure 3-18 Frequency response under 850ms additional communication delay.....	111
Figure 3-19 Frequency response of the system under random delays	113
Figure 3-20 Comparison of the buffered and unbuffered compensation	115
Figure 3-21 Control performance under 60% random data drop.....	115

Figure 3-22 Control performance with supervisory control	117
Figure 3-23 Control output with supervisory control	117
Figure 3-24 Actual delay measured by the controller.....	117
Figure 3-25 Control performance with TCP and UDP with random delay	119
Figure 3-26 Actual delay and control output under 5% data drop.....	119
Figure 3-27 Control performance with TCP and UDP under 5% data drop.....	120
Figure 3-28 Actual measured delay and control output under 10% data drop	120
Figure 4-1 Structure of the hierarchical-local frequency control [7].....	125
Figure 4-2 Structure of the HIL platform	129
Figure 4-3 Implementation of C37.118 communication within the HIL platform.....	129
Figure 4-4 The IBR model on OpenModelica	131
Figure 4-5 OPAL-RT ePHASORSIM implementation structure	131
Figure 4-6 Comparison of load bus voltages	134
Figure 4-7 Timeline of IBR control and communication delay testing	134
Figure 4-8 Closed-loop testing of IBR control and communication delay	136
Figure 4-9 Areas identified for frequency and voltage control actuators	138
Figure 4-10 Control commands, active power, and frequency	140
Figure 4-11 Control flag in the central controller (300 MW).....	140
Figure 4-12 Control commands, active power, and frequency	142
Figure 4-13 Control flag in the central controller (800 MW).....	142
Figure 4-14 Load bus voltages with and without control	145
Figure 4-15 Voltage and reactive power at participating generators	145
Figure 4-16 Reactive power of IBRs and the SVC.....	145

Figure 4-17 Load bus voltages with and without control (IBR priority).....	147
Figure 4-18 Voltage and reactive power at participating generators	147
Figure 4-19 Reactive power of IBRs and the SVC.....	147
Figure 5-1 Function modules in the microgrid central controller.....	155
Figure 5-2 Data flow of the power management module	158
Figure 5-3 Flowchart of the power management module.....	161
Figure 5-4 Feasibility of load combinations	163
Figure 5-5 Incidence matrix identifying connections in the microgrid	165
Figure 5-6 Topological treatment for merged (sub-)MGs	167
Figure 5-7 A group of P-f droop curves.....	172
Figure 5-8 Structure of the converter-based hardware testbed (HTB) [110].....	176
Figure 5-9 Converter-based HTB testing platform.....	176
Figure 5-10 HTB microgrid circuit model.....	177
Figure 5-11 Visualization interface of the HTB microgrid testing platform	180
Figure 5-12 Topology variations of the MG.....	180
Figure 5-13 Power, frequency, and voltage during the HTB testing	181
Figure 5-14 Voltage and current waveforms during the boundary expansion.....	183
Figure 5-15. Voltage and current waveforms during the PV curtailment.....	186
Figure 5-16. Power sharing and secondary frequency regulation.....	188

CHAPTER 1. INTRODUCTION

1.1 Background and Motivation

Power systems around the world are experiencing rapid changes in generation mix due to the increasing integration of renewable energy resources and retirement of traditional generation plants, which poses challenges to the safe operation of the power interconnections. On the other hand, the increasingly available measurement and communication facilities enhance the observability and controllability of the systems with real-time system awareness and offline data analytics. This dissertation aims to utilize measurements for enhanced monitoring and control of power systems with increasing integration of renewable resources.

First, monitoring the trends of inertia and primary frequency response is quintessential to the safe operation and corrective planning of the power interconnections in an era of generation mix changes. The Eastern Interconnection in North America has seen a significant increase in renewable energy integration (mainly solar and wind), accompanied by a large-scale coal-gas swap due to the retirement of coal-fired power plants [1]. While renewables pose challenges to the inertia and primary frequency response, the replacement of coal-fired units with gas units has the potential to improve the frequency dynamics. The overall trend of the frequency response remains an open question. With an abundance of synchronized measurement data from the FNET/GridEye frequency monitoring network hosted at the University of Tennessee and the Oak Ridge National Laboratory [2], [3], monitoring and analysis of the trends of the major power system becomes possible today. A trending study spanning 10 years from 2012 to 2021 for the Eastern Interconnection is

conducted to obtain the trending results in the Eastern Interconnection about its inertia and primary frequency response characteristics. These results could help improve power system operators' and planners' awareness of the position of the interconnection today and prepare them for changes in the future by understanding how various types of resources have changed the system in the past. Factors impacting the observed strength of primary frequency response are discovered in the process of primary frequency response evaluation also led to an improved event MW size estimation method. In addition to the interconnection level investigations, regional dynamic characteristics also need to be analyzed with the sensors across the system. This could help identify potential weak points in the large interconnection and provide critical information for future renewable integration plans.

Compared to the Eastern Interconnection, the Continental Europe Synchronous Area (CESA) system experienced a much faster decline in inertia due to its higher rate of renewable penetration. One of the challenges facing the CESA interconnection, as a result, is more inter-area oscillations during low inertia times, especially midnights when load demand is low and the renewable generation is high [4]. This inflicts additional limits on the power transfer capability available in a power interconnection. Effective suppression of the oscillations is essential for the safe operation of power interconnections and maximized utilization of existing transmission capabilities [5]. Traditional inter-area oscillation damping controllers are designed around a certain steady-state point with detailed system circuit models. Considering the scale of large interconnections, the accuracy of dynamic parameters of all components in the system is a big hurdle to the performance of such controllers. In addition, as the power systems operation conditions are

becoming more volatile due to the integration of renewables, the performance of controllers designed at a specific operation point can suffer deterioration in real-world operations. Hence, a measurement-based wide-area damping controller is proposed to take advantage of the increasing availability of Phasor Measurement Units (PMUs) [6]. The power system dynamic behavior is characterized by a low-order transfer function model based on synchrophasor measurements. The transfer function model can be updated in real-time to track the latest system operating conditions, and the controller parameters can be updated accordingly. A measurement-based wide-area damping controller for the Continental Europe Synchronous Area system is designed and implemented in this dissertation to suppress the 0.293 Hz inter-area oscillation between its north and south. The controller design, implementation, and hardware-in-the-loop (HIL) testing are introduced in detail.

Despite the challenges the increasing integration of renewables poses to power systems, they are also bringing opportunities for improving the control of both large-scale power interconnections and distribution networks with the assistance of measurements. The New York State Grid has been incorporating battery energy storage systems and wind farms into its fleet. The fast response capability of these inverter-based resources has opened doors to faster and more efficient control schemes for improved dynamics and stability. Together with the increasingly available deployment of PMUs and communications, measurement-based frequency and voltage control schemes coordinating inverter-based resources and traditional generations are designed for the New York State Grid. The hierarchical-local frequency control strategy prioritizes local active power mismatch detection and compensation, yet has the capability of inter-area power dispatch that preserves information privacy [7]. The control takes advantage of measurements from

PMUs to realize fast frequency control and prevents over- or under-compensation. The voltage control scheme utilizes voltage and reactive power feedback signals to achieve a closed-loop control based on the gradient method, which is much less dependent on the accuracy of the power system models and operating conditions. The control automatically coordinates IBRs, SVCs, and traditional generators [8]. The frequency and voltage controllers are designed for the New York State Grid and implemented on hardware. A hardware-in-the-loop testing platform is constructed with the 5000-bus New York State Grid model simulated in real time for the testing and validation of the hardware controllers.

In addition to interconnection-level integrations, the deployment of inverter-based resources in distribution networks has also been significant in recent years. With the increasing installation of smart switching devices, measurement units, and communication facilities, more flexible, efficient, and reliable operation of distribution networks has become possible. One of the most promising approaches to this is utility-scale community-based microgrids that withstand extreme events through islanded operations. To handle the uncertainties brought along by the distribution-level renewable resources, the concept of dynamic boundaries for improved efficiency and reliability has been proposed in the literature [9], [10]. To enable the islanded microgrids to operate flexibly with dynamic boundaries and multiple source locations, a measurement-based real-time power management module is proposed and implemented, which handles the increased complexity in topological variations and transitions stemming from the flexible operating conditions and adaptability requirement for arbitrary topologies [11]. This includes the real-time operation of multiple islands with dynamic boundaries, initiation of topological transitions (merging and separation of islands), and automatic source coordination for

power sharing and frequency regulation. All functions in the power management module are designed to be automatically adaptable to arbitrary microgrids with non-meshed topologies so that the deployment of the controller at new microgrid sites can be expedited at a reduced cost. The module has been implemented on NI's CompactRIO system as an essential part of an MG controller and tested on a converter-based hardware testbed (HTB). Testing results verified the effectiveness of the algorithms under various operating scenarios.

1.2 Dissertation Outline

The rest of the dissertation is organized as follows.

Chapter 2 discusses the measurement-based historical trend assessment for the inertial response and primary frequency responses in the Eastern Interconnection, including the data sources, considerations in the evaluation of the frequency dynamics, and the trending analysis results. An improved MW estimation method is proposed based on the findings in the process of primary frequency response assessment. In addition, regional dynamics are discussed with sample events across the interconnection to provide preliminary knowledge for future regional inertia studies.

Chapter 3 presents a measurement-based wide-area damping control (WADC) scheme verified on the real-time model of the Continental Europe Synchronous Area power interconnection. It introduces the choice of the WADC control loop, the measurement-based modeling of the system, the design of the control parameters, and the hardware implementation. A hardware-in-the-loop (HIL) testing platform with a network impairment simulator integrated into the loop is constructed for real-time performance testing of the controller under a variety of realistic operating conditions.

Chapter 4 implements and tests the measurement-based frequency and voltage control schemes on the New York State Grid, which leverage the available inverter-based resources and coordinate them with traditional resources. The design philosophies of the frequency and voltage control schemes incorporating the inverter-based resources are discussed. The controllers are implemented on hardware control platforms and tested in the HIL setup with a 5000-bus New York State Grid model simulated in real time.

Chapter 5 discusses the design and implementation of a measurement-based real-time power management module for operating multiple-source-location dynamic-boundary microgrids with inverter-based resources. The structure, functions, and algorithms of the power management module are introduced, with an emphasis on the flexible design that adapts to arbitrary non-mesh topologies for the expedited deployment of the controller at new microgrid sites with a reduced cost. The controller has been implemented on hardware and tested on the hardware testbed (HTB).

Chapter 6 concludes the work in this dissertation and identifies future research opportunities.

CHAPTER 2. MONITORING THE TRENDS OF INERTIA AND PRIMARY FREQUENCY RESPONSE

2.1 Introduction

Monitoring the trends in power systems amid the era of generation mix changes is critical for maintaining awareness of the system today and understanding its potential evolution in the future. This Chapter discusses the analysis, methods, and findings about inertia and primary frequency response in the Eastern Interconnection with field measurement data captured by the FNET/GridEye system in the past decade. This study confirms the decline in inertia as expected by the industry and unveils an unexpected increase in primary frequency response. An improved event MW size estimation scheme is also proposed based on the improved primary frequency response estimation method. Additionally, regional dynamics in a variety of areas in the Eastern Interconnection are discussed to identify potential weak points in terms of regional inertia, which could be informative for future operation and planning with uneven renewable integrations.

It should be noted that part of the content in this Chapter is from the author's articles submitted to the 2023 IEEE PES GT&D International Conference and Exposition [12] and the IEEE Access journal [13].

2.1.1 Background and Motivation

The appropriate response of a power system to active power mismatch caused by disturbances is critical in maintaining its stability and efficiency. The response is typically comprised of inertial response, primary frequency response, secondary frequency response, and tertiary frequency response. While the secondary and tertiary frequency controls aim

at bringing the system back to normal operation with minimized steady-state frequency deviation and area control error, the inertial and primary frequency responses are critical in arresting frequency dynamics and maintaining system stability in the first few seconds after the occurrence of the disturbance. The inertial response happens instantly following the frequency discursion due to the electromagnetic tie between the generator rotors and the stator terminals. During the inertial response, the power imbalance gets either stored in or released from the rotors in the form of kinetic energy, which mitigates the rate of change of frequency (RoCoF). The primary frequency response, on the other hand, is a control mechanism by generator governors to arrest frequency deviations by increasing or decreasing the active power output to compensate for the power mismatch due to the disturbance [14], [15].

However, the inertial response and primary frequency response are facing changes in the era of generation mix evolvment. Generation mixes of power systems around the globe are experiencing rapid transformation due to the integration of renewable energy resources. Most of the renewable resources are interfaced with the grid through power electronics converters. Although some converters provide advanced inertial and primary frequency response capabilities, the majority of the renewable resources today are operating in the grid-following mode without frequency response capabilities due to considerations of stability, equipment aging, and lost opportunity costs for headroom reserves [16]. This is expected to deteriorate the inertial and primary frequency response as the penetration of the renewables increases.

On the other hand, the development in the generation mix can be more complicated in some power interconnections. For example, in addition to the increasing renewables, the

Eastern Interconnection also experienced a large amount of replacement of coal plants with gas units [17]. Gas-fired generators typically contribute higher inertia per MW and stronger primary frequency response due to their tighter governor dead bands (10 - 17 mHz) and stiffer droop curves (4%) [18].

With the integration of renewables, the replacement of coal plants with gas plants, and other changes happening in the generation mix at the same time, the actual course of the development in the inertial response and the primary frequency response becomes an open question. Quantified assessments of the two quantities are critical for system operators and planners to be aware of the historical trends in the past, the current position of the system today, and potential corrective planning needed for the changes coming in the future.

Research about the frequency response amid the generation mix evolution has drawn attention from both the industry and academia. The Multiregional Modeling Working Group (MMWG) models of the Eastern Interconnection have been used by researchers to create high wind and solar penetration scenarios for studying the changes brought up by renewables [19-22]. While these models provided valuable insights about the impact of wind and solar integration on inertial and primary frequency response, they may not have accurately reflected a few critical aspects of the system response, including the drastic change in coal and gas-fired plants in recent years and the accurate representation of governor dead band settings.

Measurement-based evaluations, on the other hand, focus on the actual response exhibited by the system as a holistic demonstration of all changes and are suitable for retrospective trending analysis. A 10-year trending analysis of primary frequency response was conducted for Eastern Interconnection from 1994 to 2004 in [23] and found a declining

trend. Reference [24] provided a trending analysis of the Eastern Interconnection, concluding the frequency response in the Eastern Interconnection has been stable from 2009 through 2012. One unresolved issue with the analysis in these studies is the uncertainty shown by the low correlation coefficient among the events, which leads to lower confidence in the results obtained. Reference [25] provided further analysis and showed that a few factors, including the pre-disturbance frequency, has a significant impact on the β values calculated, but they were not leveraged to further improve the trending analysis of frequency responses.

This study takes advantage of the historical data collected by the synchronized phasor measurement network, FNET/GridEye, in the past decade (2012 to 2021) for a quantified evaluation of both the inertial response and primary frequency response in the Eastern Interconnection. The study provides an analysis of critical factors that affect the effective and consistent evaluation of inertial and primary frequency response for large-scale power systems like the Eastern Interconnection. For inertial response evaluation, the selection of an appropriate calculation time window is discussed for optimal balance between reliability and accuracy. For primary frequency response, the impact of critical factors on the evaluation, including governor dead bands, event starting frequency, and event MW size, are discussed in detail. Methods to minimize the impact of these factors on the evaluation of the trends in the past decade are then introduced. These methods significantly improved the confidence of the results of the trending analysis and revealed rather unexpected changes in the Eastern Interconnection frequency response.

The knowledge of the impact that the starting frequency and MW size have on the observed primary frequency response can also be leveraged to improve the event MW

estimation. This is realized by taking into consideration the quantified relation between the primary frequency response and these two factors.

Also discussed are the regional dynamics observed in local measurements taken by FNET/GridEye. As it is observed that local frequency dynamics can deviate drastically from the interconnection during transients, regional frequency behavior can be of interest to both system operators and planners. Sample events will be presented for a variety of locations across the Eastern Interconnection to identify high-risk areas in terms of severe local frequency dynamics, which could be informative for more rigorous studies on regional inertia and frequency security.

The rest of this chapter is organized as follows: section 2.1 presents an overview of power system frequency responses and estimation methods for the inertial and primary frequency response. Section 2.2 introduces the FNET/GridEye and data-preprocessing procedures required for the evaluation of the inertial and primary frequency response. Section 2.3 discuss the methods of inertia calculation and the results for the past decade. Section 2.4 presents the calculation of the primary frequency response and the details and nuances that have a significant impact on the process of revealing the actual trend of the primary frequency response. Explanations for the unexpected trend in the primary frequency response in Eastern Interconnection are also given. Section 2.5 discusses the formulation and solution for the improved event MW size estimation method. Section 2.6 presents sample events across various regions in the Eastern Interconnection and concludes patterns in regional dynamics that can be informative for future studies, operations, and planning. Section 2.7 gives a summary of the frequency work in this chapter.

2.1.2 Power System Frequency Response – Time Scale of Interest

Power systems utilize controllable equipment to maintain system frequency within an acceptable range following a disturbance, such as generation trip, load pickup/shedding, transmission line trip, etc. Different controls are in place to handle frequency regulation across different time scales. These control schemes include [26]:

- **Primary frequency control**

Actions provided by the interconnection to arrest and stabilize frequency in response to frequency deviations. Primary Control comes from automatic generator governor response (also known as speed regulation), load response (typically from motors), and other devices that provide an immediate response based on local (device - level) control systems.

- **Secondary frequency control**

Actions provided by an individual balancing authority or its reserve sharing group to correct the generation-load imbalance that created the original frequency deviation, which will restore both Scheduled Frequency and Primary Frequency Response. Secondary Control comes from either manual or automated dispatch from a centralized control system.

- **Tertiary frequency control**

Actions provided by Balancing Authorities on a balanced basis that are coordinated so there is a net zero effect on Area Control Error (ACE). Examples of Tertiary Control include dispatching generation to serve native load; economic dispatch; dispatching generation to affect Interchange; and re-dispatching generation. Tertiary Control actions are intended to replace Secondary Control Response by reconfiguring reserves.

In this work, the time scale of interest is the first 50-60 seconds after a disturbance (primary frequency control), which, in most interconnections, reflects the impact of system inertia due to the kinetic energy in rotating mass and governor response, as shown in Figure 2-1. The first few seconds immediately following the disturbance will be used for calculating the system inertia, and the first 50 seconds will be used to calculate the beta value. Details are given in the following sections.

2.1.3 Estimation of Power System Inertia

Estimating power system inertia can be especially helpful in such situations since it provides awareness of safety margin and useful information for future planning activities. Research in the inertia estimation realm can be categorized into four major types based on their data sources:

- a) Measurement following large disturbance events
- b) Measurement following artificial probing injections
- c) Ambient measurement
- d) Dispatch information and generator parameters

2.1.3.1 Inertia Estimation Based on Disturbance Measurement

Large disturbance events, such as generation unit disconnections, introduce sudden active power mismatch in a power system and cause significant transients in system frequency. The frequency transient is a result of three major components of the response, the inertial response, governor response (primary and secondary), and load damping.

Generator inertia and load damping react to frequency deviations instantly from the moment the disturbance occurs, while the primary and secondary frequency response initiated by governors, load damping, and area generation control (AGC) systems take

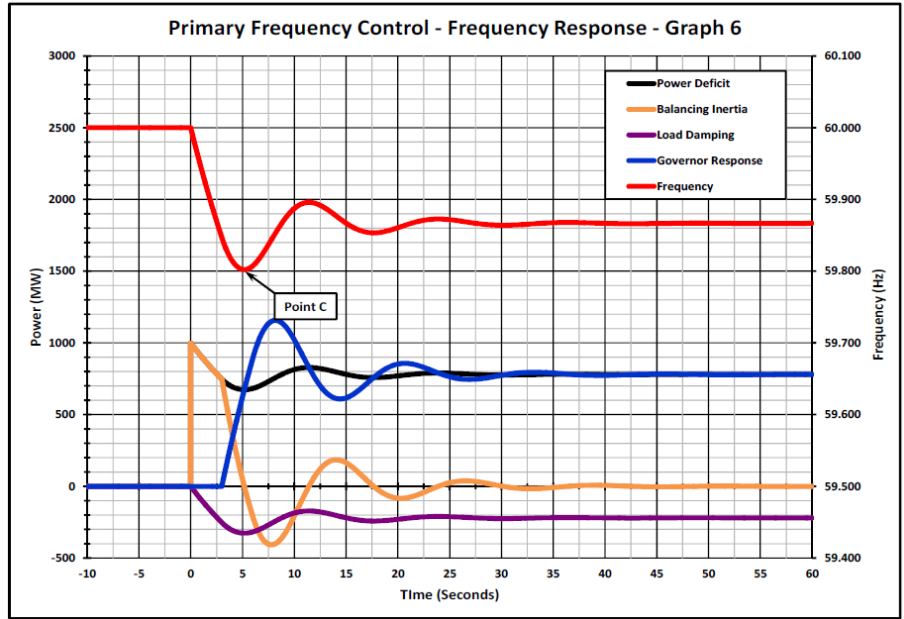


Figure 2-1 Typical primary frequency response and power contribution [26]

seconds to minutes to be significant. Hence, the first few seconds immediately after the occurrence of the disturbance is chosen as the time window for inertia analysis.

Immediately following a generation tripping event, the active power deficit is compensated majorly by the kinetic energy released from the rotating mass in the system. The derivative of frequency is determined by the power deficit, which is the net sum of the amount of generation tripped, and the decrease in demand due to load damping (frequency response of frequency-sensitive loads), as shown in equation (2-1)

$$2H \frac{df}{dt} = (\Delta P - D\Delta f) \quad (2-1)$$

Due to the small frequency deviation (typically within 0.05Hz) and load damping ratio D , the second term on the right-hand side of equation (2-1) can be neglected, leading to the linear correlation between RoCoF and Δf :

$$2H \frac{df}{dt} = \Delta P \quad (2-2)$$

As the RoCoF ($\frac{df}{dt}$) can be calculated from the frequency transient following large disturbance events, the equivalent inertia can be estimated with the calculated RoCoF and the power mismatch. To obtain an accurate inertia estimate, it is important to approach the RoCoF calculation properly and to have an accurate power mismatch report. In real-world measurements, the frequency transient of a disturbance can often be obscure due to the small RoCoF, noises, and oscillations. Thus, data processing is critical in accurate RoCoF and inertia estimation. Thanks to the wide-deployment of FNET/GridEye synchronized frequency monitoring sensors in the Eastern Interconnection, the noise and oscillations can be mitigated directly with the abundance of wide-area measurements by applying a median filter. More details will be discussed in section 2.2.3.

2.1.3.2 Other Inertia Estimation Methods

Large disturbance events are rare in power systems, so they are usually used for post-event analysis instead of continuous monitoring of the inertia constant. Researchers have proposed estimation methods that utilize ambient measurement data, injection of small probing perturbations, or dispatch information for quasi-real-time continuous monitoring of inertia.

Probing-injection-based methods actively inject small perturbations into the power network and monitor frequency dynamics in response to injection for system identification [27-30]. Following the artificial injection of the perturbation, the frequency measurement feedback can be used together with the probing signal to determine system inertia. For moderately larger artificial perturbations in a small power system, the inertia can be estimated using a process similar to that in the disturbance measurement based methods, which calculate inertia directly with the RoCoF and the MW values [27]. Such methods introduce considerably large perturbations and may pose risk to the safe operation of the power systems. Other probing methods, however, use smaller perturbations and attempt to construct a transfer function that characterizes the relationship between the measured frequency and the injected power change [28-30]. In general, the probing signal shall have enough energy in the frequency range of interest for a satisfactory signal-to-noise ratio, but not large enough to pose risk to the secure operation of the system. Choices of the probing signals include white noise, sinusoidal, multi-sine, exponentially enveloped sinusoidal, etc.

Ambient-measurement-based methods, on the other hand, accomplish the estimation with non-event, non-intrusive ambient measurement. It requires no large disturbances, no probing injections, and can be used to monitor system inertia in a nearly continuous

manner. These methods take measurements of frequency and power at certain locations during normal operation and apply system identification techniques or other modeling methods to extract information about the system's inertia [31-34]. The difficulty in inertia estimation with ambient measurement data is that the inertial response is hard to be distinguished from other dynamics during normal operation, such as frequency control, voltage control, electro-mechanical dynamics, and stabilizing actions [35]. Also, the methods are typically less accurate due to the lower signal-to-noise ratio of ambient measurements.

Lastly, the dispatch-information-based inertia estimation method uses information about the generator commitment status across the grid and the inertia contribution from all generators online to estimate the total inertia. It facilitates reliable, real-time, and continuous inertia monitoring and has been adopted by a number of transmission system operators (TSOs) [36-38]. Such inertia estimation methods can be integrated into existing SCADA systems. Examples of successful integration include the Svenska Kraftnat SCADA system, the Fingrid SCADA system, the Statnett SCADA system, and the Energinet DK SCADA system. While the majority of generator circuit breaker statuses are available in these power systems, there can still be generator statuses that are not accessible by the TSOs. For the inertia contributed by those inaccessible generators, it can be estimated roughly by observing load levels and renewable generation in the system.

Whereas these methods are not the focus of the inertia assessment work in this dissertation, they have the potential to estimate regional inertia levels with measurements appropriately deployed across the system.

2.1.4 Estimation of Primary Frequency Response

Similar to the estimation of inertia, the estimation of primary frequency response also requires data pre-processing to minimize the impact of noise in the measurement. The NERC frequency response standard background document provided a standardized primary frequency response measure method, as shown in Figure 2-2 [26]. It takes the data 16 seconds before the event occurrence as pre-disturbance frequency (level A), and the data 20 – 52 seconds after the occurrence as the post-disturbance frequency (level B), for the calculation of primary frequency response.

However, with field measurement of real-world events, more factors should be considered in the calculation of the primary frequency response, including the event's starting frequency, the impact of governor dead bands, etc, which have rarely be discussed sufficiently for evaluating the trend frequency response. More details about handling these factors will be presented in this chapter.

2.2 Data Sources and Preprocessing

Two primary data sources are utilized in this project for quantitative analysis of system inertia and beta value:

- FNET/GridEye
- NERC confirmed MW information for generation trip events

2.2.1 FNET/GridEye

FNET/GridEye is a low-cost synchronized wide-area power system frequency measurement network deployed at the distribution level. It is the only monitoring network that covers all three major interconnections (the Eastern Interconnection, the Western Interconnection, and the Texas Interconnection) in North America with more than 200

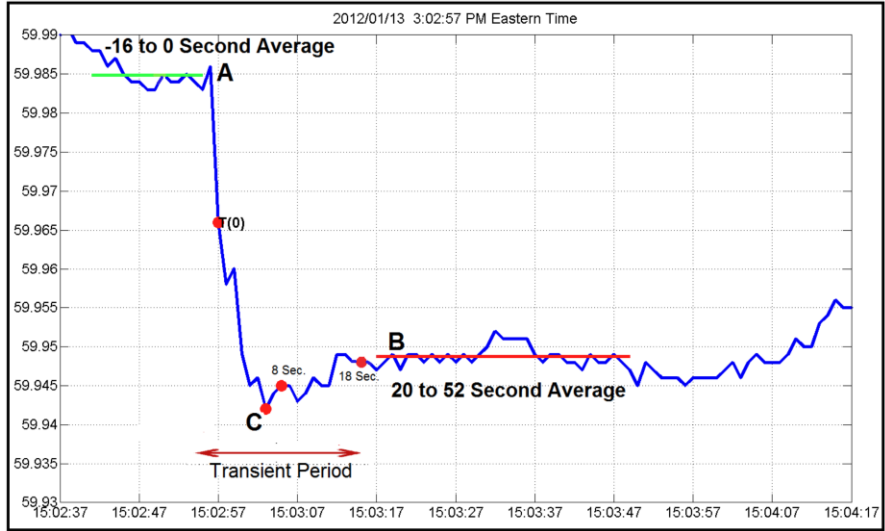


Figure 2-2 Measurement of primary frequency response [26]

sensors. It also monitors power grids around the world with more than 80 sensors [3], [39], [40]. Figure 2-3 presents the deployment map for FNET/GridEye sensors in the United States.

FNET/GridEye sensors are designed for easy and low-cost deployment in homes or offices in a plug-and-play manner as long as access is available to a 120 V power outlet, a network connection, and a clear view of the sky. The first generation FNET/GridEye sensor, called the frequency disturbance recorder (FDR) transmits GPS timestamped frequency, voltage magnitude, and voltage angle measurements to the servers hosted at the University of Tennessee and the Oak Ridge National Laboratory for data processing, analysis, and storage [41]. The recently updated sensor, Universal Grid Analyzer (UGA), enables an ultra-high reporting rate (1500 frames/second) and facilitates point-on-wave measurement, power quality monitoring, and advanced applications [42]. A number of situational awareness tools have been developed. Online applications include real-time monitoring and visualization, event location, islanding alert, area control error monitoring, oscillation alert and control, etc. [2], [43-52]. Offline applications include post-event analysis, large-scale power grid model validation, data analytics, AI and machine-learning-based applications, forensic research using grid data, etc. [53-59].

Online applications send alerts and notifications to utility companies, regulatory agencies, and independent system operators for emergency alerts, enhanced awareness, and controls. Offline applications provide valuable data for the analysis and validation of historical events and simulation models.

In this study, the raw data of synchronized frequency measurement were extracted from the historical database of FNET/GridEye for trending analyses. A total of 352

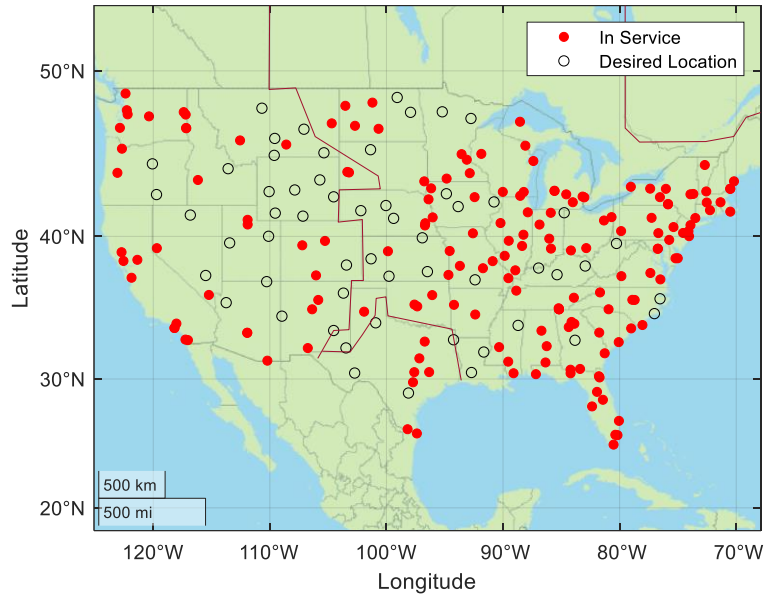


Figure 2-3 Deployment of FNET/GridEye Sensors

generation trip events are used for the quantitative evaluation of inertial and primary frequency response in Eastern Interconnection.

2.2.2 NERC Registry with Confirmed MW information

It is essential to have confirmed MW information for the generation tripping events, together with the frequency measurement, to calculate system characteristics like inertia and beta value. The UTK team has access to a generation trip event list with detailed MW information, which is maintained by NERC (North American Electric Reliability Corporation).

2.2.3 Data Preprocessing

With the NERC registry of generation tripping events, historical frequency measurements are extracted from the FNET/GridEye database for events that have confirmed MW information available. Before calculating the inertia and beta value with the measurements, the raw data should be preprocessed to reduce the impact of measurement error, oscillations, etc.

For large-scale power interconnections like the Eastern Interconnection, frequency dynamics can experience a more complicated process of propagation, oscillation, and region-specific dynamics. The vast geographical coverage and the massive capacity of the system make it a necessity to have a large number of measurements available across the interconnection for a complete understanding of the frequency dynamics of the system. A limited number of measurements confined to specific areas will have difficulty reflecting the dynamic behaviors of the interconnection as a whole.

For example, the Florida area in EI is well known to have a ‘loose’ connection to the rest of the Eastern Interconnection, which makes the area more likely to be excited for

oscillations against the rest of the system amid disturbances. If measurement sensors were confined within the area, the analysis results may not accurately reflect the characteristics of the whole interconnection. Figure 2-4 shows a generation trip event that happened on April 15, 2020, near Okeechobee, FL. The curves in the brown shades are measurements taken in the state of Florida, and the curves in the shade of blue are from nearby states in the southeast. Conclusions one draws with only measurements from specific areas may vary widely from others using measurements from the rest, because of the vastly different frequency responses in different areas, especially in the first few seconds after the disturbance. A median frequency that well represents the dynamics of the whole interconnection becomes critical for characterizing the inertial and primary frequency responses.

The wide deployment of FNET/GridEye sensors enables an overarching awareness of the frequency dynamics across the whole Eastern Interconnection. For all the generation trip events in the past decade, there were at least 60 active sensors reporting synchronized measurements in EI at the times of occurrence. The frequency measurements are first aligned by their GPS-synchronized timestamps. Then, the median frequency can be calculated at every sampling step with measurements from all sensors:

$$f_{median} = \begin{cases} \mathbf{F} \left[\frac{n+1}{2} \right], & n \text{ is odd} \\ \frac{\mathbf{F} \left[\frac{n}{2} \right] + \mathbf{F} \left[\frac{n}{2} + 1 \right]}{2}, & n \text{ is even} \end{cases} \quad (2-3)$$

where \mathbf{F} is the ordered list of the reported frequency at a certain sampling time, and n is the number of active sensors at the moment of the sampling step. The median frequency curve obtained with equation (2-3) for the sample event in FL is plotted as the bold black

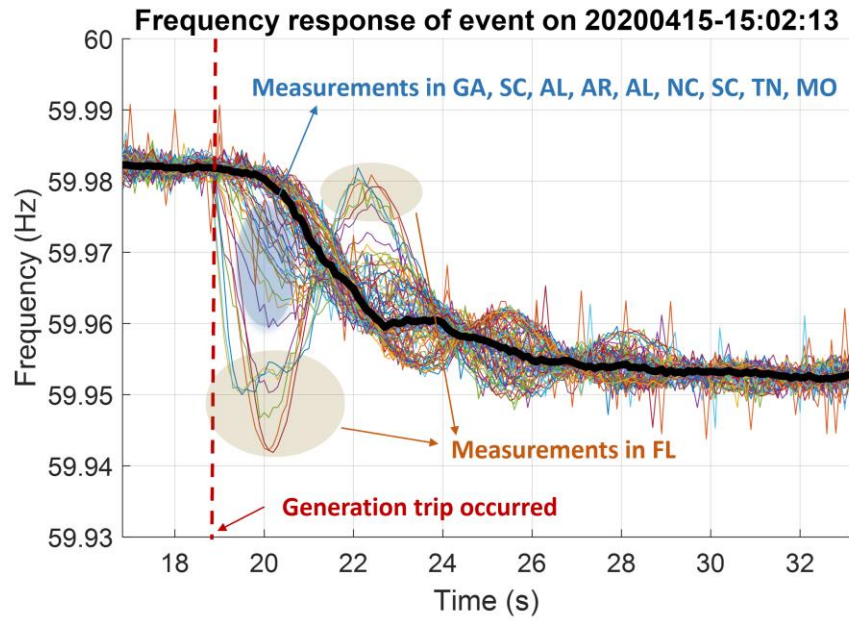


Figure 2-4 Generation trip event in Florida

curve in Figure 2-4, which represents the overall trend of decline in frequency in the interconnection. Using the median frequency curve mitigates measurement errors, avoids the over-exhibition of regional frequency dynamics in specific areas, and puts stress on the overall frequency response on the interconnection level. All trending analyses in the following text will be utilizing the median frequency curve for the generation trip events.

2.3 Trend Analysis of Inertia

For the quantification of interconnection-wide equivalent inertia, all rotating mass and other equivalent fast responses can be conceptually treated as one rotor collectively, and the following equation governs the dynamics in the first few seconds after the disturbance:

$$2H \frac{df_{median}}{dt} = (\Delta P - D\Delta f_{median}) \quad (2-4)$$

where H represents the inertia constant of the whole interconnection, f_{median} is the median frequency as described in section 2.2, ΔP is the power mismatch resulting from the disturbance, and D is the load damping ratio. As the frequency deviation is small in the first few seconds following the event and most generation trip events lead to steady-state frequency deviations smaller than 50mHz (0.001p.u.), the load damping effect can be neglected for the investigation of inertia. Hence, it is reasonable to expect the rate-of-change-of-frequency (RoCoF) to be proportional to the power mismatch. If a such linear correlation is verified by the data in the field, the coefficient of the linear relationship will be the interconnection inertia being sought.

2.3.1 Considerations for the RoCoF and inertia calculation

As discussed above, accurate calculation of the RoCoF is crucial for the effective evaluation of inertia. One important parameter in the calculation of RoCoF for inertia

assessment is the length of the time window following the disturbance. Theoretically, the shorter the time window, the better for inertia estimation. As the inertial response is instant and other responses like the primary response take time to react, a shorter window will involve fewer unwanted responses.

For small power systems or regional inertia estimation, a rule-of-thumb choice of the RoCoF time window is 0.5 seconds, as governors typically take seconds to react to frequency disturbances [60]. However, when focusing on the overall frequency dynamics of a power system as vast as the Eastern Interconnection, a larger window is needed. As an example, Figure 2-5 shows a close-up view of the Florida event in Figure 2-4. The blue curve is the measurement in Orlando, FL, near the generation trip location. A short time window of 0.5 seconds is sufficient for the estimation of RoCoF with the blue curve thanks to the crisp event start point and the frequency decline being almost a straight line within that window. However, such RoCoF and inertia results only reflect the regional frequency dynamics and regional inertia for Florida.

The evaluation of the interconnection RoCoF and inertia, however, can be different. It is noted that the median frequency (black curve) was almost unchanged in the first second after the disturbance, in which the FL regional frequency took to the nadir and those in the southern states (GA, SC, AL, AR, AL, NC, SC, TN, MO) started to follow. After the first one second, the frequency in FL and other southern states started to bounce back, which means the inertia support from the rest of the interconnection arrives, and that is when the median frequency started to drop.

In a large power system like the Eastern Interconnection, the electromagnetic propagation of the inertial response from other regions takes time to travel across the vast

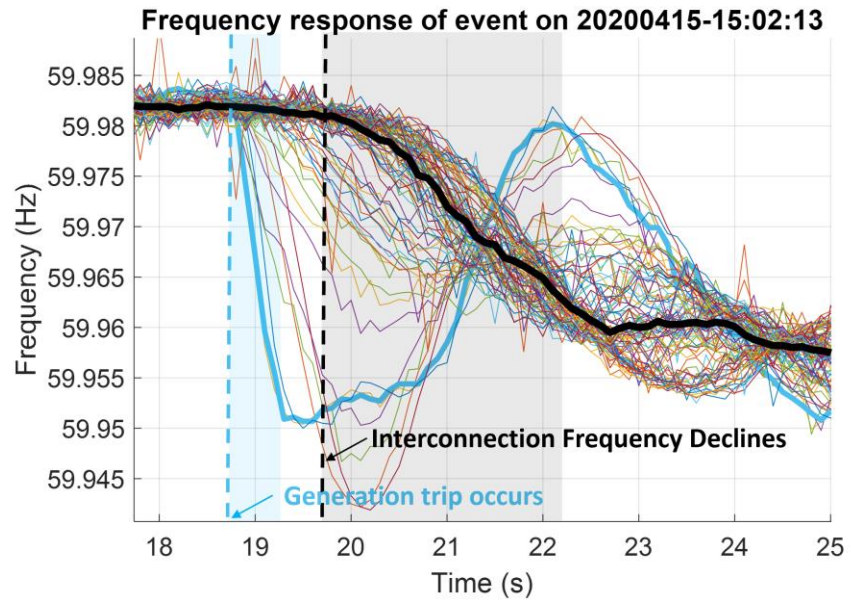


Figure 2-5 Comparison of regional and interconnection frequency dynamics

geographical areas to support the area of disturbance origin. This makes the median frequency RoCoF, which represents the interconnection frequency, often experiences a flatter decline at the beginning of the disturbance as inertial support from other regions has yet to arrive at the area of disturbance. In addition, the large total inertia of the interconnection itself leads to a smaller $|RoCoF|$, which renders it prone to the impact of noise when using a short time window.

A longer time window is desirable for the interconnection-level inertia evaluation, but at the same time, too long a time window will involve too much primary frequency response as the generator governors start to react to the frequency deviation. Hence, to choose an appropriate time window, the correlation coefficient between the MW size and the RoCoF can be used as an indicator for the consistency of estimation to find the optimal balance. Time windows of 0.5 seconds, 1 second, 2 seconds, 3 seconds, 4 seconds, and 5 seconds have been used to calculate the RoCoF of the events.

For a time window selected, the RoCoF of the events can be calculated and used for the calculation of its correlation coefficient with the MW size:

$$R(\mathbf{MW}, \mathbf{RoCoF}) = \frac{1}{N-1} \sum_{i=1}^N \left(\frac{\mathbf{MW}(i) - \mu_{\mathbf{MW}}}{\sigma_{\mathbf{MW}}} \right) \left(\frac{\mathbf{RoCoF}(i) - \mu_{\mathbf{RoCoF}}}{\sigma_{\mathbf{RoCoF}}} \right) \quad (2-5)$$

where R is the correlation coefficient between \mathbf{MW} and \mathbf{RoCoF} , N is the number of events, \mathbf{MW} is the vector containing the MW sizes of the generation trip events, \mathbf{RoCoF} is the vector containing the RoCoFs calculated with the selected time window for the events, $\mu_{\mathbf{MW}}$ and $\mu_{\mathbf{RoCoF}}$ are the average values of the \mathbf{MW} and the \mathbf{RoCoF} vectors elements, and $\sigma_{\mathbf{MW}}$ and $\sigma_{\mathbf{RoCoF}}$ are the standard deviations of the \mathbf{MW} and the \mathbf{RoCoF} elements. For example, Figure 2-6 shows the MW-RoCoF plot for generation trip events in the year 2020 with a 3-second RoCoF calculation window, and the correlation coefficient is 0.89.

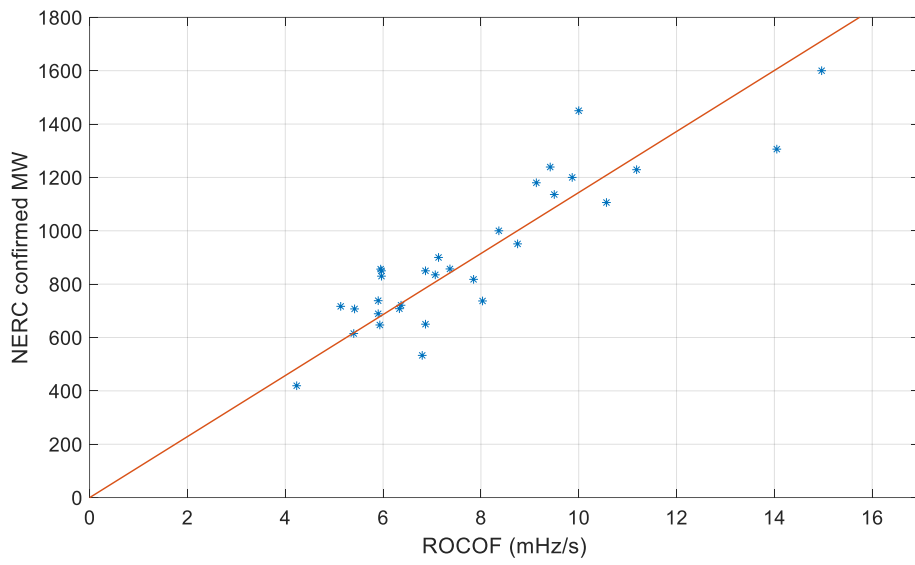


Figure 2-6 Plot of RoCoF against MW for events in the year 2020

Conducting such correlation coefficient calculation for all years from 2012 to 2021 with time windows from 0.5 seconds to 5 seconds gives the results in Table 2-1.

Figure 2-7 shows the average values and standard deviations of $R(MW, RoCoF)$ under different RoCoF time windows with data from 2012 to 2021. As the RoCoF calculation window becomes longer, the average correlation coefficient increases, and the standard deviation decreases. However, the benefit of lengthening the RoCoF calculation window becomes marginal after it reaches 3 seconds, as shown by the flat zones after 3 seconds on the curves of average value and standard deviation. To minimize the chance of involving governor actions while maintaining a high correlation, the time window of 3 seconds is chosen in the following analysis for the Eastern Interconnection.

2.3.2 Inertia Trend Results

With the 3-second RoCoF calculation window, the RoCoFs are calculated for each generation trip event from 2012 to 2021. The inertia values are then assessed quarterly (four quarters a year) using the least-squares fitting method to find the first-order fitted curve. The slope of the fitted curve indicates the inertia of the system and can be found by:

$$2\hat{H} = (\mathbf{RoCoF}^T \mathbf{RoCoF})^{-1} \cdot \mathbf{RoCoF}^T \cdot \mathbf{MW}$$

$$\mathbf{RoCoF} = \left[\frac{\Delta f_1}{\Delta t}, \frac{\Delta f_2}{\Delta t}, \dots, \frac{\Delta f_n}{\Delta t} \right]^T \quad (2-6)$$

$$\mathbf{MW} = [MW_1, MW_2, \dots, MW_n]^T$$

where $(\Delta f_i)/\Delta t$ is the rate of change of frequency in time window Δt for generation trip event i , MW_i is the size of the generation trip i , and n is the number of events. Dividing the events available into quarterly divisions and setting the Δt to be 3 seconds yields the quarterly inertia results with the 3-second RoCoF time window.

Table 2-1 Correlation coefficients between MW and RoCoF

Time window (seconds)	0.5	1	2	3	4	5
2012	0.55	0.64	0.76	0.90	0.91	0.92
2013	0.46	0.77	0.90	0.93	0.94	0.94
2014	0.40	0.81	0.83	0.87	0.86	0.83
2015	0.34	0.74	0.82	0.88	0.89	0.89
2016	0.21	0.65	0.78	0.81	0.81	0.81
2017	0.09	0.64	0.89	0.87	0.86	0.81
2018	0.60	0.75	0.76	0.76	0.79	0.77
2019	0.41	0.84	0.91	0.90	0.91	0.90
2020	0.69	0.79	0.87	0.89	0.90	0.88
2021	0.66	0.90	0.89	0.89	0.90	0.90
Avg.	0.44	0.75	0.84	0.87	0.88	0.87
SD	0.18	0.08	0.06	0.05	0.05	0.05

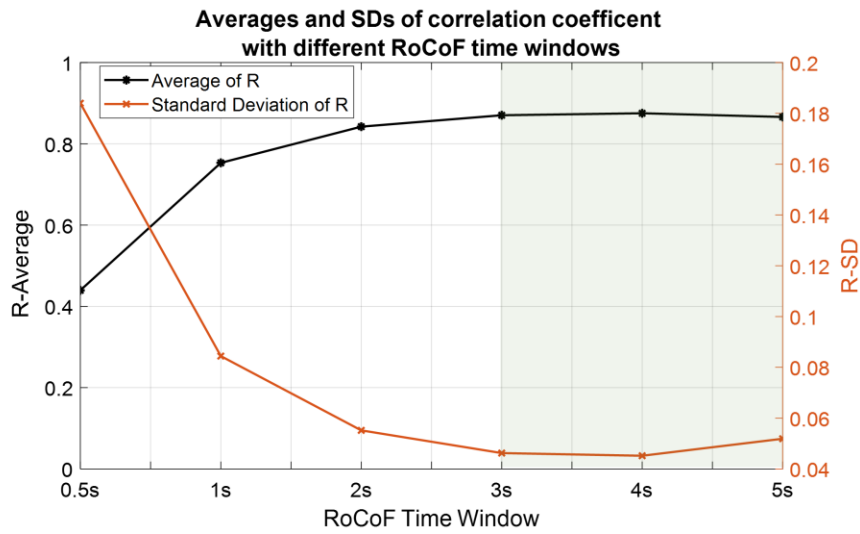


Figure 2-7 Mean and SD of the correlation coefficient with different RoCoF windows

It should be noted that the inertia estimated using the 3-second time window is not strictly the theoretical inertia of the system. While the slightly longer time window reliably captures the interconnection-level response, there will be inevitably a certain level of governor response involvement, especially in the area of event origin where the local frequency experiences the most drastic dynamics. Nevertheless, it is good enough for the purpose of revealing the relative trend of the inertia in the past decade, instead of the accurate inertia value of the system. The trend of inertia (calculated with 3-second RoCoF) of the Eastern Interconnection from the year 2012 to 2021 is shown in Figure 2-8. The blue circles are the quarterly inertia (40 quarters in total) and the black dash curve is the smoothed trending curve.

Three features are clearly visible in the figure: a) The Eastern Interconnection has experienced a decline of 10% in its inertia in the past decade. The benefit of higher inertia contribution per MW from gas-fired generators is outweighed by the lack of inertia from renewable energy sources; b) The EI inertia has clear seasonal variations – even the quarterly averaged inertia can vary by more than 20% in different seasons; c) The highest inertia mostly appears in the third quarter, where the high temperature summer months are included. These summer months have the highest generator commitment rate due to the high demand, leading to higher inertia levels.

2.4 Trend Analysis of Primary Frequency Response

In this section, the calculation of the primary frequency response will be introduced first, and then factors that have a significant impact on the observed primary frequency response β will be discussed in detail. In the end, an effort in excluding such impact for a consistent and accurate reflection of the trend of β will be presented.

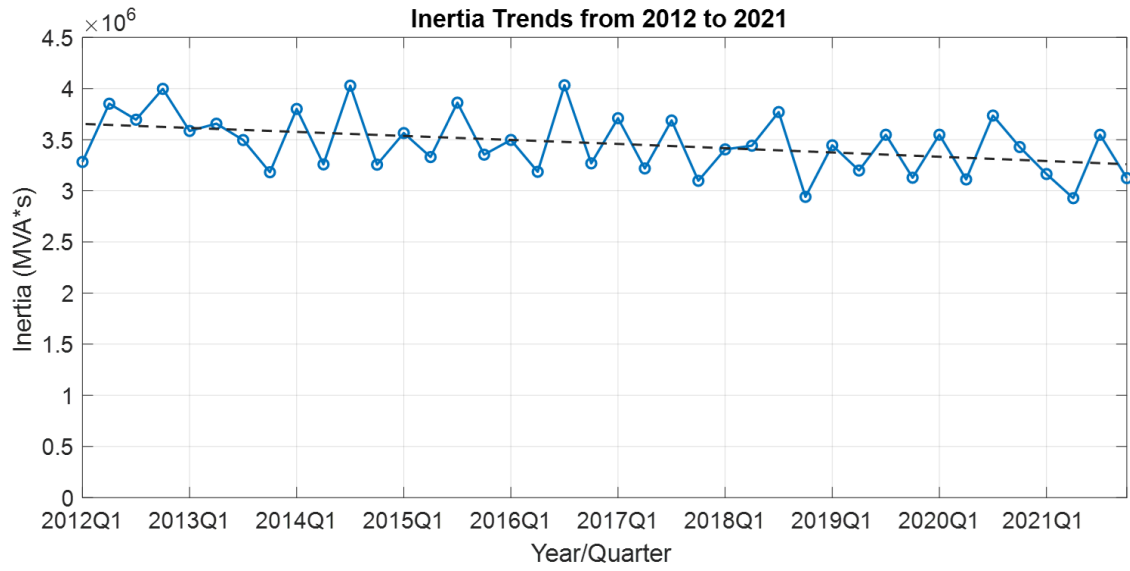


Figure 2-8 Trend of inertia in Eastern Interconnection from 2012 to 2021

2.4.1 Basics of the Calculation of Primary Frequency Response

The calculation of the interconnection primary frequency response also utilizes the median frequency curve introduced in section 2.2. The NERC frequency response standard background document has laid out the process of calculating the primary frequency [15]. As shown in Figure 2-2, point A is the start point of the generation trip event, point C is the frequency nadir, and point B is the settling frequency before AGC actions. The difference between frequency levels at A and C can be used to calculate the arrested frequency response, which is useful in directly determining the safety margin from under-frequency load-shedding thresholds. The difference between the frequency level at A and that at B is used to calculate the primary frequency response. It is noted that due to the large scale and strong inertial response of the Eastern Interconnection, the frequency level at point C is often very close or identical to point B, which means the inertia of the system is able to smoothly buffer typical power mismatches without an overshoot until the system reaches the steady state determined by the strength of the primary frequency response.

With a number of generation trip events in a certain time period, the primary frequency response estimation can be formulated as an over-determined system of linear equations, and the best estimate can be made with the least-squares method:

$$\hat{\beta} = (\Delta \mathbf{F}^T \Delta \mathbf{F})^{-1} \cdot \Delta \mathbf{F}^T \cdot \mathbf{MW}$$

$$\Delta \mathbf{F} = [\Delta f_1, \Delta f_2, \dots, \Delta f_n]^T = [\Delta f_1, \Delta f_2, \dots, \Delta f_n]^T \quad (2-7)$$

$$\mathbf{MW} = [MW_1, MW_2, \dots, MW_n]^T$$

where $\hat{\beta}$ is the estimated primary frequency response, $\Delta \mathbf{F}$ is the vector comprised of frequency deviations in the generation trip events, $\Delta f_i = \Delta f_{Ai} - \Delta f_{Bi}$ is the frequency deviation of generation trip event i , \mathbf{MW} is the vector comprised of generation trip MW

sizes, MW_i is the size of the generation trip i , and n is the number of events.

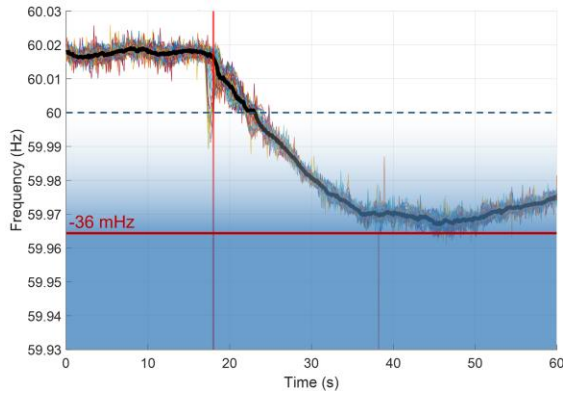
2.4.2 Impact of Governor Dead-Bands and Event Specifications

1) Role of governor dead bands in the evaluation of primary frequency response β

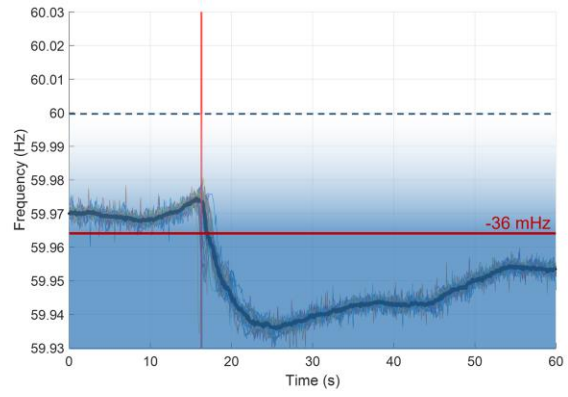
Unlike the inertial response that is inherent and instant due to the electromagnetic tie between the rotating mass and the electric grid, the primary frequency response is mainly due to the control actions from generator governors and advanced converter control of frequency-responsive renewables if enabled. These control mechanisms typically have dead bands built-in to prevent frequent actions that increase the chances of instability and tear and wear to the equipment [14]. In the Eastern Interconnection, the NERC standard requires the dead band setting in frequency-responsive conventional generators to be tighter than the maximum allowable range of ± 36 mHz [18].

The existence of governor dead bands makes the evaluation of the trend of the primary frequency response more complicated than inertia. Figure 2-9 shows an illustration of how the distribution of dead bands impacts the primary frequency response an event receives.

The shade of blue in both subplots in Figure 2-9 indicates the amount of primary frequency response mobilized. The deeper the frequency dives, the more governor dead bands will be trespassed, leading to a stronger primary frequency response as indicated by the deeper shade of blue. When the system frequency is near 60 Hz, most of the governors are not in action since the frequency is within their dead bands, and hence the area has the lightest shade of blue. As compliant with NERC's requirement of the largest allowable dead band of 36 mHz, dead bands of most frequency-responsive generators are exceeded at $f = 59.964$ Hz and all available primary frequency response resources have been actively engaged, leading to the deep blue shade at and below the 36 mHz deviation.



(a) High starting frequency



(b) Low starting frequency

Figure 2-9 Dead-bands and event frequency dynamics

This means the primary frequency response a disturbance event receives will be different depending on which frequency range it travels through, even if the system has the same primary frequency response portfolio. Since the frequency drop within the deeper blue area experiences more ‘resistance’ as more primary frequency response is engaged, a disturbance event with a larger portion of its frequency dynamics in the deeper blue area will experience a stronger primary frequency response. For example, the event presented in Figure 2-9. (a) starts at around 60.02 Hz and its whole frequency dynamics are above the NERC lower dead band setting limit of 59.964 Hz. In contrast, the event in Figure 2-9.(b) starts at 59.976 Hz, which is already close to the 59.964 Hz line. This means a large portion of the frequency dynamics of event (a) is close to a free fall in its first tens of mHz of decline, and governor actions are slowly engaged as it reaches its nadir. It is a very different situation for event (b), as its starting frequency is already at where most of the governors have been engaged. Almost the whole frequency decline of event (b) is ‘resisted’ by the largest available governor response from the beginning of the process. It is foreseeable that the primary frequency response calculated using events (a) and (b) will yield drastically different conclusions about the primary frequency response of the system.

The consecutive generation trip events in Figure 2-10 are a good instance for demonstrating the impact of governor dead bands on the evaluation of primary frequency response. These events happened on August 11, 2019, only 36 seconds apart in the Eastern Interconnection. The first event has a generation trip size of 645 MW and the second of 950 MW. It is worth attention that the Δf_2 caused by the 950 MW trip in event #2 is significantly less than the Δf_1 by the smaller 650 MW trip in event #1, which defies the positive correlation as expected between MW and Δf . This leads to significantly different

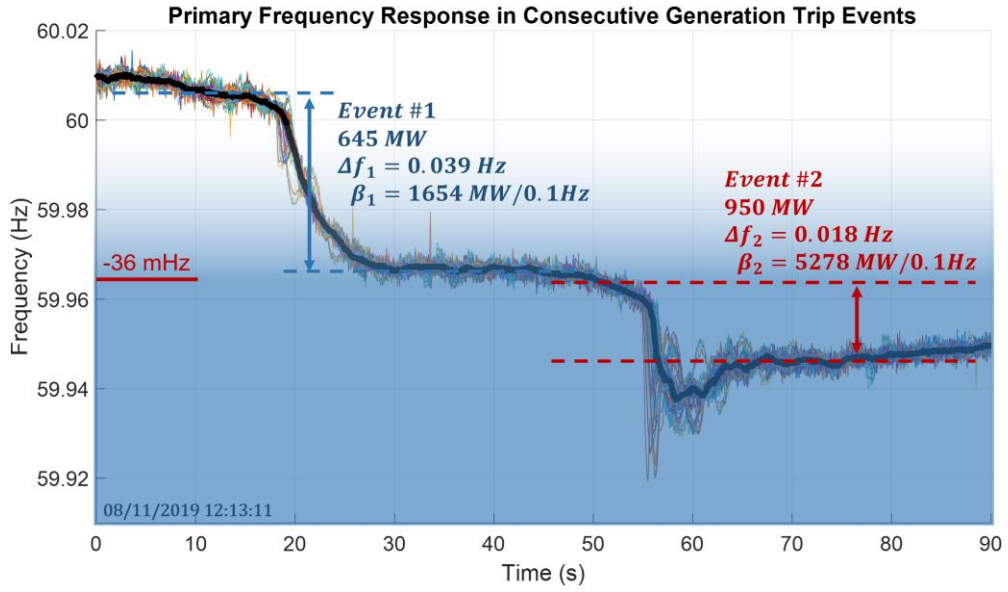


Figure 2-10 Primary frequency response in consecutive generation trip events

strengths of primary frequency response:

$$\begin{aligned}\beta_1 &= \frac{645 \text{ MW}}{0.039 \text{ Hz}} = 1654 \text{ MW}/0.1\text{Hz} \\ \beta_2 &= \frac{950 \text{ MW}}{0.018 \text{ Hz}} = 5278 \text{ MW}/0.1\text{Hz}\end{aligned}\tag{2-8}$$

where β_1 and β_2 are strengths of the primary frequency response of the individual events.

With the extremely similar primary frequency response resources available at the time of event occurrences (only 36 seconds apart), the drastic difference in β_1 and β_2 ($\beta_1 \approx 320\% \cdot \beta_2$) well demonstrates the significant impact of the position of the frequency dynamics and the existence of governor dead bands on the strength of the primary frequency response a disturbance event receives. This has to be properly addressed before a consistent and fair comparison of primary frequency response across the years can be conducted.

Two most significant factors that impact how a frequency disturbance event receives primary frequency are:

- Starting frequency (frequency pre-disturbance)
- MW size of the disturbance

These factors largely determine when and how much governor response engages throughout the frequency dynamics, or intuitively, what areas the frequency curve travels through in Figure 2-9. The combination of small MW size and high starting frequency will lead to extremely low β since most of the frequency dynamics are in the lighter area, and the combination of large MW and low starting frequency will lead to extremely high β since most portion of the frequency dynamics are in the deeply shaded area where resistance from governor actions is abundant.

2) Impact of starting frequency and MW size on β

As discussed above, the distribution of dead band settings and the variations in disturbance event specifications can make the evaluation of the trend of primary frequency response inconsistent if no measures are taken in selecting the appropriate disturbance events for analysis.

The beta values shown in Figure 2-11 are calculated quarterly with equation (2-7) without screening the events for their starting frequency and MW size. The β obtained seems to have had a mild decline since 2012.

However, the distribution of individual event β has been widening in recent years, as indicated by the boxplot in Figure 2-12.

In addition to the wider range of β , the events in recent years also appear to be increasingly scattered on the $MW - \Delta f$ plane. For example, the $MW - \Delta f$ plot for 2020 events is presented in Figure 2-13.

It is noted the events are much more scattered than the $MW - RoCoF$ plot (Figure 2-6) in the same year. The correlation coefficient between MW and Δf in 2020 is 0.57. Conducting such correlation calculation for year 2012 to 2021 gives the trend shown in Figure 2-14.

It is noticeable that the correlation declined significantly in recent years, validating that the distribution of the events is indeed becoming more scattered on the $MW - \Delta f$ plane in recent years. The low correlation coefficient leaves the β trend in Figure 2-11 less trustworthy and even possibly misleading about the actual trend in β .

The reason behind the declining correlation lies in the change in data availability in the past decade. In earlier years (2012 to 2014), only generation trip events with

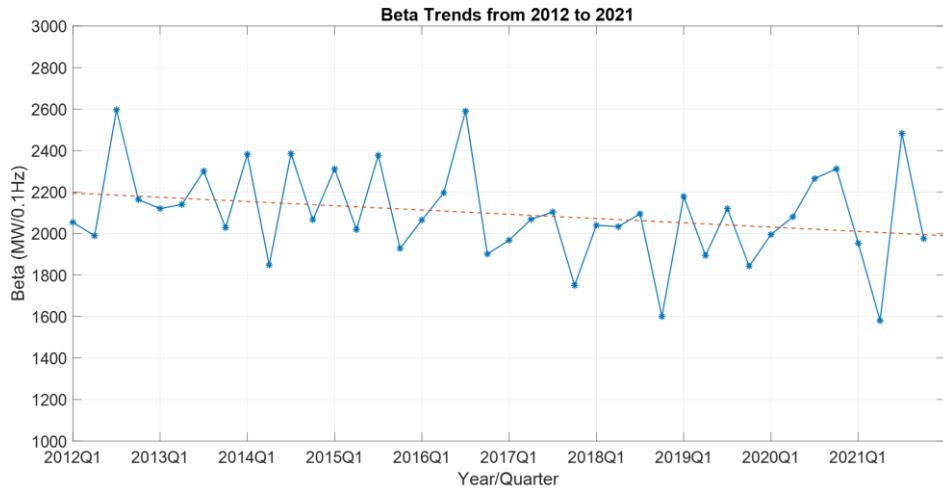


Figure 2-11 Beta Trends from 2012 to 2021 calculated with all events

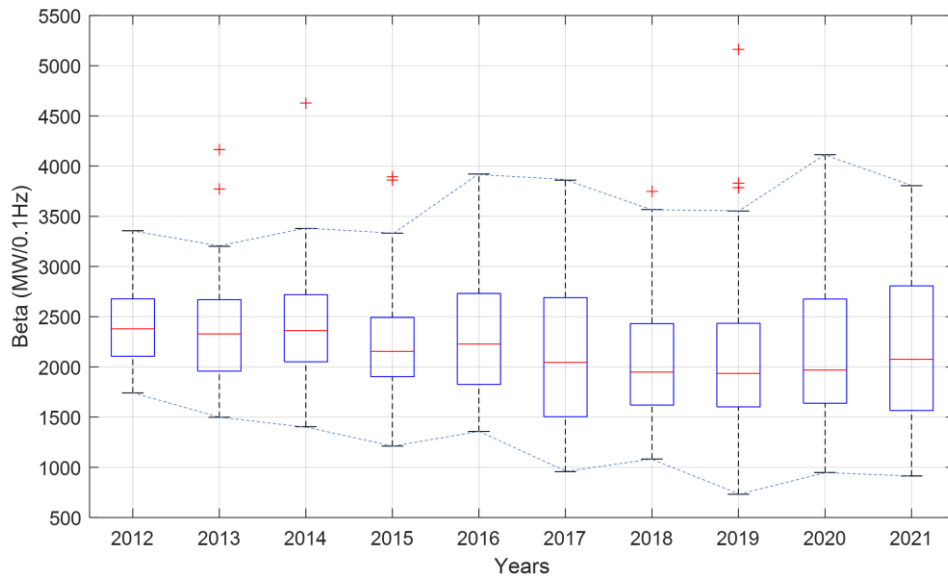


Figure 2-12 Boxplot of β values of individual events from 2012 to 2021

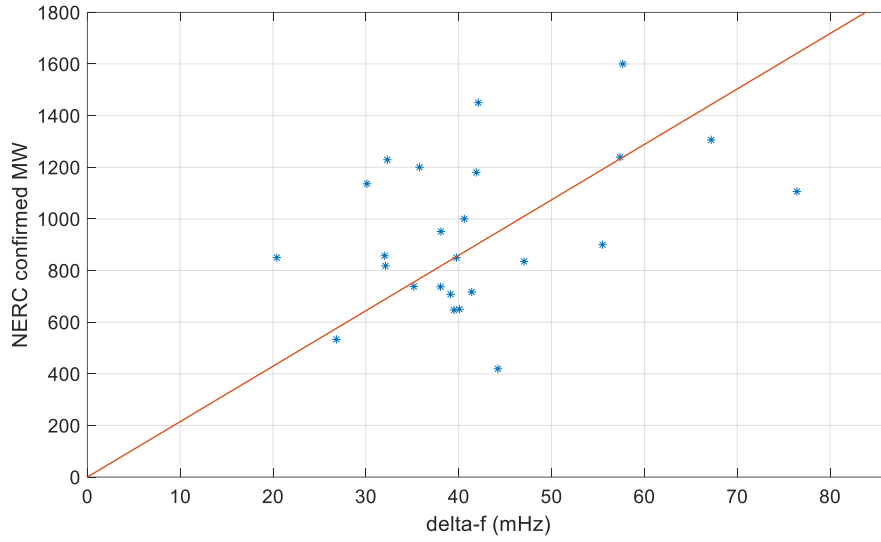


Figure 2-13 The $MW - \Delta f$ plot of events in year 2020

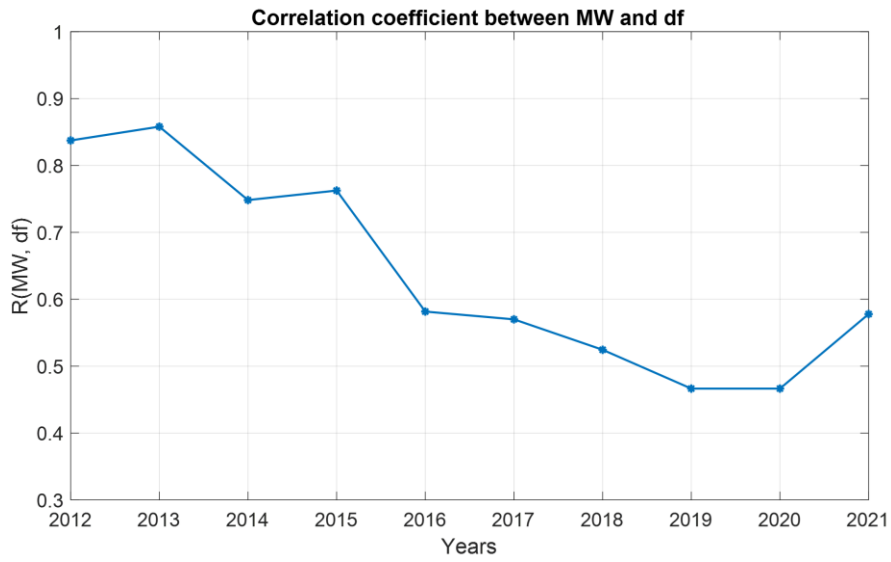


Figure 2-14 Correlation coefficient between MW and Δf

magnitudes greater than 1000 MW are reported, while in later years, events are being reported and logged with magnitudes of as low as 300 MW. Such change in data availability led to changes in two aspects: a) small MW events have more representation in later years than earlier years; b) starting frequencies are more diverse and the impact of it is aggravated by small MW sizes.

The impact of starting frequency and MW size of an event on the primary frequency response it experiences is validated in the figures below, which depict the correlation between the observed β and the two factors:

The β and starting frequency exhibited a moderate negative correlation in Figure 2-15. (a), which echoes the fact that events with lower starting frequencies engage primary frequency response earlier and stronger. The $\beta - MW$ exhibited a positive correlation that starts to phase out as the MW passes 800 MW. This is because larger disturbances have a larger chance to have the frequency dive deeper and engage more governors.

3) Event selection for consistent evaluation of the trend of primary frequency response

While the β value calculated for an individual generation trip event does represent the primary frequency response it received, it is less meaningful in indicating the underlying strength and capability of the primary frequency response of the interconnection over a certain period since the specification of the disturbance itself has a large impact on the dynamics it experiences. The same goes for the evaluation of $\hat{\beta}$ with equation (2-7) for a certain period. It is critical to filter the events based on their starting frequencies and MW sizes for a consistent evaluation of the β trend across the years.

First, a filter screening event for sizes larger than 800 MW is placed. According to Figure 2-9, an event of a larger MW size has larger frequency deviations, which avoids

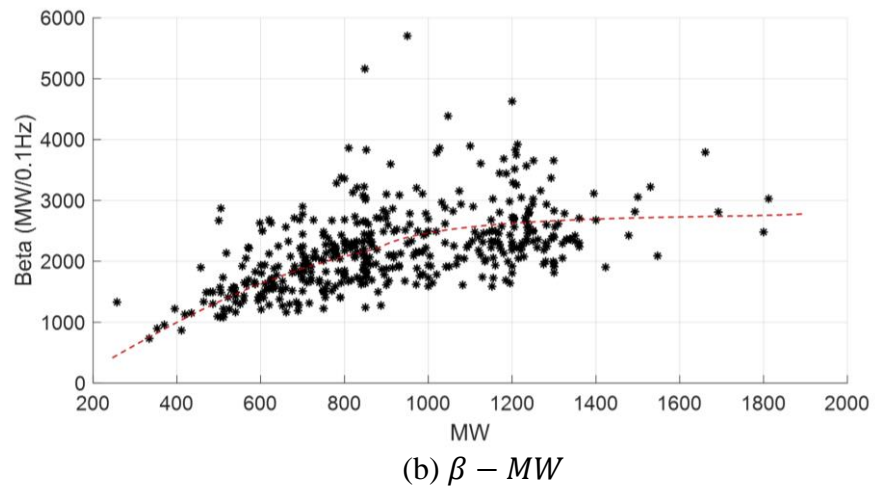
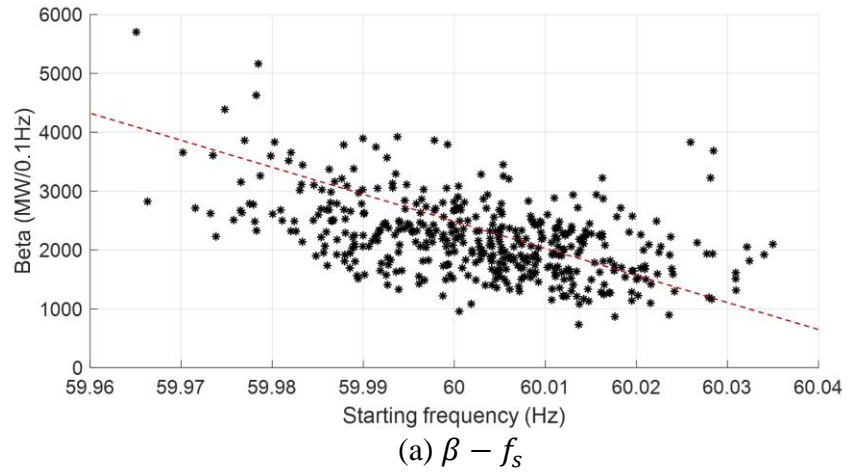


Figure 2-15 Plot of event β against starting frequency and MW size

events largely enclosed by the 36 mHz dead band box that leads to an unreasonably lower exhibition of β . This is also validated in Figure 2-15, where the observed β exhibits downward trend as the MW decreases.

Then, the second filter is placed on the starting frequency. Two choices were made in this study: a) starting frequency near the nominal frequency: $59.995 \text{ Hz} < f_s < 60.005 \text{ Hz}$; and b) low starting frequency $f_s < 59.990 \text{ Hz}$.

The first choice ($59.995 \text{ Hz} < f_s < 60.005 \text{ Hz}$) is intended for a standard evaluation of the trend of primary frequency response under typical events that have pre-disturbance frequencies close to the nominal. The primary frequency response obtained with criteria is noted as β_0 in the following text.

The second choice ($f_s < 59.990 \text{ Hz}$) is to reveal the trend of the primary frequency response when most resources available are mobilized, noted as β_+ . This is to exclude the impact of dead bands as much as possible by using only the events with low starting frequencies. Setting the filter lower than the 36 mHz NERC requirement (at 59.964 Hz) would be ideal, but there are not a sufficient number of such events since the Eastern Interconnection rarely operates at that low frequency. The choice of the 59.990 Hz is a compromise between the event availability and low-frequency criteria. However, it is noted that most of the gas-fired generators are configured to have governor dead bands between 10 to 17 mHz. A starting frequency at or below 59.990 Hz will have most of the governors of gas units activated at the beginning of the disturbance, and the 36 mHz maximum allowable dead band limit can be easily crossed at the early stage of the events.

2.4.3 Trends of Primary Frequency Response with Event Filters

1) β_0 from events with near nominal frequency ($59.995 \text{ Hz} < f_s < 60.005 \text{ Hz}$, $MW > 800$)

The application of this event filter mitigates the impact of the governor dead bands by using large events starting near the nominal operating frequency of 60 Hz. It represents the typical scenario where the events start from the nominal frequency with little ‘resistance’ due to the dead bands and then experience increasing engagement of governor reactions as the frequency declines. The range of starting frequency from 59.995 Hz to 60.005 Hz facilitates a fair comparison across the years in the past decade. The correlation coefficient between the event MW size and the frequency deviation, which is used as an indicator of the effectiveness and consistency of the trending comparison, improved significantly after the application of the event filter, as shown in Figure 2-16.

The trend of primary frequency response obtained with generation trip events with $59.995 \text{ Hz} < f_s < 60.005 \text{ Hz}$, $MW > 800$ is shown in Figure 2-17.

The overall trend of the primary frequency response β_0 is significantly different from that calculated without the event filter in Figure 2-11. It showed an upward trend in the past decade that led to a 14.73% increase from 2268.51 MW/0.1Hz in the early years (2012 to 2014) to 2602.70 MW/0.1Hz in recent years (2019 to 2021). The application of the filter on MW size and starting frequency greatly mitigated the impact of governor dead bands and disturbance specifications on the observation of primary frequency response, and the true upward trend in β_0 is revealed. Explanations for the increase in β_0 will be given in section 2.4.4.

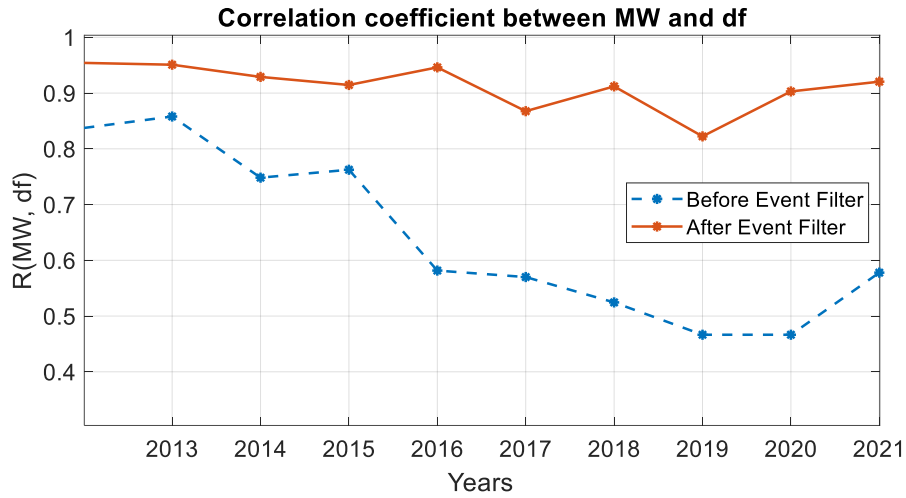


Figure 2-16 Correlation coefficient – events with near nominal f_s

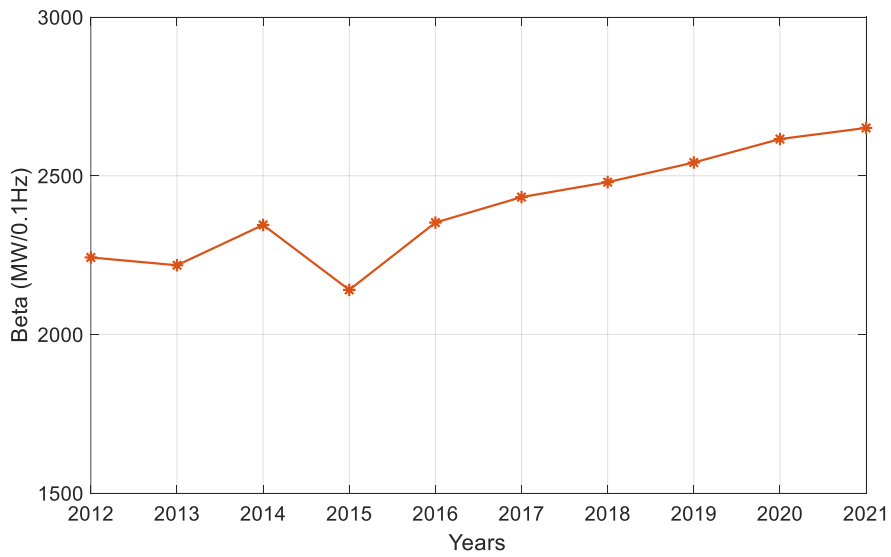


Figure 2-17 The trend of primary frequency response β_0

2) β_+ from events with low starting frequency ($f_s < 59.990 \text{ Hz}$, $MW > 800$)

By setting the starting frequency filter for $f_s < 59.990 \text{ Hz}$, the calculated β_+ demonstrates the trend in Eastern Interconnection's primary frequency response when most of the available frequency-responsive resources are mobilized. It further excludes the impact of the uncertainties in the engagement of governors during the transients as a large portion of the governors have been activated before the event starts and the rest are to be engaged very quickly as the event proceeds.

The correlation coefficient (red solid curve in Figure 2-18) after the application of the filter improved significantly compared to that before the filter (blue dash curve) and stayed consistently higher than 0.80 from 2012 to 2021. This indicates the filter effectively reduced the impact of governor dead bands on the observation of β .

The trend of primary frequency response β_+ obtained with these low-starting-frequency events is shown in Figure 2-19. It is noticed that the primary frequency response when most available resources are mobilized, β_+ (calculated with low-starting-frequency events), sees an even stronger increase in the past decade. The average β_+ in recent years (2019 to 2021, 3460.71 MW/0.1Hz) has increased by 22.61% compared to that in 2012 to 2014 (2822.54 MW/0.1Hz). This can be explained by the evolution in the generation mix in the Eastern Interconnection.

2.4.4 Explanation for the Increase In Primary Frequency Response

The authors expected that the primary frequency response of the interconnection must have necessarily weakened over time as thermal generators retire and more renewables are integrated. The above data shows that this relationship has not manifested in the EI. Instead, its β value has strengthened. The authors believe this trend is associated with the

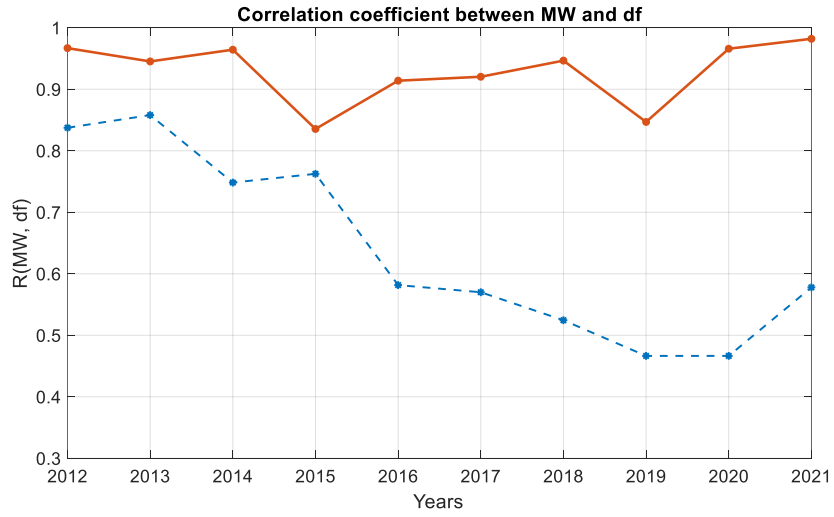


Figure 2-18 Correlation coefficient – events with low f_s

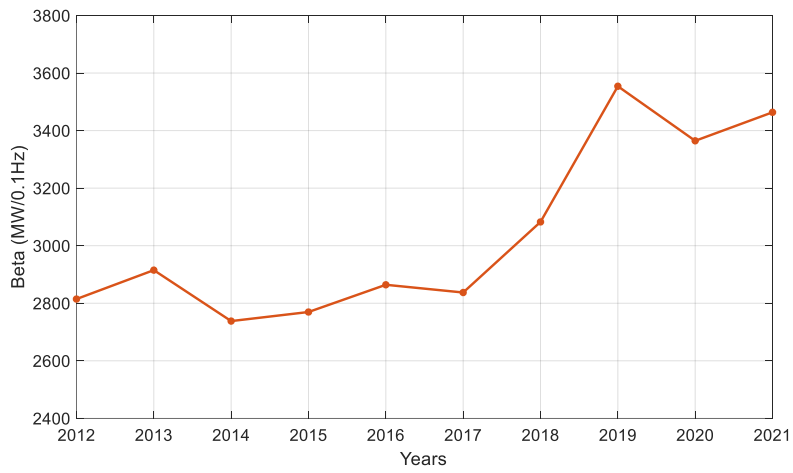


Figure 2-19 The trend of primary frequency response β_+

evolution of the EI's fuel mix – especially the proliferation of gas-fired generation and its generally enhanced frequency regulation features. The electricity generation from coal, natural gas, solar, and wind is plotted in Figure 2-20 based on data from the U.S. Energy Information Administration [1]. The changes in the generation of these fuel types are summarized in Table 2-2.

The total generation from all fuel types remained stable in the past decade. The retirement of coal-fired plants led to a -45.36% decrease in its generation in the past decade. This is replaced mainly by newly commissioned gas-fired plants and renewables like solar and wind. The increase in gas generation is 380004 GWh, which compensates for 69.5% of the reduction in coal generation. The increase in solar (45380 GWh) and wind (95227 GWh), together, picked up 25.7% of the decrease in coal generation.

The gas-fired generator governors are typically configured to have tighter dead bands (10-17 mHz) and stiffer droop curves (4% droop) than coal generators (36 mHz, 5% droop) [18], [61]. These settings make the overall primary frequency response engage faster and deeper in recent years. Such effect is well demonstrated in Figure 2-19 with the strong increase in β_+ , and is also visible, though to a lesser extent, in Figure 2-17.

2.5 Improved Event MW Estimation

Through the trending analysis of primary frequency response, it is learned that the distribution of governor dead bands can be a critical factor that impacts the response an event receives from the system. Two major specifications of an event that interact with the dead bands are the starting frequency and the MW size of the event – the former determines the number of governors engaged at the beginning of the event and the latter determines the amount and timing of governors to be engaged throughout the frequency dynamics.

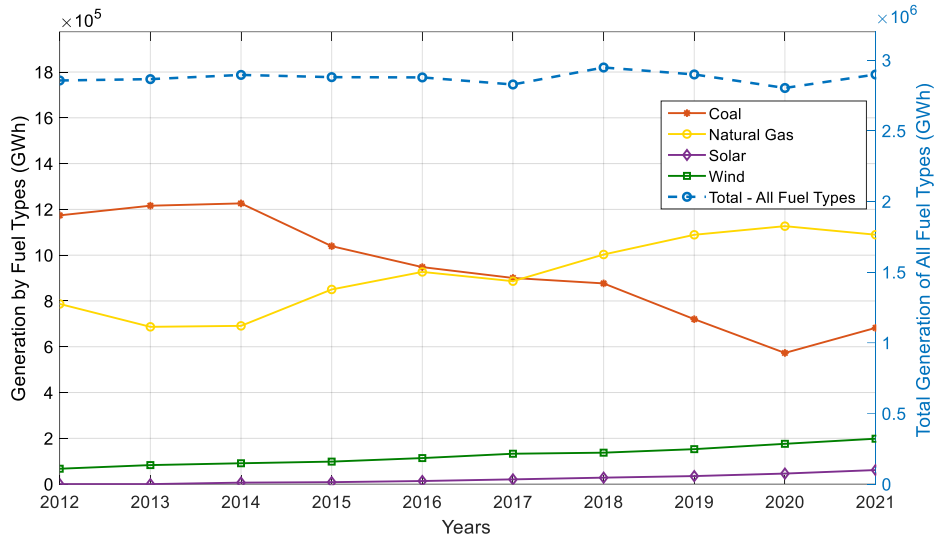


Figure 2-20 Generation in Eastern Interconnection by fuel types

Table 2-2 Changes in Generation of Coal, Gas, Solar, and Wind

Fuel Type	Average GWh 2012-2014	Average GWh 2019-2021	Difference (GWh)	Percentage Change (%)
Coal	1205412	658618	-546794	-45.36%
Gas	721755	1101759	380004	52.65%
Solar	2161	47541	45380	2099.95%
Wind	80479	175706	95227	118.33%
All	2871989	2866356	-5633	-0.19%

Based on such understanding, one can anticipate a relationship between the strength of the primary frequency response an event elicits and these two specifications of the event. The following investigations aim to reveal such a relationship and utilize it for improving the accuracy of event MW size estimations.

2.5.1 Overview

Current online MW estimation takes a recent average β for calculation of the MW estimate with the observed frequency deviation Δf :

$$MW_{est} = \beta_{avg} \cdot \Delta f \quad (2-9)$$

This formulation does not acknowledge the impact of the event specifications themselves on the exhibition of the strength of primary frequency response (β). Using the average value of β has the advantage of straightforward implementation, but it compromises accuracy. With the knowledge of factors that impact the exhibited β , there is an opportunity to use historical event data for constructing a quantitative relationship between the β and two major event specifications, f_s and MW, through curve-fitting. The quantified relationship will help improve the prediction of the β values for specific events, and thus lead to more accurate MW size estimations.

Assume the strength of primary frequency response (β) could be expressed as a function of the event specifications f_s and MW:

$$\hat{\beta} = \beta(f_s, MW) \quad (2-10)$$

Incorporating this into the MW estimation equation will lead to:

$$MW_{est} = \hat{\beta}(f_s, MW_{actual}) \cdot \Delta f \quad (2-11)$$

where starting frequency f_s and frequency deviation Δf can be obtained from online

synchronized measurements, and MW_{actual} is an unknown quantity. It is noted that in equation (2-11), the size of the event is the quantity to be estimated (MW_{est}), and yet at the same time, it is a factor that impacts the β value, which is part of the estimation equation (noted as MW_{actual}). To solve equation (2-11), two routes can be pursued:

- Option 1: Estimate $\hat{\beta}$ with f_s information only;
- Option 2: Unify MW_{est} and MW_{actual} as one variable: MW, and then estimate $\hat{\beta}$ and MW at the same time by converting the formulation into an iterative process that simultaneously optimizes the estimation of both quantities.

These two options will be both implemented and compared in terms of estimation accuracy. First, the relation between β and f_s, MW is quantified to prepare for the MW estimation. Then, such quantified relation is applied in the MW estimation process. FNET/GridEye data from 2018 to 2019 are used for parameter calibration through curve fitting, and data from 2020 and 2021 are used for performance evaluation.

2.5.2 Formulation of the MW Estimation Problem

To formulate the MW estimation problem, the relation between β and f_s, MW needs to be integrated into the estimation process. This starts with the quantification of the relation. With a number of generation trip events, the relation between the strength of primary frequency response, β , and the two factors, f_s and MW , can be obtained through curve-fitting. Plots in Figure 2-21 and Figure 2-22 show the patterns among the quantities.

There is a negative correlation between β and starting frequency f_s , which aligns with the analysis in section 2.4. The higher the starting frequency, the later and less governor reaction will be engaged during the transient, and thus the lower the strength of primary

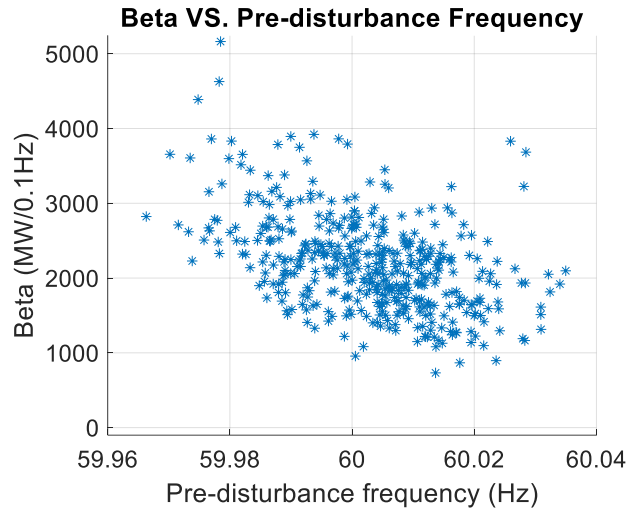


Figure 2-21 Relationship between β and starting frequency

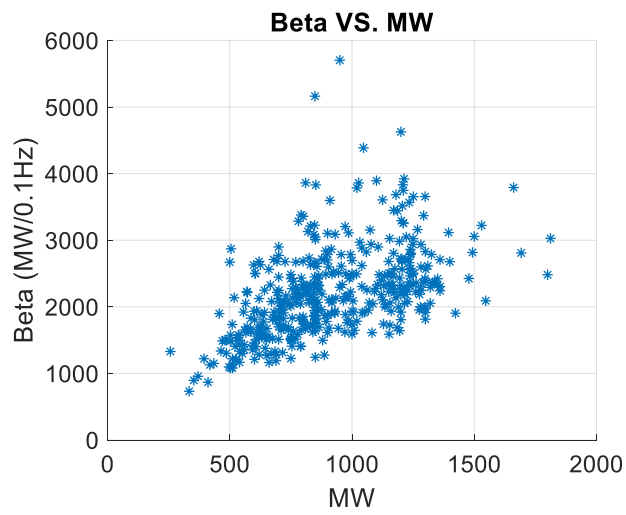


Figure 2-22 Relationship between β and event MW size

frequency response (β), and vice versa. On the contrary, a positive correlation is observed between β and MW . The larger the MW size of the event, generally the wider the range that the system frequency travels through, activating more governors by passing their dead bands. But it should be noted that these two event specifications, starting frequency and MW , are closely coupled, meaning their impact cannot be separated since they act together in the interaction with numerous governors. The overall effect of them, however, can be approximated through curve fitting. During curve fitting, the orders of variants f_s and MW can be determined by both how good the fitting is (correlation coefficient) and how the fitted curves perform in the MW estimation algorithms, as a higher correlation coefficient does not automatically guarantee better fit due to over-fitting issues.

Option 1 relies on the relationship between β and starting frequency f_s , disregarding the impact of MW on the observed β . Thus, the MW estimation becomes:

$$MW_{est} = \hat{\beta}(f_s) \cdot \Delta f \quad (2-12)$$

The correction to β becomes a single variant function in relation to f_s . As both f_s and Δf can be readily measured from event frequency dynamic curves, MW_{est} can be calculated according to (2-12) once a curve-fitting is done to capture the function $\hat{\beta}(f_s)$. Although this option leaves out the impact of MW on β observation, it greatly simplifies the estimation process.

Option 2, in contrast, treats the MW_{actual} as the same variable as MW_{est} , and attempts to solve all quantities together. This way, equation (2-11) becomes:

$$MW_{est} = \hat{\beta}(f_s, MW_{est}) \cdot \Delta f \quad (2-13)$$

Depending on the complexity of the function of $\hat{\beta}(f_s, MW_{est})$ obtained from fitting historical data, this equation can be either solved directly or through numerical/iterative

solutions. As the curve fitting result of the function $\hat{\beta}(f_s, MW_{est})$ can vary from system to system, a numerical solving process based on the Newton-Raphson method is proposed as a general solution.

2.5.3 Solving MW Estimation Equations

(a) Option 1

For option one, where the β value is predicted solely based on the starting frequency f_s , the solution to the MW estimation is straightforward once the $\beta - f_s$ correlation is determined with curve-fitting on historical data. With the FNET/GridEye historical data from 2018 to 2019, the $\beta - f_s$ correlation is identified as $\beta = -564.9 f_s + 2186$. The MW can be easily solved with the following equation, where the frequency deviation Δf can be observed from the measurement.

$$MW_{est} = (-564.9 f_s + 2186) \cdot \Delta f \quad (2-14)$$

where the starting frequency f_s is normalized with a mean of 60 and a standard deviation of 0.01315.

(b) Option 2

In option 2, the prediction of β is based on not only the starting frequency but also the MW size, which is the quantity to be estimated. Depending on the complexity of the fitted curve of $\hat{\beta}(f_s, MW_{est})$, solving (2-13) can be challenging. A general solution to equation (2-13) based on the Newton-Raphson method is proposed. First, an auxiliary function is defined based on equation (2-13):

$$g(f_s, MW_{est}, \Delta f) = MW_{est} - \beta(f_s, MW_{est}) * \Delta f \quad (2-15)$$

Once the frequency transient is captured through measurement, the starting frequency f_s and the frequency difference Δf can be obtained, then function $g(f_s, MW_{est}, \Delta f)$ will become a single variant function of MW_{est} . The solution of equation (2-13) will be a root of $g(f_s, MW_{est}, \Delta f) = 0$. The root can be reached iteratively with the following update rule until convergence:

$$MW_{n+1} = MW_n - \frac{g(f_s, MW_n, \Delta f)}{g'(f_s, MW_n, \Delta f)} \quad (2-16)$$

Depending on the curve-fitting result of function $g(f_s, MW_{est}, \Delta f)$, there could be multiple roots to $g(f_s, MW_{est}, \Delta f) = 0$, as shown illustratively in Figure 2-23.

In such a situation, an appropriate selection of the starting point of the iterative process is critical in finding the optimal solution. Since the measurement has captured frequency dynamics that include the first few seconds following the event, the RoCoF of the event can be calculated. The calculated RoCoF, together with average system inertia, can be used to provide an educated choice of the initial point MW_0 for the iterative process:

$$MW_0 = RoCoF \cdot H_{avg} \quad (2-17)$$

where $RoCoF$ is the calculated rate-of-change-of-frequency of the event, and H_{avg} is the average inertia for the system.

2.5.4 EI Case Study and Performance Comparison

To evaluate and compare the performance of different MW estimation methods, FNET/GridEye historic data from years 2018 to 2019 are used for curve-fitting to find the correlation between β and factors that affect it (116 events). The relation between β and f_s, MW through curve-fitting is given in Table 2-3. Data from years 2020-2021 (59 events) are used for the evaluation of the performance of different estimation methods.

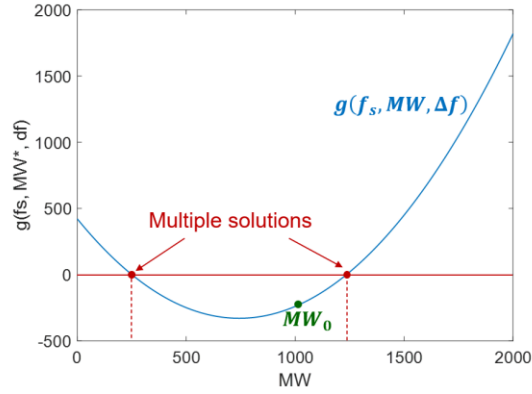


Figure 2-23 Multiple roots to the auxiliary function

Table 2-3 Curve-fitting results for EI with FNET/GridEye data

Curve-fitting orders	$\beta(f_s, MW_{est})$ (MW/0.1Hz)
$f_s - 0, MW - 0$ (Average β approach)	2186
$f_s - 1, MW - 0$ (Option 1)	$-564.9f_s + 2186$ *where f_s is normalized by mean 60 and std 0.01315.
$f_s - 1, MW - 1$ (Option 2)	$-474.8f_s + 398.2MW_{est} + 2186$ *where f_s is normalized by mean 60 and std 0.01315, and MW_{est} is normalized by mean 875 and std 260.1
$f_s - 1, MW - 2$ (Option 2)	$-166.1MW_{est}^2 - 130.2MW_{est}f_s - 432.7f_s + 450.5MW_{est} + 2321$ *where f_s is normalized by mean 60 and std 0.01315, and MW_{est} is normalized by mean 875 and std 260.1
$f_s - 1, MW - 3$ (Option 2)	$-21.91 MW_{est}^3 + 80.94MW_{est}^2f_s - 162.8MW_{est}^2 - 151.5MW_{est}f_s + 513.7MW_{est} - 484.1 f_s + 2316$ *where f_s is normalized by mean 60 and std 0.01315, and MW_{est} is normalized by mean 875 and std 260.1
$f_s - 2, MW - 2$ (Option 2)	$-120.2MW_{est}^2 - 47.76MW_{est}f_s + 166.7f_s^2 + 418.2MW_{est} - 374.9 f_s + 2129$ *where f_s is normalized by mean 60 and std 0.01315, and MW_{est} is normalized by mean 875 and std 260.1

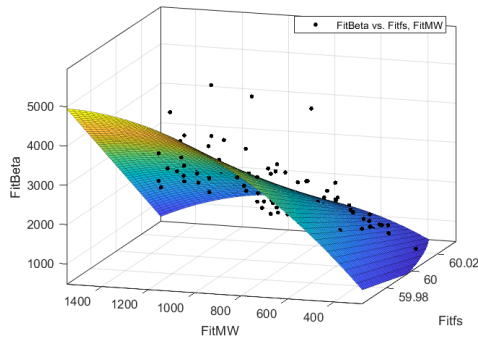
The first column shows the orders used in the curve-fitting for starting frequency and MW size. When the curve-fitting orders for both quantities are 0, it represents the average β approach. When the configuration is $f_s - 1, MW - 0$, it is used for option 1 – using only the starting frequency for β correction. When the curve-fitting orders for both quantities are equal to or larger than 1, it falls into the category of option 2, for which the Newton-Raphson solution can be applied to find the MW estimation. A comparison of the estimation accuracies is provided in Table 2-4.

Compared to the average β approach, all other methods that take advantage of β correction with f_s and MW showed consistently better MW estimation results in terms of both the average MW error and standard deviation. The MW estimation error was reduced by 28% through option 1 ($f_s - 1, MW - 0$) compared to the average β approach. Among the option 2 attempts, the ($f_s - 1, MW - 2$) case showed the best MW estimation result. It reduced the MW estimation error by 34% compared to the average β approach and gave the most consistency in estimation accuracy as indicated by the smallest standard deviation of 111.1 MW.

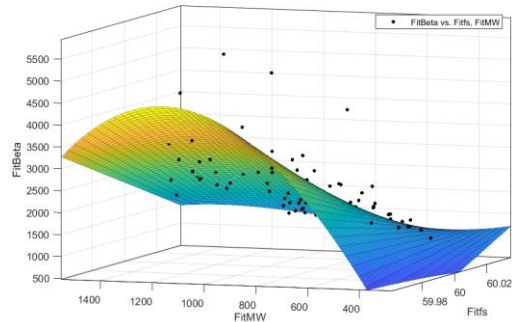
This can be explained by the approximately linear correlation between β and f_s in the Eastern Interconnection (Figure 2-21) and the approximately quadratic correlation between β and MW (Figure 2-22). It is noted that when the order of the variant MW increases to three, the performance notably deteriorated. This is caused by the overfitting of the impact of MW on β . Shown in Figure 2-24 is a comparison of the fitted surfaces with the orders of the variant MW being 2 and 3, while both of them have the first order for fitting the variant f_s . The surface of the 3rd-order MW aggressively lowered its β prediction in the low-MW, low- f_s area and over-estimated β in high-MW regions to include outliers.

Table 2-4 MW estimation accuracy of different estimation methods

Curve-fitting	Average $ MW \text{ error} $	$ MW \text{ error} $ Std
$f_s - 0, MW - 0$ (Average β approach)	264.0	167.7
$f_s - 1, MW - 0$ (Option 1)	189.5	130.6
$f_s - 1, MW - 1$ (Option 2)	184.6	127.5
$f_s - 1, MW - 2$ (Option 2)	173.1	111.1
$f_s - 1, MW - 3$ (Option 2)	195.3	148.2
$f_s - 2, MW - 2$ (Option 2)	206.2	149.5



(a) $f_s - 1, MW - 2$



(b) $f_s - 1, MW - 3$

Figure 2-24 Comparison of the fitted curves of different orders

In the Eastern Interconnection, the 1st-order- f_s , 2nd-order-MW curve-fitting gives the β correction formula that yields the best MW estimations. While in other interconnections the correlation between β and these factors can be different depending on the governor configurations, the proposed curve-fitting and Newton-Raphson approach can be applied to various $\beta - f_s, MW$ relations for improving the MW estimation accuracy.

2.6 Regional Frequency Dynamics

2.6.1 Purpose of Regional Dynamics Studies

With more than 200 synchronized frequency sensors deployed in North America, FNET/GridEye was able to monitor regional dynamics in a variety of locations. Such capability has led to online applications such as disturbance triangulation [43]. The abundance of sensors across vast geographical areas has also the potential to reveal regional frequency dynamics and inertial characteristics in the era of renewable integration.

As discussed previously in this chapter, the interconnection-level inertia remains more than sufficient despite the fact that it has been declining slowly in the past decade because of the changes in the generation mix. In today's interconnection, different regions are experiencing regional frequency dynamics and inertial characteristics due to their different connections to the rest of the interconnection as well as the nature of their generation mixes. Also, the development of renewable integration, among other changes to the mix, is usually uneven across the interconnection due to geographical, environmental, economic, and political considerations. Analysis of regional frequency dynamics and regional inertial characteristics is important for awareness of regional inertia sufficiency and provides insights into feasibilities and risks in future regional renewable developments.

As rotating masses are electrically connected, the local frequency dynamics observed are a composite result of the masses locally available, the electrical distance among the masses, the type/location of the disturbance, and the location of observation sensors. While it is difficult to depict a complete and precise picture of the regional dynamics with a limited number of disturbance events and sensors, these measurements can be informative on how the regionally available masses interact with the rest of the interconnection thanks to the widespread locations of the sensors across the system. This helps identify potential weak spots in the interconnection that are prone to severe regional frequency transients and oscillations. Hence, in this section, representative generation trip events for various regions within the Eastern Interconnection will be analyzed with a focus on identifying regional frequency dynamic characteristics and the inertial support available. For regions identified with weak regional inertial support, these results provide qualitative guidance for system planning. Regional inertia estimation methods based on probing or ambient measurement can be further leveraged in the future for more accurate inertia monitoring in these areas.

The rest of this section will cover sample events with locations across the Eastern Interconnection, including the Florida area, the Southeast, Mid-Atlantic, Northeast, Midwest, West Central, Central-Southeast, Upper Midwest, and West South Central.

2.6.2 Regional Dynamics in EI

(a) Florida

Florida has been known for a ‘loose’ connection to the rest of the Eastern Interconnection, which makes it prone to excitation of oscillations amid disturbances. In FNET/GridEye event database, the divergence of frequencies measured by sensors in Florida from the rest of the interconnection is the most evident.

Figure 2-25 shows the location of a sample generation trip of 1600 MW on the west central coast of Florida. As in Figure 2-26, strong local frequency deviations from the median frequency of the Eastern Interconnection (bold black curve) happened to locations near and within Florida in the first 10 seconds following the event occurrences. By taking a closer look at these regional dynamics, the information collected by FNET/GridEye sensors reveals details about the availability of local inertial response and inertial support from neighboring areas.

It is noticed in Figure 2-27 that all sensors in Florida experienced significantly stronger but consistent frequency decline in the first three seconds. The maximum frequency difference between Florida and the interconnection median reached 90 mHz at two seconds after the generation trip. This indicates a strong coherence among generators in Florida and a loose synchronization with the rest of the interconnection. The frequency nadir in Florida was followed by a strong overshoot that pushed the frequency of the Florida area 5 mHz above the interconnection median, which was the collective rotating mass in Florida swinging around the rest of the system. The swing persisted for two cycles before becoming negligible with a cycle of 4.467s. The swing had a significant impact on the frequencies in other southern states, including Georgia, South Carolina, Alabama, Arkansas, North Carolina, and Missouri.

The closest FNET/GridEye sensor is 70 miles away from the disturbance location, which recorded the largest RoCoF as shown in Figure 2-28. The local RoCoF and local inertia can be calculated with the frequency dynamics in the first episode of frequency decline before the bounce, as summarized in Table 2-5.

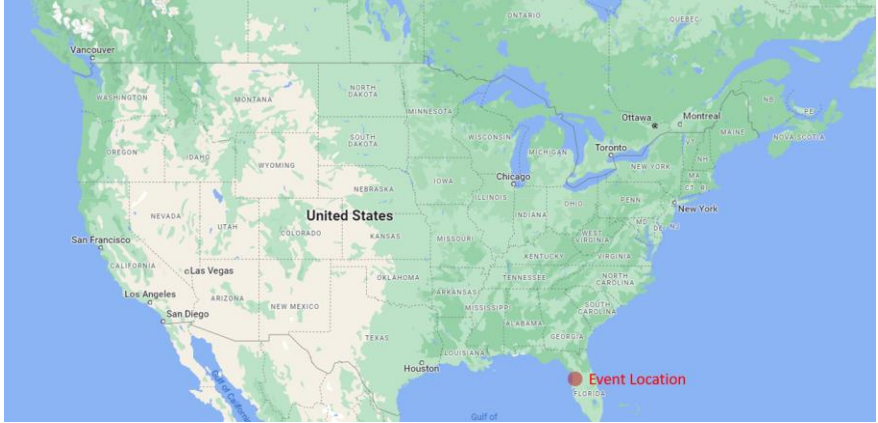


Figure 2-25 Location of the generation trip event in Florida

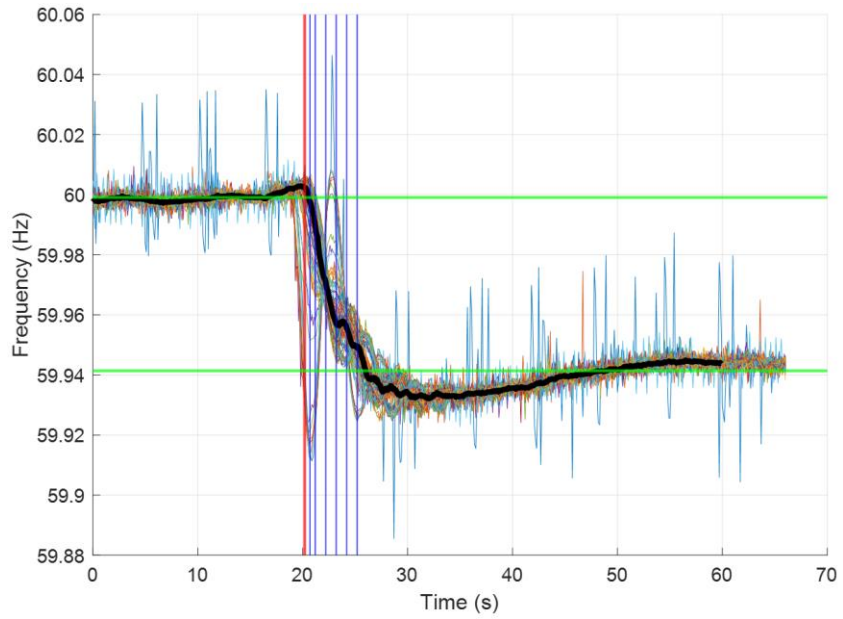


Figure 2-26 Frequency measurements captured by sensors in EI

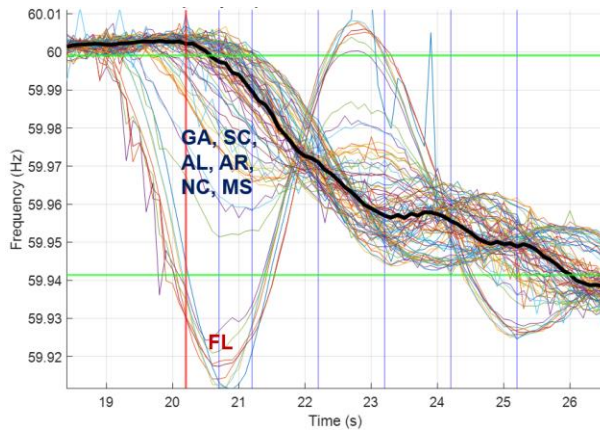


Figure 2-27 Frequency deviations in Florida and Southeast following a FL disturbance

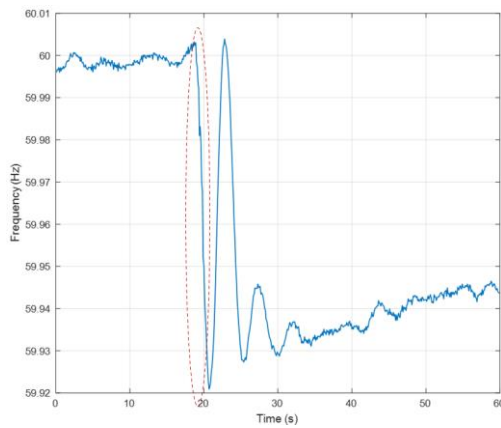


Figure 2-28 Frequency dynamics recorded by the closest sensor in Florida

Table 2-5 Frequency dynamic specifics from the event in Florida

Disturbance Location	Local RoCoF	Local Inertia	Interconnection Inertia	Inter-Area Inertial Support Arrival Time
FL	50.67 mHz/s	31.57 MJ/mHz	106.88 MJ/mHz	2.0 s

The inter-area inertial support arrival time from further regions is calculated by finding the time difference between the onset of the local frequency decline and the onset of the last frequency decline in the interconnection, which represents the region that responded to the event at the latest.

The regional inertia (measured in the first 1.4 seconds, before any inter-area inertial support arrives) is less than 30% of the total interconnection inertia. It should be noted that the ‘regional inertia’ measured this way included not only inertial response from the state of Florida, but also from southern states that experienced earlier frequency declines than the interconnection median frequency curve. Generators in these neighboring states can be electrically close and coherent with the rotating mass in Florida. It took 2.0 seconds for inertial supports from further regions to fully arrive.

(b) Southeast

A 1228 MW generation trip event in South Carolina and a 950 MW generation trip event in North Carolina are chosen as examples for the Southeast. Figure 2-29 shows the location of the two events and Figure 2-30 shows a close-up view of the frequency deviations following the events.

By extracting the RoCoF from the closest FNET/GridEye sensors’ measurement (located in Charleston, SC and Raleigh, NC), the local frequency dynamics are depicted in Figure 2-31, and specifications about local frequency dynamics and inertial characteristics are summarized in Table 2-6. Although the swing of the southeastern part of EI was not as severe as in Florida, it is noticed that the local inertia in both events (11.70 MJ/mHz, 6.24 MJ/mHz) was even lower than in Florida. The inter-area inertial support arrival time of the

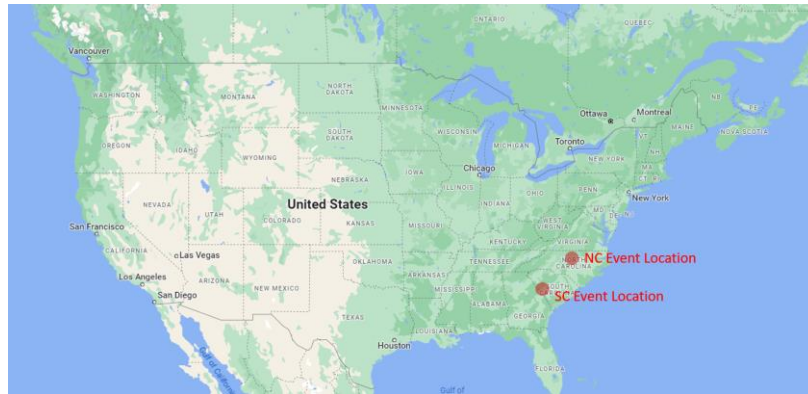
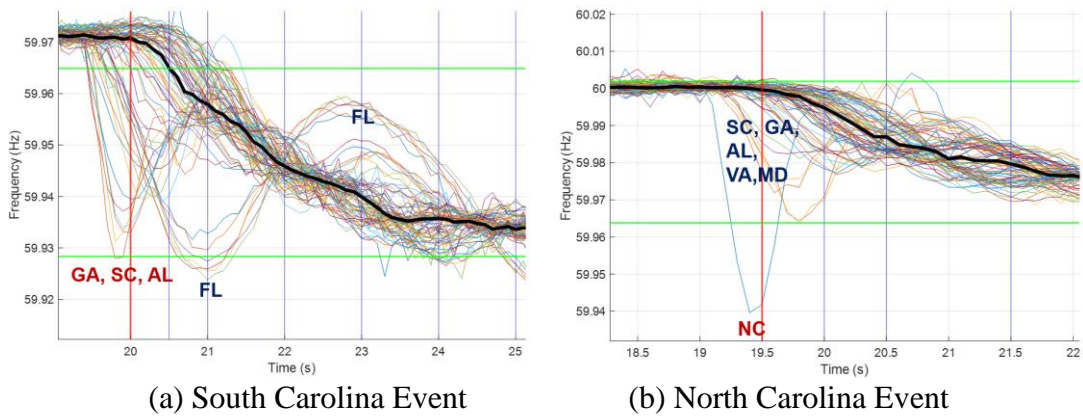


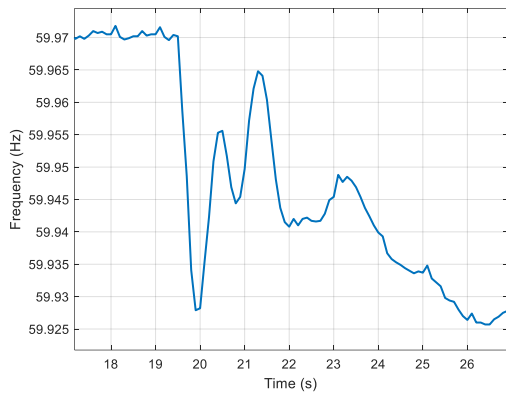
Figure 2-29 Location of the generation trip events in the Southeast



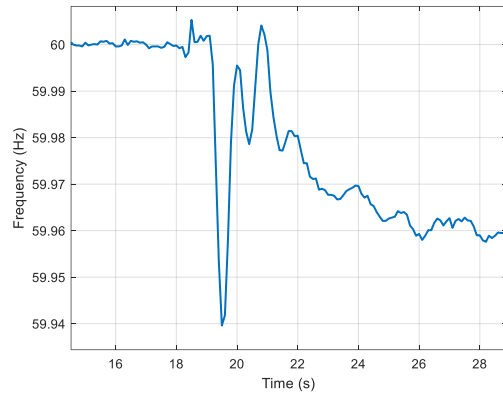
(a) South Carolina Event

(b) North Carolina Event

Figure 2-30 Frequency deviations following generation trips in Southeast U.S.



(a) South Carolina Event



(b) North Carolina Event

Figure 2-31 Frequency dynamics recorded by the closest sensors in SC and NC

Table 2-6 Frequency dynamic specifics from the event in Southeast U.S.

Disturbance Location	Local RoCoF	Local Inertia	Interconnection Inertia	Inter-Area Inertial Support Arrival Time
SC	105 mHz/s	11.70 MJ/mHz	124.04 MJ/mHz	1.2 s
NC	152 mHz/s	6.24 MJ/mHz	108.68 MJ/mHz	1.0 s

two southeastern events, however, were 1.2 seconds and 1.0 seconds. These are much shorter than that in the Florida case. which indicates that the immediately available local inertial response in the southeastern region was lower than in Florida, but the arrival of inter-area inertial support was much faster than that in Florida with more diverse and tighter connections to the rest of the interconnection. This led to a larger RoCoF but a fast stabilization of frequency dynamics in the Southeast than in Florida events. It is also worth noting that the event in South Carolina also excited the oscillatory behavior in Florida due to the relatively close disturbance location to Florida.

(c) Mid-Atlantic

A generation trip event of 910 MW in Pennsylvania is used here for a demonstration of the regional dynamics in Mid-Atlantic. Figure 2-32 shows the location of the event on the map, and Figure 2-33. (a) shows the frequency dynamics captured by FNET/GridEye sensors across the interconnection.

As New York and Pennsylvania sensors are closest to the disturbance, they are the first ones to experience the frequency dip with the largest RoCoF. Immediately followed NY and PA are Connecticut, Virginia, and Vermont. It is noted that Florida, although far away from the event location, exhibited oscillatory behaviors with a frequency of 0.225 Hz when the system starts to settle on the post-event frequency. This is due to the natural mode between the north and south coastal U.S.

With the closest sensor located in Williamsport, PA, the local frequency dynamics was captured as in Figure 2-33. (b). Specifications of the local dynamics are summarized in Table 2-7.



Figure 2-32 Location of the generation trip events in Mid-Atlantic

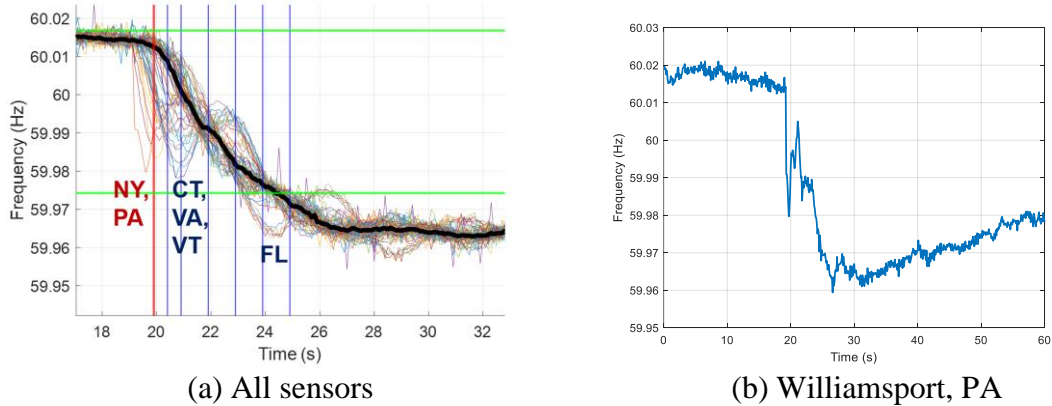


Figure 2-33 Frequency deviations following generation trips in the Mid-Atlantic

Table 2-7 Frequency dynamic specifics from the event in the Mid-Atlantic

Disturbance Location	Local RoCoF	Local Inertia	Interconnection Inertia	Inter-Area Inertial Support Arrival Time
PA	68 mHz/s	13.38 MJ/mHz	88.64 MJ/mHz	1.2 s

The Mid-Atlantic event exhibited strong regional dynamics with a local inertial response of 13.38 MJ/mHz, which is 15% of the total inertia at the time of event occurrence. Nearby inertial support from VA, CT, and VT responded quickly within 0.4 seconds, and it took 1.2 seconds for the rest of the system to respond to this disturbance. While the inertial support is received quickly, there have been oscillations sustaining for a long time due to the excitation of the Florida area's swing.

(d) Northeast

Since no appropriate event is found in the northeast-most corner of the Eastern Interconnection, a generation trip of 1270 MW in Upper New York State is used for approximate representation of Northeastern events, of which the location is shown on the map in Figure 2-34.

As shown in Figure 2-35, in the first three seconds, there is a 1 Hz oscillation of the northeast states (NY, VT, CT, MA) swinging around the rest of the system. Following this 1 Hz oscillation is the 0.25 Hz oscillation between the Northeast and Florida, which is similar to that observed in the Mid-Atlantic event in Pennsylvania.

Statistics about the frequency dynamics are summarized in Table 2-8. The local RoCoF observed by an FNET/GridEye sensor in Le Roy, NY is 107.67 mHz/s, which corresponds to a calculated local inertia of 11.79 MJ/mHz. This is 14% of the interconnection inertia level of 81.64 MJ/mHz at the time of event occurrence.

The inter-area support arrival time in this region is 1.7 seconds, which is on the high end and is due to the delayed arrival of support from the Florida area as their angle deviation increases in the first few seconds of the disturbance.



Figure 2-34 Location of the generation trip event in the Northeast

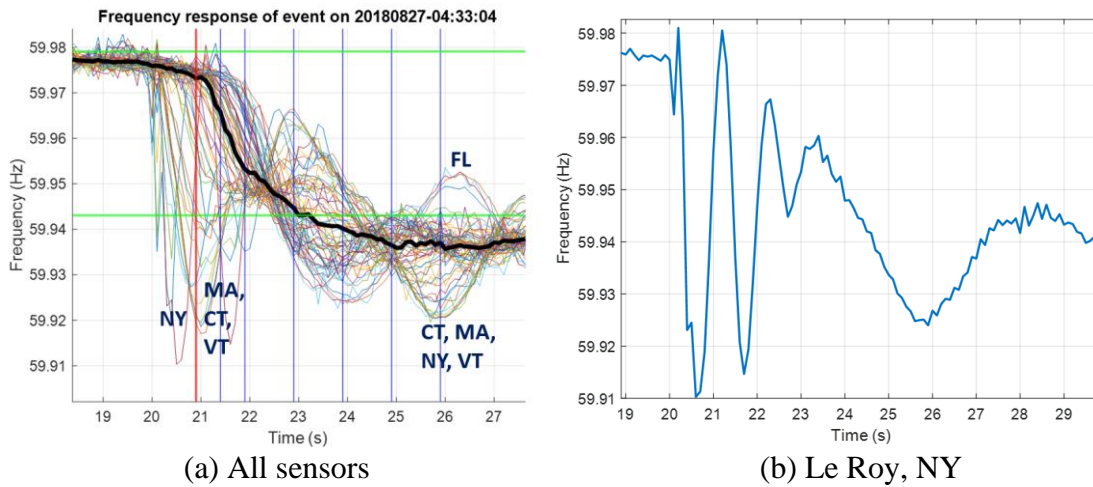


Figure 2-35 Frequency deviations following a generation trip in the Northeastern U.S.

Table 2-8 Frequency dynamic specifics from the event in Northeastern U.S.

Disturbance Location	Local RoCoF	Local Inertia	Interconnection Inertia	Inter-Area Inertial Support Arrival Time
NY	107.67 mHz/s	11.79 MJ/mHz	81.64 MJ/mHz	1.7 s

(e) Midwest

The sample event for the Midwest is a 915-MW generation trip in Illinois, as shown in Figure 2-36. While Iowa and Illinois had a large RoCoF from the beginning of the event, Wisconsin and other Midwest states also experienced strong frequency deviations from the interconnection median, but with a time delay. Through a closer look at the frequency dynamics captured by FNET/GridEye sensors, as in Figure 2-37, specifications of local dynamics and inertia from this Midwest event are summarized in Table 2-9.

The available local inertia is 21.96 MJ/mHz, about 19% of the total interconnection inertia. The inter-area inertial support for nearby regionals arrived in 0.4 seconds since the Iowa/Illinois area is tightly and diversly connected with a number of areas. The support from the further east coast took 1.2 seconds to arrive. The strong connection of the Midwest with the rest of the system is also demonstrated through the quick settlement of the oscillations following the disturbance. They settled within two dips with almost no overshoot.

(f) West Central

A generation trip event of 1200 MW in Kansas is used as an example of West Central events. The location of the event is shown in Figure 2-38, and the frequency dynamics in the first ten seconds following the disturbance are shown in Figure 2-39.

The FNET/GridEye sensor closest to the disturbance is in Kansas City, MO. The local frequency dynamics captured by this unit are shown in and specifications of the dynamics are summarized in Table 2-10.

States close to the disturbance experienced strong regional frequency dynamics immediately after the event occurrence, including KS, OK, MO, and AR. This is followed



Figure 2-36 Location of the generation trip event in the Midwest

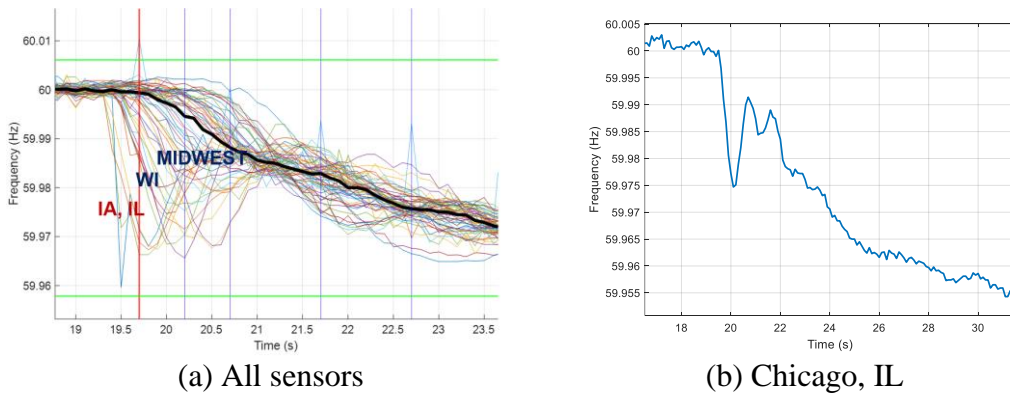


Figure 2-37 Frequency deviations following a generation trip in the Midwest

Table 2-9 Frequency dynamic specifics from the event in Midwest U.S.

Disturbance Location	Local RoCoF	Local Inertia	Interconnection Inertia	Inter-Area Inertial Support Arrival Time
IL	41.6 mHz/s	21.96 MJ/mHz	116.41 MJ/mHz	1.2 s



Figure 2-38 Location of the generation trip event in West Central U.S.

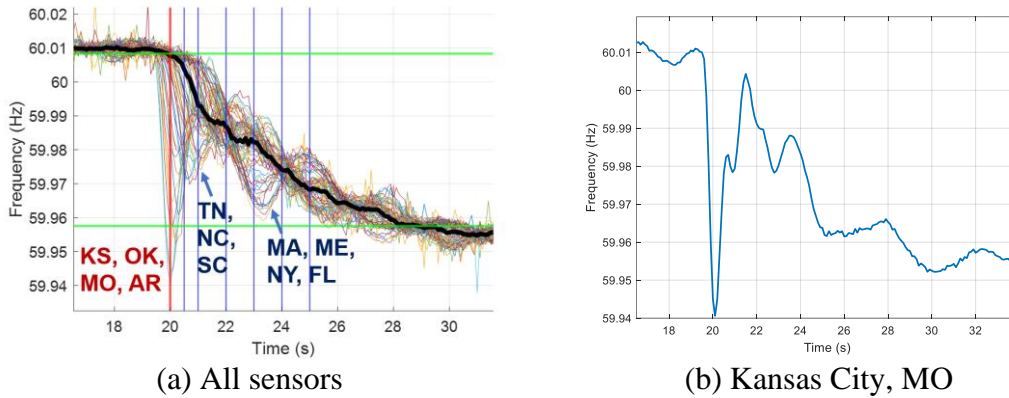


Figure 2-39 Frequency deviations following a generation trip in West Central U.S.

Table 2-10 Frequency dynamic specifics from the event in West Central U.S.

Disturbance Location	Local RoCoF	Local Inertia	Interconnection Inertia	Inter-Area Inertial Support Arrival Time
KS	116.67 mHz/s	10.34 MJ/mHz	133.33 MJ/mHz	1.0 s

quickly by support from TN, NC, and SC. While these states responded to the disturbance in 0.5 seconds, both the north and south coastal states (MA, ME, NY, FL) took about 1.0 second to respond to the disturbance and participated in an east-west oscillation mode.

Before any of the inter-area inertial support arrives, the local RoCoF measured was 116.67 mHz/s, leading to a local inertia of 10.34 MJ/mHz, 7.8% of the interconnection inertia (133.33 MJ/mHz).

(g) Central-Southeast

A generation trip of 800 MW that happened in Tennessee is used as an example for the central-southeast region. Figure 2-40 shows the location of the event on a map, and Figure 2-41 shows the frequency dynamics recorded at the time of event occurrence. Specifications of the local dynamics is summarized in Table 2-11.

The local inertia of this region was 22.99 MJ/mHz, which was 19% of the total interconnection inertia level at the time of event occurrence. While this is not significantly higher than other regions, it is noticed that the local frequency deviation is smaller compared to other areas, and less oscillation is experienced in this region. This is due to the diverse connection of the TVA area with the rest of the interconnection thanks to its central location in the Eastern Interconnection.

(h) Upper Midwest

The Upper Midwest sample event is a generation trip of 689 MW in North Dakota, of which the location is shown on the map in Figure 2-42. The frequency dynamics captured by FNET/GridEye are plotted in Figure 2-43. (a) and specifications are summarized in Table 2-12. It is noticed that states in the Upper Midwest U.S. unanimously experienced the frequency decline with the deepest in ND, MN, IA, and WI. The frequency drop in



Figure 2-40 Location of the generation trip event in Central-Southeast U.S.

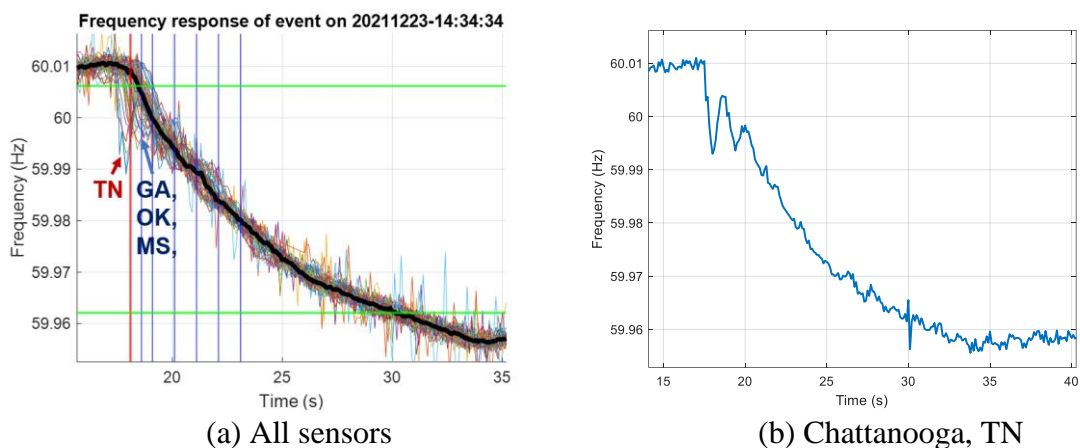


Figure 2-41 Frequency deviations following a generation trip in Central-Southeast U.S.

Table 2-11 Frequency dynamic specifics from the event in Central Southeast U.S.

Disturbance Location	Local RoCoF	Local Inertia	Interconnection Inertia	Inter-Area Inertial Support Arrival Time
TN	34.80 mHz/s	22.99 MJ/mHz	120.60 MJ/mHz	1.1 s



Figure 2-42 Location of the generation trip event in Upper Midwest U.S.

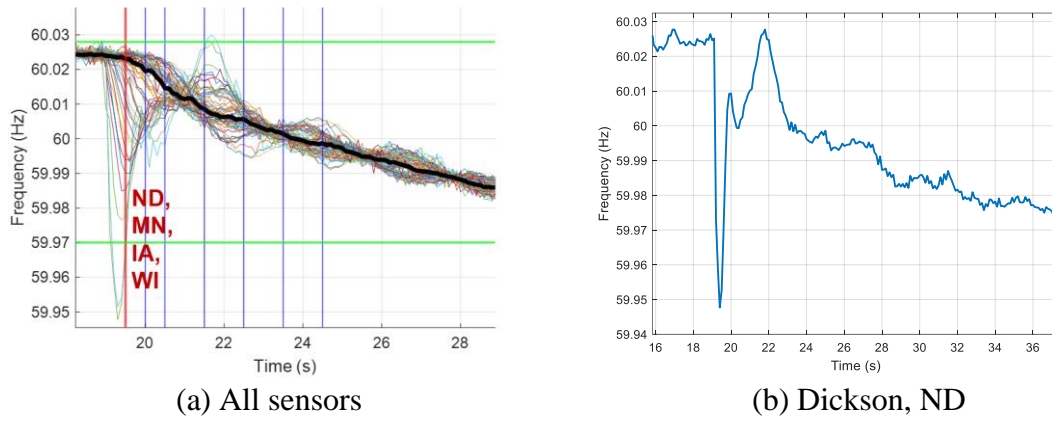


Figure 2-43 Frequency deviations following a generation trip in Upper Midwest U.S.

Table 2-12 Frequency dynamic specifics from the event in Upper Midwest U.S.

Disturbance Location	Local RoCoF	Local Inertia	Interconnection Inertia	Inter-Area Inertial Support Arrival Time
ND	258 mHz/s	2.67 MJ/mHz	119.48 MJ/mHz	1.6 s

North Dakota was the most drastic, for which a close-up view of the dynamics is shown in Figure 2-43. (b).

The Upper Midwest region showed very strong regional dynamics that led to a very low regional inertia of 2.67 MJ/mHz, 2.23% of the total interconnection inertia of 119.48 MJ/mHz. This is mainly because the area is in the Northwest corner of the Eastern Interconnection with a small capacity and weak connection with the rest of the system. While the inter-area inertial support from nearby areas arrived as soon as 0.3 seconds, it took significantly longer (1.6 seconds) for the majority of the inter-area support from the east coast to arrive. The RoCoF before inter-area support arrival reached as high as 258 mHz/s. Such high RoCoF could trigger loss-of-main protections, regional dynamics should be considered for future planning, especially when it involves large-scale integration of renewables in this area.

(i) West South Central

A generation trip of 770 MW in Mansfield, Louisiana is used as an example for events in the West South Central Region, of which the location is shown in Figure 2-44. The frequency dynamics captured by FNET/GridEye are plotted in Figure 2-45. (a). It is noticed that sensors in the West South Central area, including Arkansas, Missouri, and Oklahoma responded to the disturbance (there is no FNET/GridEye sensor in Louisiana).

The regional dynamics are extracted from the frequency recording collected closest to the disturbance sensor location in Little Rock, AR (Figure 2-45. (b)), as summarized in Table 2-13. The measured local inertia of 24.06 MJ/mHz, as measured by the sensor in Little Rock, AR, is only 16.7% of the interconnection inertia. However, it should be noted that this is an over-estimated local inertia (under-estimated local dynamics) due to the lack



Figure 2-44 Location of the generation trip event in the West South Central region

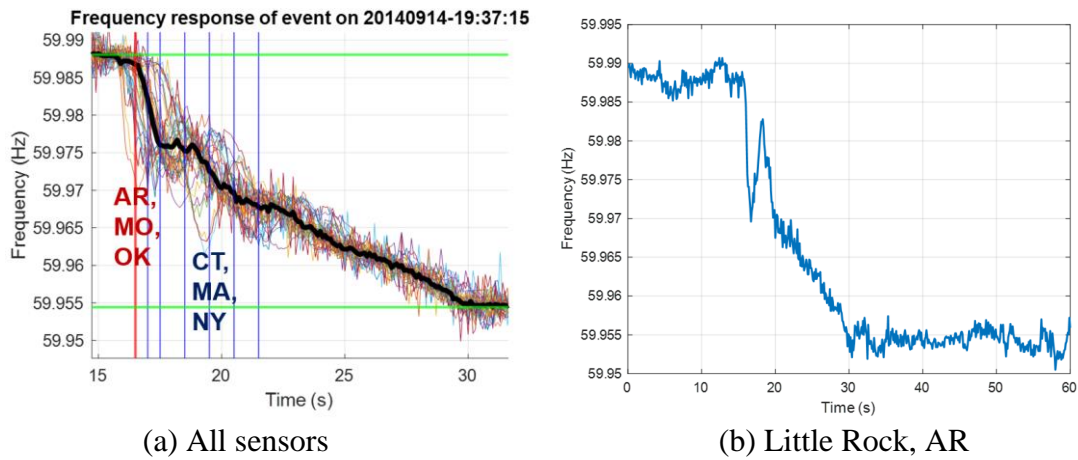


Figure 2-45 Frequency deviations following a generation trip in West South Central U.S.

Table 2-13 Frequency dynamic specifics from the event in West South Central U.S.

Disturbance Location	Local RoCoF	Local Inertia	Interconnection Inertia	Inter-Area Inertial Support Arrival Time
LA	32 mHz/s	24.06 MJ/mHz	144.38 MJ/mHz	1.7 s

of sensors in Louisiana. The inter-area support from the Northeast took 1.7 seconds to arrive and caused oscillations between the areas.

2.6.3 Summary of Regional Dynamics in EI

Specifications of the regional dynamics from these sample events are listed in Table 2-14 and an intuitive display of the regional dynamic characteristics is presented in Figure 2-46. Regional frequency dynamics have been observed across the Eastern Interconnection thanks to the widely available FNET/GridEye sensors. Findings regarding regional inertia are summarized as follows:

- Strong regional frequency dynamics have been observed across the interconnection, but different regions showed significantly distinct characteristics.
- Regional inertia value observed from local FNET/GridEye sensors can be significantly lower compared to the interconnection inertia in the first 0.5 seconds (2% - 30%) across the system when no inter-area inertial support has arrived.
- Regional RoCoF is impacted by both how much regional inertia is available locally and how diversely the region is connected to the rest of the interconnection. Areas on the edge of the interconnection tend to experience stronger regional dynamics and more oscillatory behaviors due to the loose connection and delayed support arrival.

The Upper Midwest region is the most prone to significantly high RoCoF levels (258 mHz/s), while the Florida area is the most prone to oscillations and long delays in inter-area support. As the Upper Midwest has abundant wind resources [62], and the Florida area has the highest solar irradiance (GHI) [63], special considerations shall be given with regards to the regional dynamics and oscillations when more renewables are integrated in these areas.

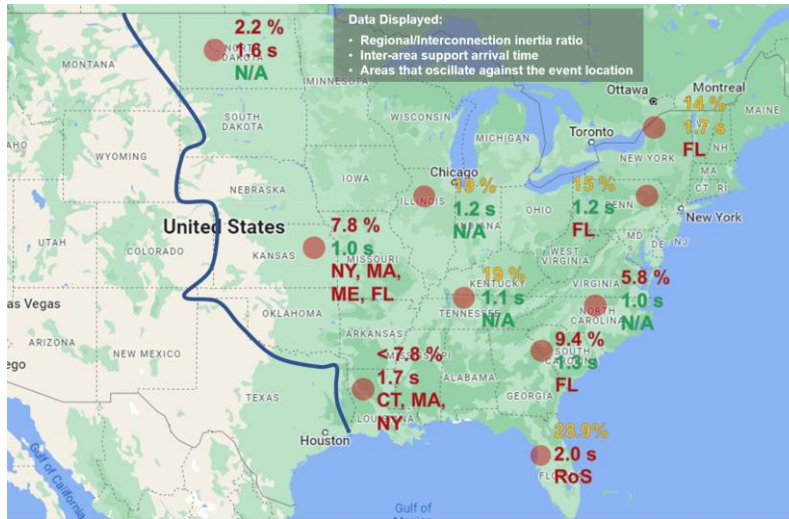


Figure 2-46 Display of regional dynamic characteristics across EI

Table 2-14 Specifications of the sample events across EI

Disturbance Location	Local RoCoF (mHz/s)	Local Inertia (MJ/mHz)	Interconnection Inertia (MJ/mHz)	Local to Interconnection Inertia Ratio	Inter-Area Inertial Support Arrival Time
FL	50	31.57	106.88	29.54%	<u>2.0 s</u>
SC	105	11.70	124.04	9.43%	1.2 s
NC	152	6.24	108.68	5.74%	1.0 s
PA	68	13.38	88.64	15.09%	1.2 s
NY	108	11.79	81.64	14.44%	1.7 s
IL	42	21.96	116.41	18.86%	1.2 s
KS	117	10.34	133.33	7.76%	1.0 s
TN	35	22.99	120.60	19.06%	1.1 s
ND	<u>258</u>	<u>2.67</u>	119.48	<u>2.23%</u>	<u>1.6 s</u>
LA	32	24.06	144.38	16.66%	<u>1.7 s</u>

Note: The inertia unit MJ/mHz can be converted to MW·s with: 1 MJ/mHz = 30000 MW·s

- Although the regional RoCoFs can be significantly more severe than the interconnection median, the strong interconnection support of inertial response and primary frequency response have successfully arrested the regional frequency deviations and kept the frequency well above the typical under-frequency load shedding setting of 59.50 Hz (59.70 Hz in Florida).
- Areas that experience extremely low local inertia have the risk of approaching typical RoCoF protection triggers of generation resources (150 mHz/s – 500 mHz/s). This shall be taken into account in the process of configuring newly integrated generation resources in these areas.
- It should be noted that the locations of disturbance and sensor could impact the regional dynamics observed. Analysis of more events is needed in the future to help even out these uncertainties and yield clearer regional dynamic characteristics.

2.7 Summary

Methods and results of the inertial and primary frequency response of the Eastern Interconnection are presented. The analysis takes advantage of the historical measurement data from the FNET/GridEye, which possess an abundance of synchronized distribution-level sensors in the Eastern Interconnection.

Since the existence of governor dead bands and specifications of an event (starting frequency and MW size) have a paramount role in the observed primary frequency response, event filters have been used to choose appropriate events for the trending analysis of primary frequency response. The value of β_0 , which is calculated with typical generation trip events that happen near the nominal operating frequency of 60 Hz, saw an increase of

14.73%. The value of β_+ , which is calculated with low starting frequency events and represents the response when most of the frequency-responsive resources are mobilized, exhibited a strong increase of 22.61%. Such a significant increase in primary frequency response is unexpected considering the increasing integration of renewables. An explanation is the replacement of coal units with gas units that provides stronger primary frequency response with stiffer droops and tighter dead bands. The scale of the gas-coal swap is much larger than the renewable (solar and wind) integrations. These results and conclusions can be useful information for power system operators and authorities to consider in system operation and corrective planning.

Although governor actions will inevitably influence the evaluation of interconnection-level inertial response due to the lengthened RoCoF calculation window, the impact would lean towards over-estimation of the inertial response since the primary frequency response over this same period has strengthened significantly. Together with the observed decline of 10% in inertial response, the authors believe it is safe to conclude that the actual inertial response has been declining in the past decade by *at least* 10%.

Based on the knowledge obtained about the correlation between the strength of primary frequency response to generation trip events, an improved MW estimation method is proposed by correcting β values for individual disturbance events based on their specifications of the starting frequency f_s and the MW sizes. Curve-fitting is leveraged to capture the correlation between these quantities and the Newton-Raphson method is used to solve the MW estimation problem iteratively. FNET/GridEye historical data are used for curve-fitting/parameter tuning, as well as performance evaluation. The proposed method significantly improved both the accuracy and consistency of MW estimation.

Regional frequency dynamics are studied with sample disturbance events across the Eastern Interconnection. Areas at the edge of the interconnection are the most prone to low regional inertia and exhibit more oscillatory behaviors. The Upper Midwest is identified to have the lowest local inertia (highest local RoCoF) and Florida is identified to be the most loosely connected with long inter-area support arrival time and abundant oscillatory behaviors. Additional attention is advised for the integration of new generation resources in these areas due to the highly active regional transients.

CHAPTER 3. MEASUREMENT-BASED WIDE-AREA DAMPING

CONTROL – TERNA CASE STUDY

As the Continental Europe Synchronous Area power interconnection experiences an even faster and deeper generation mix change compared to the Eastern Interconnection, its declining inertia and increasing occurrence of inter-area oscillation are pressing issues for the system. The north-south inter-area oscillations have been more frequently observed in recent years, especially during light-load, high-renewable midnights with low inertia levels. This chapter introduces the design, implementation, and testing of a measurement-based wide-area damping controller for the TERNA (an Italian Transmission System Operator) case study. After the hardware-in-the-loop verification in this study, the controller is now being tested in the field at the TERNA control center.

It should be noted that part of the content in this chapter is from the author's conference paper submitted to the 2021 IEEE Power & Energy Society General Meeting (PESGM) [47]. It should also be noted that sensitive information such as bus numbers are altered or redacted in compliance with confidentiality requirements.

3.1 Introduction

While large power grid interconnections improve the resiliency and efficiency of transmission networks, inter-area oscillation events are becoming more frequent in power systems and pose a significant threat to system stability and security amid the rapid generation mix change with increasing renewable integrations [5], [6].

For example, the Continental Europe Synchronous Area has been experiencing low inertia conditions frequently in recent years, especially during the light load period in the

midnights when the wind generation is high. The correlation between the reducing inertia and the occurrence, as well as severity, of inter-area oscillations in the Continental Europe Synchronous Area was discussed in [64]. One instance of these oscillation events is the December 3rd, 2017 event in the Continental Europe system, as shown in Figure 3-1. The oscillation mode of 0.293Hz between the north (France) and the south (Southern Italy) was excited by two consecutive generator disconnections [4].

To increase damping to inter-area oscillations and improve small signal stability, two major categories of inter-area oscillation damping schemes are available: a) local information based damping strategies; b) wide-area measurement-enabled damping schemes. Local information based damping strategies take advantage of the existing power system stabilizers (PSS) or FACTS/HVDC systems by introducing additional controls to increase the damping of the target oscillation modes [65], [66]. However, the performance of local information based inter-area oscillation damping control has been deteriorating as renewable penetration increases, which makes system operation conditions more volatile. The location of the existing actuators, in relation to the oscillation mode of interest, can also be a significant limit to the damping performance.

With the rapid deployment of phasor measurement units (PMUs) in the past decades, wide-area damping controllers (WADCs) utilizing remote synchronized measurements have the potential to be more effective in suppressing inter-area oscillations than local power system stabilizers due to higher observability and controllability [67], [68]. A variety of equipment can be used as actuators, such as generators, HVDC links, FACTS devices, and IBRs [6], [69-72]. Traditional wide-area oscillation damping control design methods rely on power system models linearized around specific operation points for

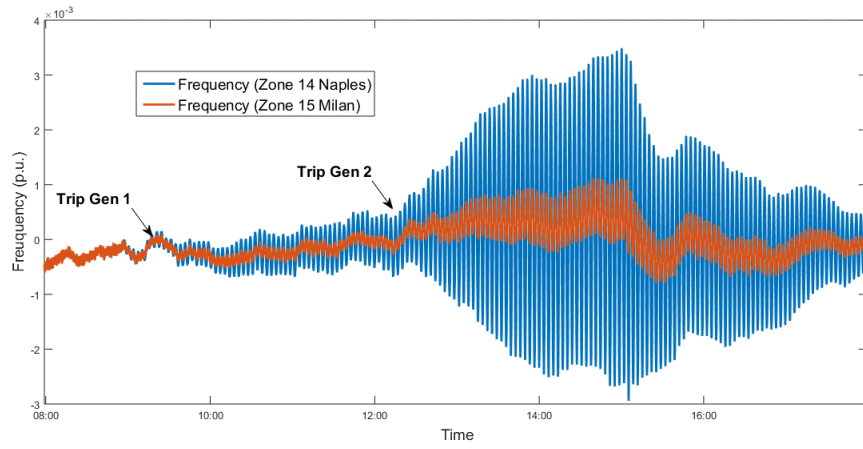


Figure 3-1 The December 3rd, 2017 event dynamics as observed in Naples and Milan

modal analysis. The accuracy of the power system models and load/resource forecasting, as well as the changes in operation conditions, can become overly challenging for the design of such controllers as the renewable penetration level continues to climb rapidly.

Hence, the work in this dissertation aims at a wide-area damping control scheme that is based on a measurement-driven-model design philosophy with the capability to adapt to system operating conditions and can be implemented on hardware controllers for real-time execution. The measurement-based method actively constructs and updates low-order transfer function models based on streaming measurements [73]. As the system operating condition changes, the transfer function model of the power system can be updated in real-time with timestamped synchrophasor measurements. This frees the controller parameter design from fixed, and possibly inaccurate, power system models, and paves the pathway to fully automated adaptive controllers.

First, the determination of the optimal controller input signal and control actuator is introduced. Then, a measurement-based transfer function model is constructed to simplify the representation of the system, which also provides the basis for the design of the parameters of the controller. The WADC has been implemented on the CompactRIO system, a general-purpose controller provided by National Instruments (NI) for prototyping [74]. A HIL testing platform, including a real-time power system simulator and network impairment simulator, was constructed to emulate realistic operating conditions with various types of communication network uncertainties and impairments. The hardware controller has been tested thoroughly under realistic operating conditions, such as measurement error, communication uncertainties, etc. in the HIL setup. The controller has been enhanced with several auxiliary function modules that were implemented and

validated during the testing phase to ensure satisfactory performance of the WADC under realistic operating conditions.

3.2 Design of the Wide-Area Damping Scheme

3.2.1 Choice of Control Input

The selection of the feedback signals for controller inputs and actuators for executing the control commands is critical for the satisfactory performance of the damping controller. The input feedback signal should maximize the observability of the oscillation mode of interest, and the actuator should be located at buses with high controllability to the mode.

With the increasing deployment of synchronized phasor measurement devices, frequency dynamics with accurate timestamps can be collected from across the power interconnections. As the power systems experience disturbances like generation tripping, load shedding, etc. excites certain oscillation modes of interest, the synchronized frequency measurements can be utilized for analysis of the observability of the mode at different locations. For frequency dynamic recordings at different locations, the Fast Fourier Transform can be applied to extract the magnitude of oscillations at various frequencies:

$$X(k) = \sum_{j=0}^{N-1} x(j)\omega_N^{jk} \quad 0 \leq k \leq N - 1$$

$$\omega_N = e^{(-2\pi i)/N}$$
(3-1)

The FFT magnitude on the candidate buses at the target mode of 0.293 Hz is shown in Table 3-1.

The frequency difference between buses 964 and 7944 showed the highest magnitude at $f = 0.293 \text{ Hz}$. However, since the PMU at bus 7944 is outside the administrative area where the control center does not have access to the real-time data, the frequency at bus 964 is chosen as the input for damping control.

Table 3-1 FFT Magnitude at the mode of interest

Bus Number	Bus Name	Event 1	Event 2
<i>f_964</i> (Palermo)	XXXXXX3802A1	7.56E-05	7.33E-05
<i>f_1568</i> (Rome)	XXXXXX3801A1	3.99E-05	3.87E-05
<i>f_3008</i> (Venice)	XXXXXX3801A1	2.39E-05	2.30E-05
<i>f_7294</i> (Milan)	XXXXXX3802A1	1.07E-05	1.03E-05
<i>f_7944</i> (Torino)	XXXXXX3801A1	5.46E-06	5.25E-06
<i>f_2590</i> (Torino)	XXXXXX3801C1	1.80E-06	1.71E-06
<i>f_2502</i> (Naples)	XXXXXX3801A1	7.12E-05	6.91E-05
<i>f_2038</i> (Florence)	XXXXXX380131	2.72E-05	2.63E-05
<i>f_964-f_7944</i>	Bus frequency difference	8.10E-05	7.85E-05
<i>f_964-f_2590</i>	Bus frequency difference	7.69E-05	7.45E-05

*Bus numbers have been altered for compliance with confidentiality requirements.

3.2.2 Choice of Control Actuators

A generalized method for selecting an appropriate actuator is through system identification and residue analysis. For each of the actuator candidates that have the potential to be deployed for oscillation damping, the transfer function between the actuator and the optimal observation point (controller input) can be constructed as in section 3.2.1. The transfer function, once identified, can always be organized in the form of:

$$G_{ij}(s) = \sum_{k=1}^n \frac{R_k}{s-\lambda_k} \quad (3-2)$$

where R_k is the residue for mode λ_k . The residue indicates how sensitive the output (frequency) is to the input (control), and it contains both the observability factor and the controllability factor:

$$R_k = c_j \phi_k \varphi_k b_k \quad (3-3)$$

where φ_k is the left eigenvector and ϕ_k is the right eigenvector associated with the oscillation mode k . The actuator with the highest residue can be selected as the optimal actuator for the damping control. For this case study, the synchronous condensers located at bus 2322 and 472 are chosen as the actuator.

3.2.3 Design of the Wide-Area Damping Controller Parameters

While a variety of actuators can be utilized in the damping control, synchronous generators/condensers are used in the TERN study due to resource availability. Figure 3-2 shows the structure of the closed loop that contains the WADC, the actuator, and the rest of the power system.

With the observation signal (Δf) selected as in section 3.2.1 and the actuator at bus 2322, the WADC parameters can be designed once the system between V_{ref} and Δf can

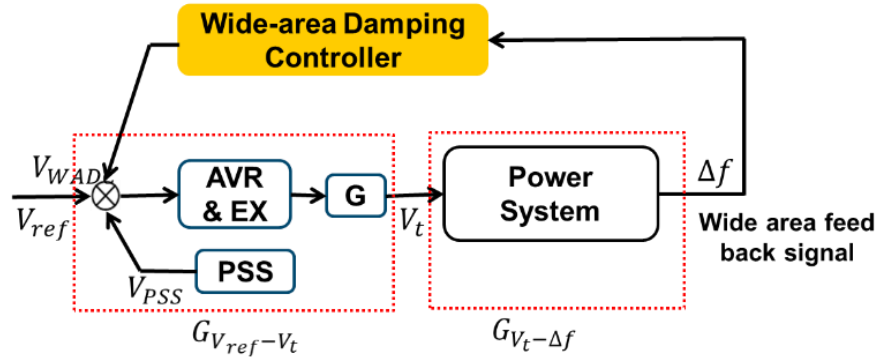


Figure 3-2 Structure of the closed-loop system with the WADC [6], [47]

be identified. $G_{V_{ref}-\Delta f}$ can be treated as a multiplication of two transfer functions, $G_{V_{ref}-V_t}$ and $G_{V_t-\Delta f}$. The first transfer function, $G_{V_{ref}-V_t}$, reflects the physical characteristics of the generators and can be identified by injecting probing signals (low-pass filtered white noise is used in this study).

$$G_{V_{ref}-V_t,2322} = \frac{2.64s^4 + 90.41s^3 + 2851s^2 + 1868s + 37519}{s^5 + 4.082s^4 + 1004s^3 + 2974s^2 + 13707s + 36518} \quad (3-4)$$

The second transfer function, $G_{V_t-\Delta f}$, reflects the rest of the power system and can be identified by injecting probing signals (low-pass filtered white noise is used in this study):

$$G_{V_t-\Delta f,2322} = \frac{0.5772s^3 + 99.54s^2 + 266.7s + 250}{s^4 + 9.822s^3 + 1017s^2 + 1134s + 1100} \quad (3-5)$$

The WADC is designed to modulate the magnitude and compensate the angle so that the damping ratio of the target mode is maximized. The characteristic equation of the control loop shown in Figure 3-2 is as follows:

$$1 + G_{WADC}(s)G_{V_t-\Delta f}(s)G_{V_{ref}-V_t}(s) = 0 \quad (3-6)$$

where $G_{WADC}(s)$ represents the transfer function of the controller, of which the structure is shown in Figure 3-3.

Thus, the transfer function of the WADC (excluding the filter)

$$G_{WADC}(s) = K_w \frac{T_w s}{1 + T_w s} \left(\frac{1 + T_1 s}{1 + T_2 s} \right)^2 \quad (3-7)$$

Let $s = j\omega_d$ and solving the characteristic equation (3-6) gives:

$$\begin{aligned} \arg(G_{WADC}(j\omega_d)) + \arg(G_{V_t-\Delta f}(j\omega_d)) + \arg(G_{V_{ref}-V_t}(j\omega_d)) &= 180^\circ \\ |G_{WADC}(j\omega_d)| |G_{V_{ref}-V_t}(j\omega_d)| |G_{V_t-\Delta f}(j\omega_d)| &= 1 \end{aligned} \quad (3-8)$$

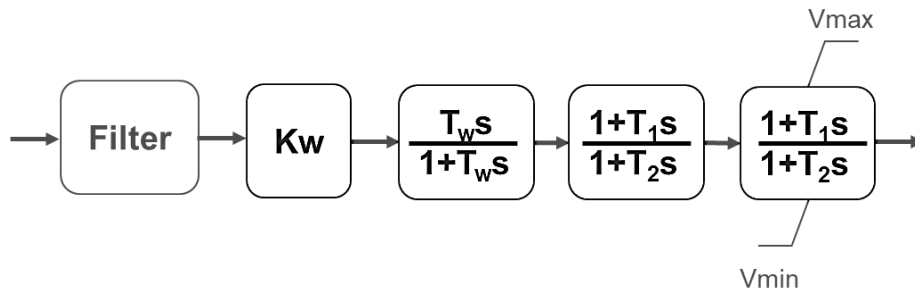


Figure 3-3 Transfer function block diagram of the WADC

The parameters can be obtained as:

$$\begin{cases} T_1 = \alpha T_2 = 0.5451 \\ T_2 = \frac{1}{\sqrt{\alpha}\omega_d} = 0.5451 \\ K_w = \frac{|G_{WADC}(j\omega_d)|}{\left(\frac{1+T_1j\omega_d}{1+T_2j\omega_d}\right)^2} = 964 \end{cases} \quad (3-9)$$

The WADC has been implemented on the National Instruments' generic hardware controller platform, CompactRIO, for prototyping and testing. In the next section, details about the implementation of the controller and the hardware-in-the-loop (HIL) testing platform will be introduced and testing results will be discussed.

3.3 Hardware Implementation of the WADC and the HIL Platform

3.3.1 Overview of the Hardware-in-the-Loop (HIL) Platform

Compared with computer simulations, the HIL setup emulates a real-time operating environment to verify the performance of the developed WADC under more realistic scenarios, including measurement error/noise, varying time delay, and data package loss. The framework of the built HIL test setup is shown in Figure 3-4. The Continental Europe Synchronous Area system model was emulated on the OPAL-RT's real-time digital simulator OP5600 [75]. Based on the phasor domain simulation results, e.g., voltage magnitude, phase angle, and frequency, the real-time digital simulator generates the associated analog voltage waveforms. An amplifier was used to step up the voltage from +/- 10V to +/-120V to emulate the secondary side of a potential transformer and feed the analog voltage signal to PMU devices. The WADC implemented with National Instrument's CompactRIO receives the PMU streaming measurements complying with the standard IEEE C37.118. A communication network impairment simulator is used to introduce signal latency and data package loss to test the controller performance in the non-

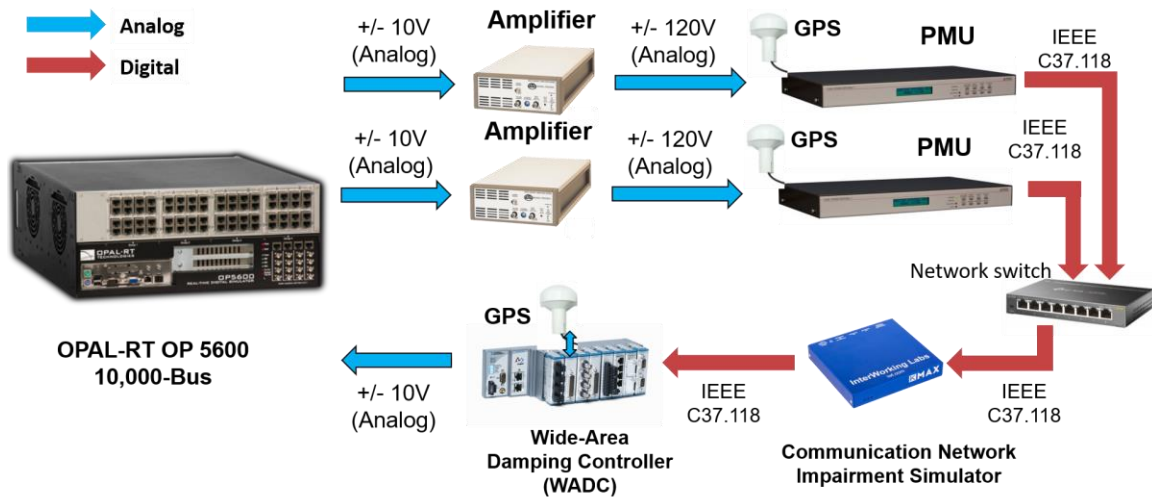


Figure 3-4 The HIL testing platform for the WADC.

ideal communication environment. The WADC generates the control command, converts it into a +/- 10V analog signal, and feeds it to the real-time digital simulator.

3.3.2 Hardware Implementation of the Controller

The overall structure of the WADC is described in Figure 3-5. The controller has the following function modules: PMU data receiver, GPS module, delay detector, lead-lag structure, supervisory control, delay compensator, missing data handling, oscillation detector, and D/A conversion.

A graphical user interface has been developed for the damping controller, as shown in Figure 3-6. It provides the users with an intuitive presentation of controller operation status and a convenient interface for human intervention.

The interface displays a scope window for frequency in Palermo and two windows for the control outputs. On the bottom left, there are two buttons to enable/disable the controllers. Next to the enabling section is the supervisory control display. It shows the on/off status, communication delay, and in-use information for both PMU channels. The red square light "PMU Alert" only comes on when both PMU channels fail the data quality requirements for maintaining the correct operation of the controller. Also in place is the delay compensation section, which gives information about the delay of the package being used for control at the moment, and the corresponding parameter set used for compensation. The "FPGA Locked" is an indicator of the successful synchronization of the controller through its GPS extension module. A breakdown of the function blocks in the controller is as follows.

- The PMU data receiver is a function block that communicates with PMUs or PDCs through the phasor measurement communication protocol IEEE C37.118-2011. It

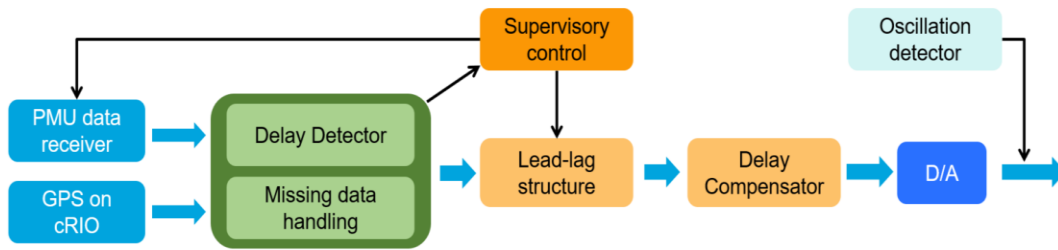


Figure 3-5 Overall structure of the controller

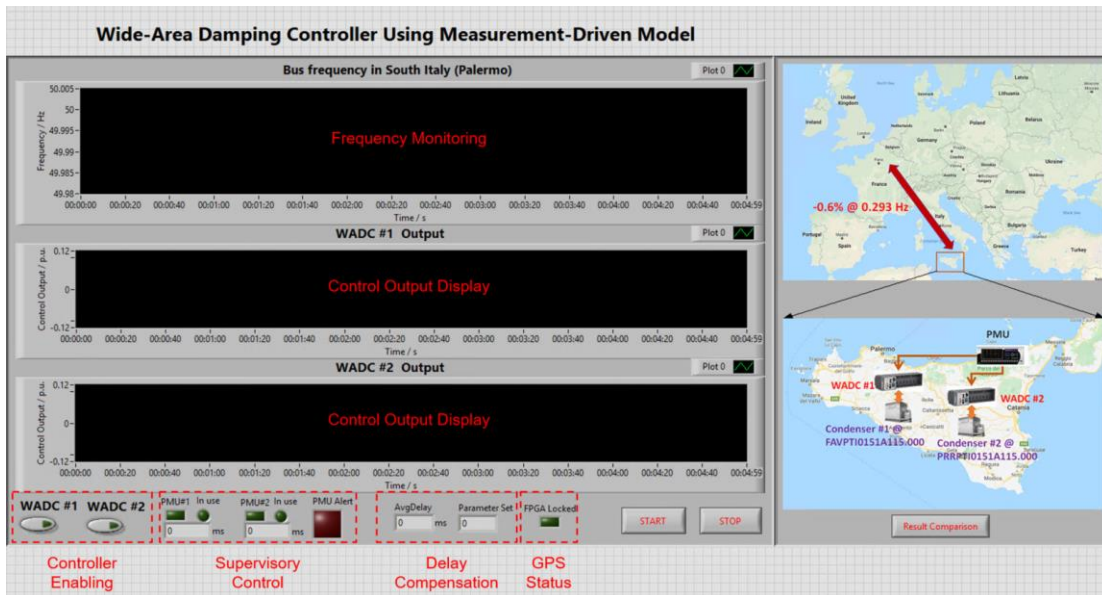


Figure 3-6 The graphical user interface of the damping controller

supports both TCP/IP and UDP/IP, but UDP/IP is recommended for the control purpose since the controller can tolerate occasional data loss, while requires timely updates from measurement devices.

- The GPS module is used to receive the GPS signal to capture an absolute timestamp.
- The delay detector (Figure 3-7) measures the actual delay from the moment the measurement was taken to the moment the controller uses it. The function shares the assessed delay with the supervisory control and the delay compensator block for further processing and control.
- The missing data handling module manages and copes with data loss caused by data drops (permanent loss) or congestion (temporary loss) in the communication network.
- The supervisory control module continually monitors the communication delay in all PMU channels and decides which channels to be adopted for control. Whenever the primary (default) PMU channel sees the communication delay being consistently larger than 1 second, the supervisory control will attempt to switch to the backup PMU channel to reduce the impact. When the primary PMU channel comes back to normal operation, the controller will wait for a few seconds to ensure the reliability of it and then switch back.
- A section of the GUI is allocated for supervisory control as shown in Figure 3-8. It presents to the operator the real-time delays in all the PMU channels, and the PMU currently in use. If both PMU channels experience severe issues that may compromise the safe operation of the controller, the supervisory control (Figure 3-9) will give a "PMU Alert" light as a warning and pause the control output until at least one PMU channel comes back.

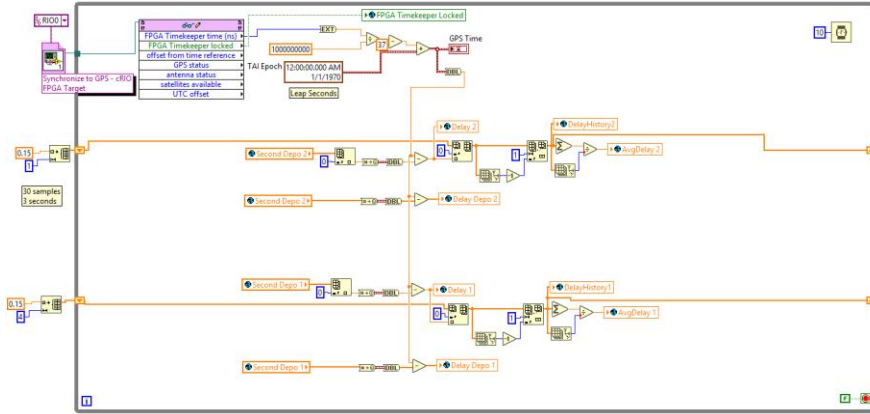


Figure 3-7 Implementation of the delay detector on CompactRIO

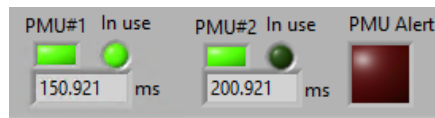


Figure 3-8 Supervisory control on the GUI

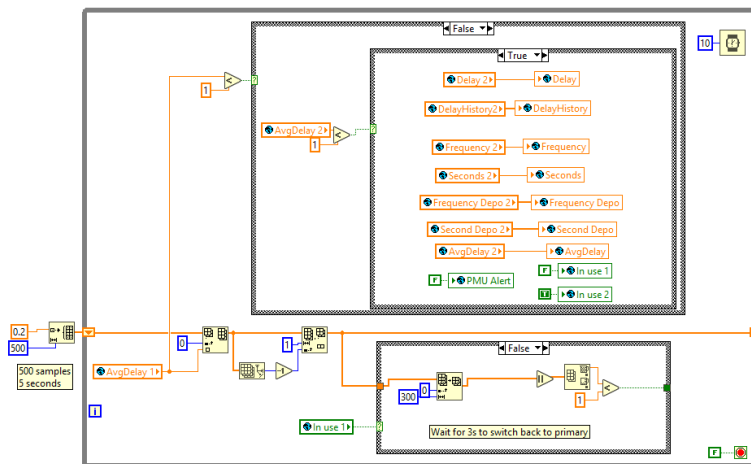


Figure 3-9 Implementation of the supervisory control function

- The lead-lag structure block is an implementation of the transfer function in the WADC for compensating the angle shifts.
- The delay compensator monitors (Figure 3-10) the actual delay of the package being used and chooses the best set of compensation parameters for it. It can also buffer the data received and actively use packages around a specific delay value to reduce switching between compensation parameter sets.
- The oscillation detector module monitors the oscillation in the system and decides when to activate or deactivate the damping controller. The decision is made based on the oscillation magnitude in a moving window. The detector enables the control when the maximum oscillation magnitude during that period is larger than a threshold and disables it when the maximum is smaller than the threshold. Both the magnitude threshold and the length of the time window are reconfigurable in the module.
- The D/A module converts the digital signal to analog control output, which is fed back into the OPAL-RT simulator. In the HIL setup, the actuator in the model takes an analog signal through the input breakout board of OPAL-RT. Hence, the controller needs a digital-to-analog conversion module to convert the digital control command to an analog voltage signal before it is fed to the OPAL-RT. The D/A extension board installed on the CompactRIO is NI-9263 [76], which has four channels of analog voltage output with a sampling rate of 100 kS/s.

3.3.3 Real-Time Simulation of the Continental Europe Synchronous Area

While the OPAL-RT ePHASORSIM model solver is able to utilize the PSS/e power flow and dynamic model files for real-time simulation, several user-defined PSS/e dynamic models are still required due to the limited built-in PSS/e model library in OPAL-RT.

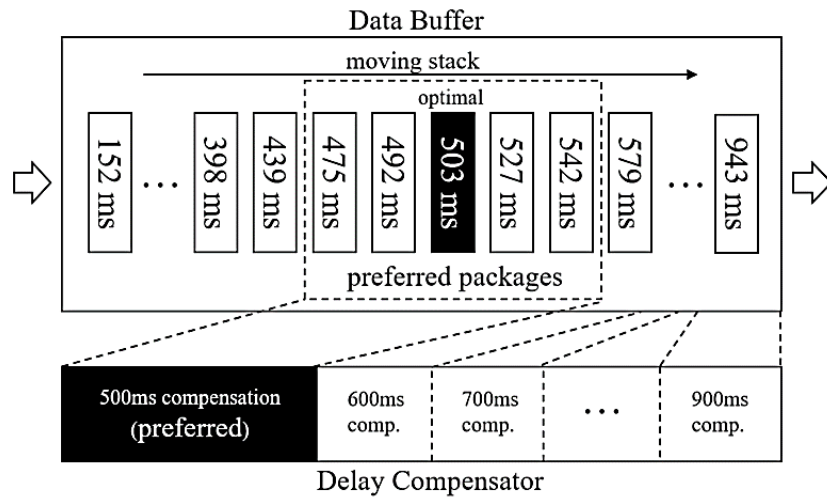


Figure 3-10 Structure of the delay compensator

Figure 3-11 shows the files necessary for transitioning the PSS/e models to the real-time simulator, OPAL-RT ePHASORSIM.

To generate the user-defined dynamic models that are supported by the ePHASORSIM model solver, auxiliary files were added to support the model simulation. The auxiliary files include Functional Mock-up Units (FMUs), FMU glossary files, and PSS/e mapping files. An FMU is a user-defined generator unit model compiled on the OpenModelica platform, which contains components such as generators, exciters, governors, and power system stabilizers (PSSs). The FMU glossary file lists all the parameters involved in the components, and the PSS/e mapping file provides the mapping between the parameters in FMUs and those in PSS/e models.

These FMUs were constructed by using the basic PSS/e component model library in OpenModelica provided by OPAL-RT. A typical layout of a generation unit is shown in Figure 3-12. Blocks GENSAL, SEX, IEE2ST, and TGOV1 are base components of the generator, exciter, stabilizer, and governor. The green and red triangles are input and output pins that interface with the OPAL-RT ePHASORSIM model solver. The OpenModelica compiles the FMUs for both the Linux and Windows platforms so that the FMUs can be called upon in both real-time and offline simulations.

To ensure the constructed ePHASORSIM model can reflect the Terna system dynamic properties accurately, power flow and dynamic simulation results of the Terna system model from OPAL-RT and PSS/e were compared.

The power flow solutions in PSS/e and ePHASORSIM model are compared in Table 3-2, which includes the buses with maximum voltage magnitude and angle mismatches, as

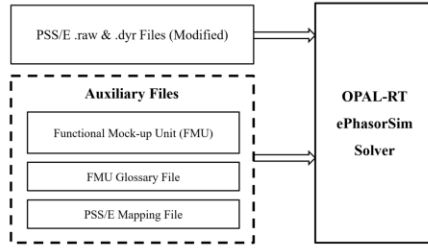


Figure 3-11 Input files to the OPAL-RT real-time digital simulator

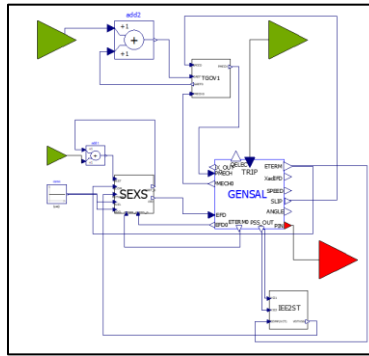


Figure 3-12 Structure of a sample generation set in OpenModelica

Table 3-2 Comparison of power flow solutions in OPAL-RT and PSS/e

Bus Number	Base Voltage (kV)	Voltage Magnitude/Angle (p.u./deg.)		Mag./Ang. Difference (p.u.)
		OPAL-RT	PSS/E	
85	400	0.9497 / 117.31	0.9507 / 117.43	0.0010 / 0.12
286	400	0.8860 / 124.34	0.8870 / 124.39	0.0010 / 0.04
3829	400	0.9091 / 101.44	0.9095 / 101.62	0.0004 / 0.18
6568	400	0.9886 / 124.50	0.9898 / 123.08	0.0012 / 1.41
3538	400	1.0142 / 156.07	1.0157 / 151.88	0.0015 / 4.19
947	220	1.0858 / 148.61	1.0899 / 147.14	0.0041 / 1.47
3498	220	1.0258 / 104.23	1.0245 / 104.06	0.0013 / 0.16
2034	220	1.0127 / 96.69	1.0070 / 97.13	0.0057 / 0.43
9387	220	0.8651 / 94.60	0.8650 / 94.83	0.0001 / 0.23

*Bus numbers are altered for compliance with confidentiality requirements

well as a few other sample buses. The maximum voltage magnitude mismatch is 0.0057 p.u., while the maximum angle difference is 4.19 degrees. Therefore, the power flow solutions in PSS/e and ePHASORSIM model match with acceptable accuracy.

The events used for model validation are two consecutive trips of generators, representing the 2017 event at the Italian grid. The first generator trip occurs at $t = 5$ s at Bus 7400, and the second at $t = 245$ s at Bus 7398. The frequency at Bus 7678 and the active power on the tie-line between Bus 4156 and Bus 992 during the events are shown in Figure 3-13 and Figure 3-14, respectively, where the amber curve represents the simulation result from OPAL-RT and the blue curve from PSS/e.

The simulation results of both the selected bus frequency and tie-line power are consistent across the two platforms. With Prony analysis, the dominant mode in OPAL-RT was at 0.294 Hz with a damping ratio of -0.614%, and that in PSS/e was at 0.294 Hz with a damping ratio of -0.616%. The comparison of oscillation frequency and damping ratio are given in Table 3-3. The TERNA power grid model has been implemented successfully on OPAL-RT ePHASORSIM without compromising the accuracy of the dominant oscillation mode of interest.

3.4 Hardware-in-the-Loop Testing Results

With the HIL testing platform introduced above, the controller has been tested for various situations and purposes, as shown in Table 3-4. The controller demonstrated its capability of handling time delays, data drops, and chunk data loss. The rest of this chapter presents the results and findings from these test cases.

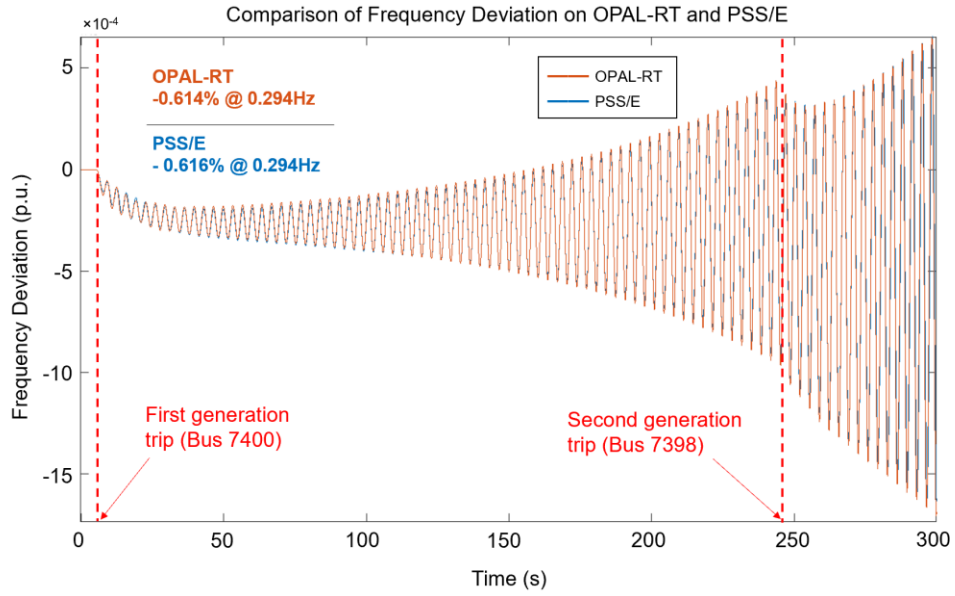


Figure 3-13 Comparison of frequency deviation in OPAL-RT and PSS/e

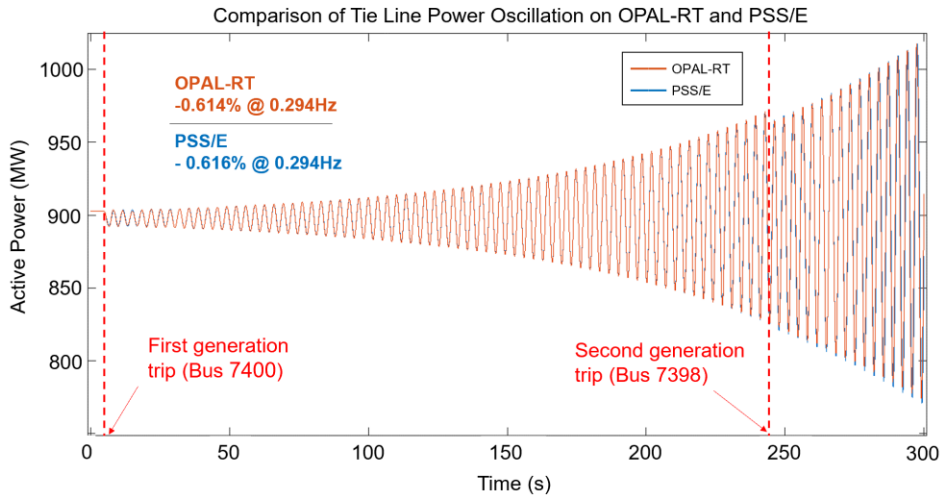


Figure 3-14 Comparison of tie-line power oscillations in OPAL-RT and PSS/e

Table 3-3 Comparison of oscillation frequency and damping ratio

Data window	PSS/e		OPAL-RT		PMU measurements	
	Freq. (Hz)	Damp. (%)	Freq. (Hz)	Damp. (%)	Freq. (Hz)	Damp. (%)
[5, 45 seconds] after first trip	0.293	-0.410	0.293	-0.410	0.293	-1.062
[250, 290 seconds] after second trip	0.292	-0.628	0.292	-0.628	0.292	-0.614

Table 3-4 Testing cases conducted on the HIL platform

Case #	Case Name	Note
1	Base case	No delay, no data drop
2	Constant time delay	300ms, 500ms, 800ms
3	Random time delay	--
4	Random data drops	--
5	Chunk data loss and supervisory control	--
6	Comparison of TCP and UDP	--

3.4.1 Case 1: Base Case

The base testing case is intended to demonstrate the basic performance of the damping controller under no additional communication network impairments. In the base case, the comparison is between the system with and without the WADC, under the two consecutive events that happened on December 3rd, 2017. The result is shown in Figure 3-15, and the damping ratios in Table 3-5 are calculated through Prony analysis.

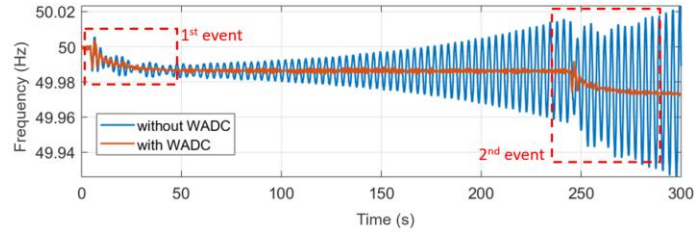
Without the WADC, the oscillation grew, with damping ratios of -0.486% and -0.449% after the two events, respectively. When the WADC is enabled, the damping ratio increased to 12.326% and 12.051% during the two events, and the oscillations settled within 10 seconds. The WADC significantly improved the system damping and hence enhanced the stability as a result.

3.4.2 Case 2: Constant Time Delay

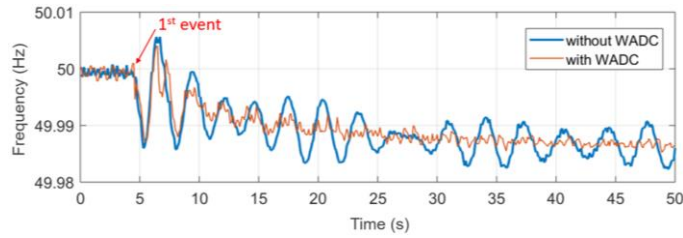
To test the controller with a constant time delay, the network simulator was set to introduce the same delay to every package that goes through it before arriving at the controller. Since the communication loop has an inherent minimum delay of around 150ms, the total delay will be 150ms plus the time delay introduced by the network simulator. Test results under the generation trip events with an additional delay of 300ms, 500ms, and 850ms are shown below.

In the 300ms delay test (Figure 3-16), the system still has a positive damping ratio and the oscillation settled after around 70 seconds. The performance during the transient deteriorated compared to the no-delay case and the compensated case.

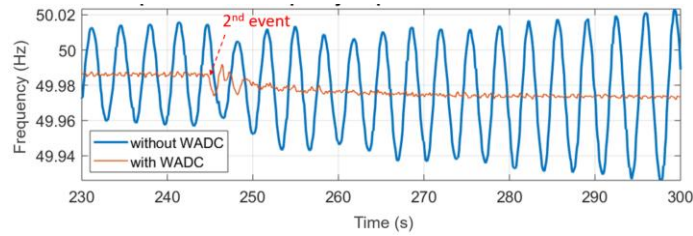
For delays over 500ms (Figure 3-17, Figure 3-18), the system experiences growing oscillations when no compensation is engaged. The benefit of applying the compensation



(a) Overview of the two consecutive events



(b) Details around the first event



(c) Details around the second event

Figure 3-15 Frequency dynamics in the base case testing

Table 3-5 Comparison of damping ratios before and after the application of WADC

Controller Presence	Damping Ratio (%)	
	<i>1st event</i>	<i>2nd event</i>
Without WADC	-0.486	-0.449
With WADC	12.326	12.051

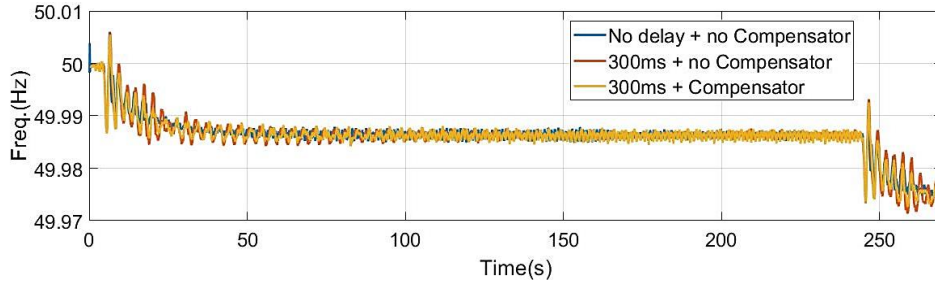


Figure 3-16 Frequency response under 300ms additional communication delay

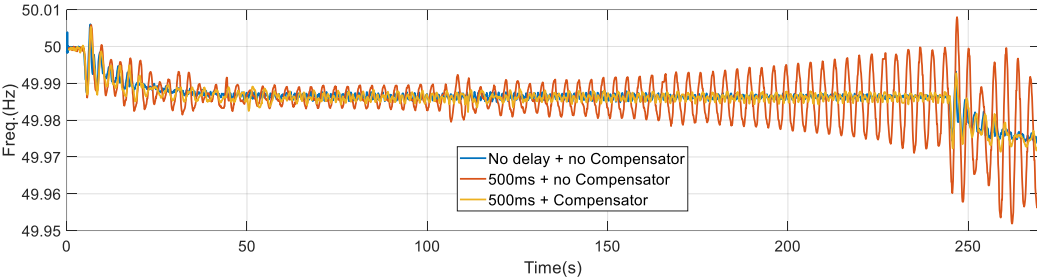


Figure 3-17 Frequency response under 500ms additional communication delay

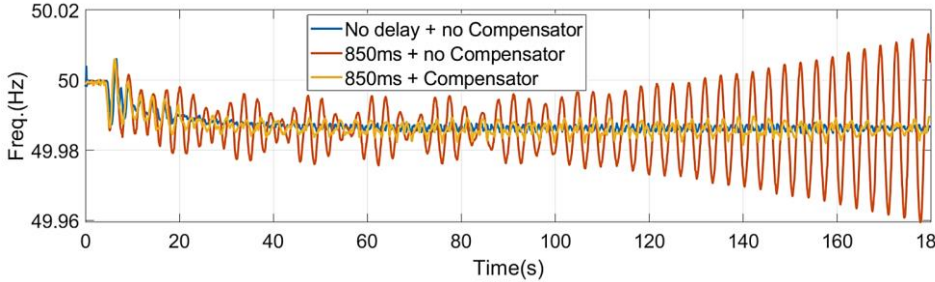


Figure 3-18 Frequency response under 850ms additional communication delay

was evident in this case. However, in the 850ms constant delay case, deterioration in the steady state is noticed after the oscillation is settled. This provides a useful reference for how much of a delay should be considered tolerable and be compensated without engaging supervisory control for alternate PMU channels.

3.4.3 Case 3: Random Time Delay

To validate the capability of the controller in handling random delays, the network simulator was set to introduce random delays to all the packages conforming to the gaussian distribution, which means most of the packages will have a delay close to the mean value of the Gaussian distribution.

The two generator trip events are still used in this test. For the period after the first generator trip and before the second one, the random delay was set to have a gaussian distribution with a mean of 50ms and a standard deviation of 50ms. For the period after the second trip event, the mean was changed to 700ms, and the standard deviation stays 50ms. The tests were conducted for both the adaptive and fixed compensation methods to demonstrate the effectiveness and impact of the automatic parameter selection in the delay compensation block. The results are shown in Figure 3-19.

During the first event, the small amount of random delay ($\mu = 50ms$, $\sigma = 50ms$) did not have a large impact on control performance. Both the adaptive and fixed delay compensation gave a similar control effect. During the second event, the random delay was reconfigured to $\mu = 700ms$, $\sigma = 50ms$. The adaptive delay compensation demonstrated its effectiveness by automatically switching to the optimal compensation parameter set.

Another test has been done to compare the compensation with and without the data buffer, as described in section 3.3.2. The target buffer age was set to 500ms, which

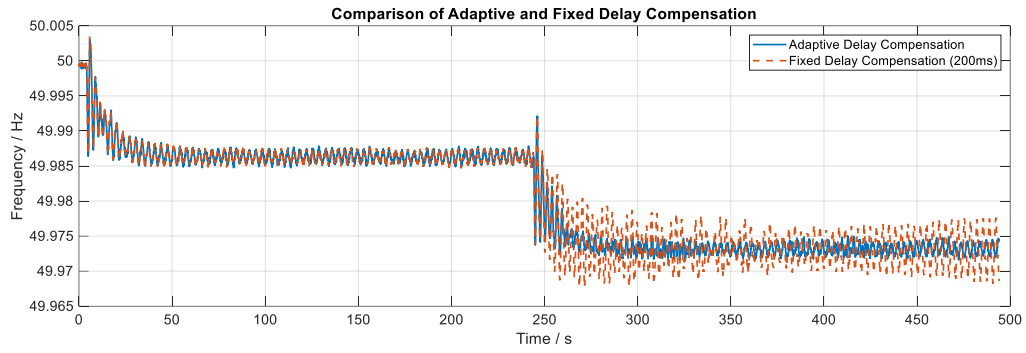


Figure 3-19 Frequency response of the system under random delays

indicates the controller will attempt to choose appropriate packages in the buffer to keep the delay of the packages used for control as close to 500ms as possible. The test result is shown in Figure 3-20.

From the top plot in Figure 3-20, the control effect of the buffered and unbuffered approaches are similar. However, the difference in the pattern of delay and parameter set selection is evident. In the middle figure, the delay of packages used for control in the unbuffered case (amber curve) was constantly varying between 300ms to 600ms, while that in the buffered case (blue curve) was almost constant at 500ms. This effectively lessens the switching between different parameter sets, which is well demonstrated in the bottom figure.

3.4.4 Case 4: Random Data Drop

Since the data drop, in reality, happens along with delay, a random data drop has been introduced on top of random delay by the network simulator. The test result is shown in Figure 3-21. The controller operated reliably under a data drop rate as high as 60%. This is because the UDP is very tolerant of data drops due to its nature, by which it neglects the lost package and moves forward for the later ones. Details will be given in the section that discusses the comparison of TCP and UDP.

3.4.5 Case 5: Chunk Data Loss and Supervisory Control

The supervisory control constantly monitors the PMU channels for abnormal situations. Chunk data loss is a typical example where the controller receives no updates from the PMU channel for a longer period of time than random data drops. This test applies a chunk data loss that persists for 10 seconds starting at $t = 5s$ to verify the operation of the supervisory control module.

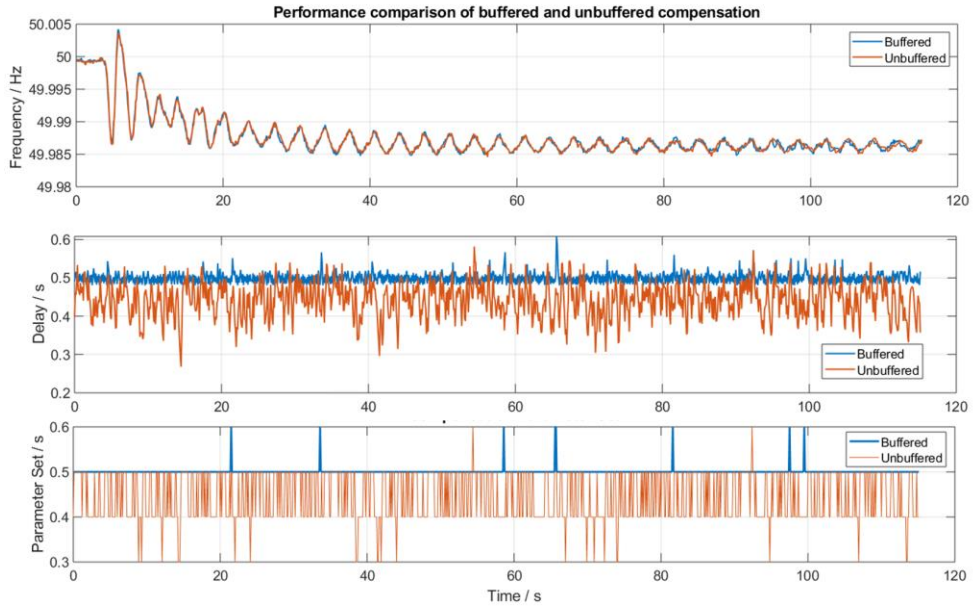


Figure 3-20 Comparison of the buffered and unbuffered compensation

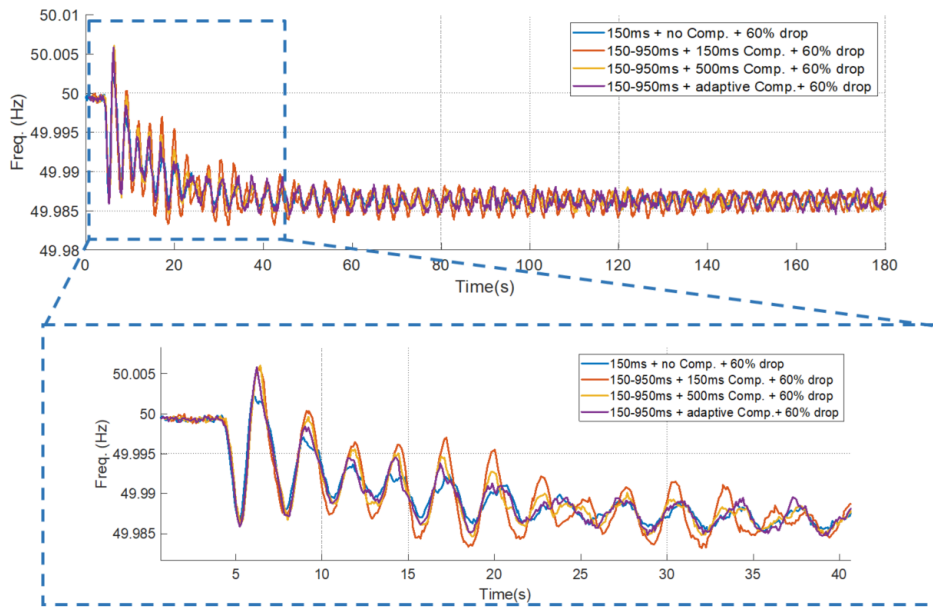


Figure 3-21 Control performance under 60% random data drop

As labeled in Figure 3-22, the chunk data loss started in the primary PMU channel at $t = 5$, and the controller saw a rapid increase in the delay since no new measurements are arriving. The supervisory control took action to switch to the backup PMU channel after three seconds (this time window is reconfigurable) of confirmation. Three seconds after the primary PMU came back normal, the supervisory control switched back to the primary.

Figure 3-23 shows the controller output under chunk data loss, with and without the supervisory control enabled. It is noticed that without the supervisory control (the amber curve), the controller stopped outputting control commands to ensure do-no-harm during the chunk data loss. However, in the with-supervisory-control case (the blue curve), the controller kept operating with the measurements streaming in from the backup PMU. The supervisory control module demonstrated its capability of monitoring and dispatching the PMU channels to ensure the continuous operation of the controller in abnormal situations.

3.4.6 Case 6: Comparison of TCP and UDP

In order to compare the impact of communication protocols on the controller, a few test cases are presented in this section, including random delay and random data drops.

3.4.6.1 Random Time Delay

Three test cases are for the investigation of the impact of random delay:

- Base case – intrinsic delay only ($\sim 160\text{ms}$)
- With additional random delay in gaussian distribution - $\mu = 300\text{ms}$, $\sigma = 100\text{ms}$
- With additional random delay in gaussian distribution - $\mu = 600\text{ms}$, $\sigma = 100\text{ms}$

The actual delay perceived at the controller is depicted in Figure 3-24. For the base case (without additional delay), the TCP and UDP saw the same delay at around 160ms, which is the intrinsic delay in the HIL loop. In the 300ms and 600ms delay cases, the TCP (solid

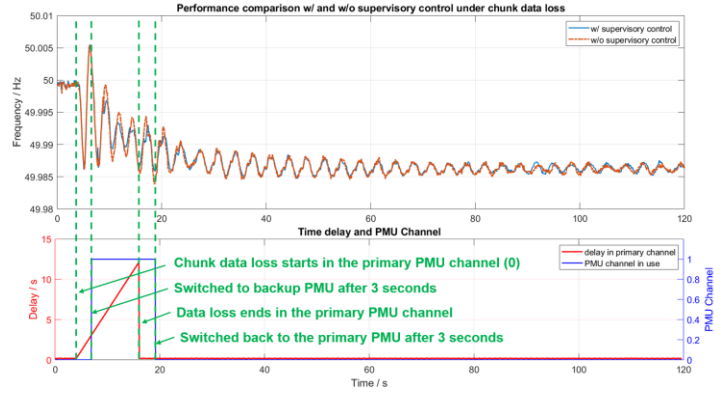


Figure 3-22 Control performance with supervisory control

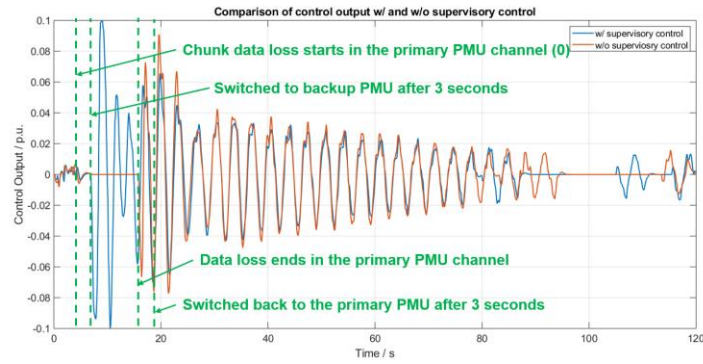


Figure 3-23 Control output with supervisory control

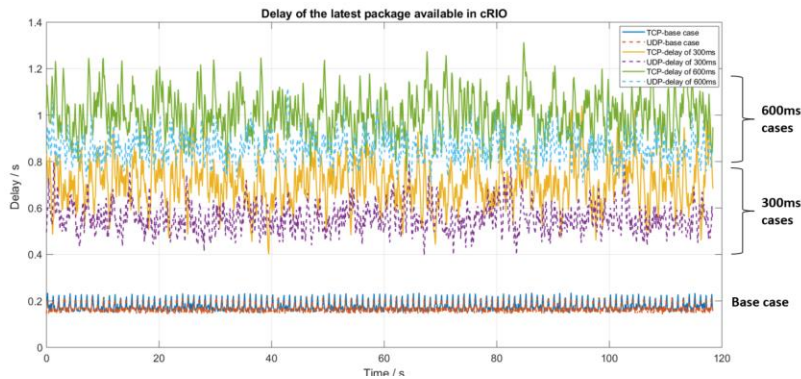


Figure 3-24 Actual delay measured by the controller

lines) sees consistently higher delays than the UDP (dash lines). However, this didn't result in deterioration in the control performance (in Figure 3-25) as the delays in TCP cases are still relatively stable, so the delay compensator block automatically adapted and chose an optimal set of compensation parameters.

3.4.6.2 Random Data Drops

In the random data drop tests, the 5% and 10% drop rates have been put in place for both TCP and UDP. The top figure in Figure 3-26 shows the comparison of actual delays observed by the controller with TCP and UDP.

It is noticeable that the delay was steadily 160ms for UDP, while it varied drastically with TCP, topping 4 seconds maximum. This is due to the design of TCP, which prioritizes successful delivery of every package over time delay. Whenever a package is dropped, TCP will use additional communication among the PMU and controller to resend the package. Because of the risks of losing these additional packages on top of the original loss, the actual delay seen by the controller can jump to an unacceptable level. Such deterioration was also reflected in the control performance shown in Figure 3-27. The decline in performance becomes even more drastic in the 10% drop rate case.

In the 10% drop rate test, the actual delay measured by the controller when running TCP (Figure 3-28) jumped to 30 seconds maximum (blue curve in the top figure), and the controller stopped outputting control commands as shown by the blue curves in the bottom figure. However, the UDP managed to keep the actual delay at 160ms – 200ms, and the controller was operating normally (red curve in the bottom figure) despite the data drops. This is because the UDP prioritizes the timely delivery of the latest packages and moves on if previous packages are lost, which aligns with the need for the damping controller.

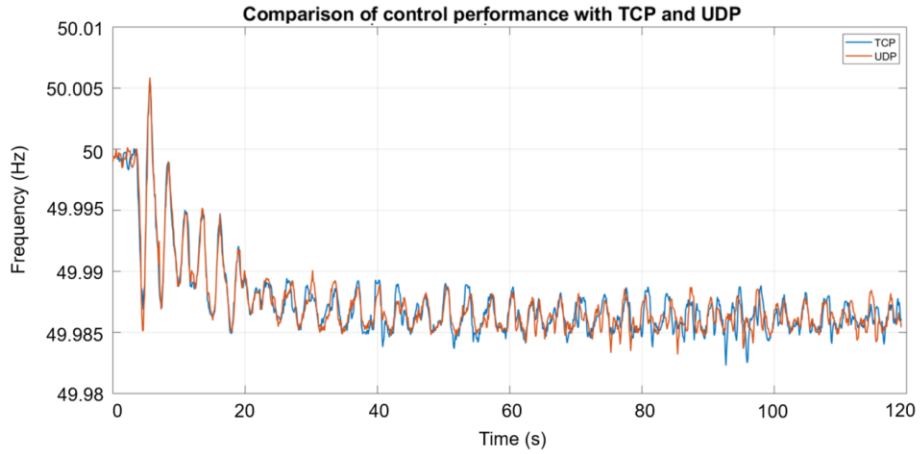


Figure 3-25 Control performance with TCP and UDP with random delay

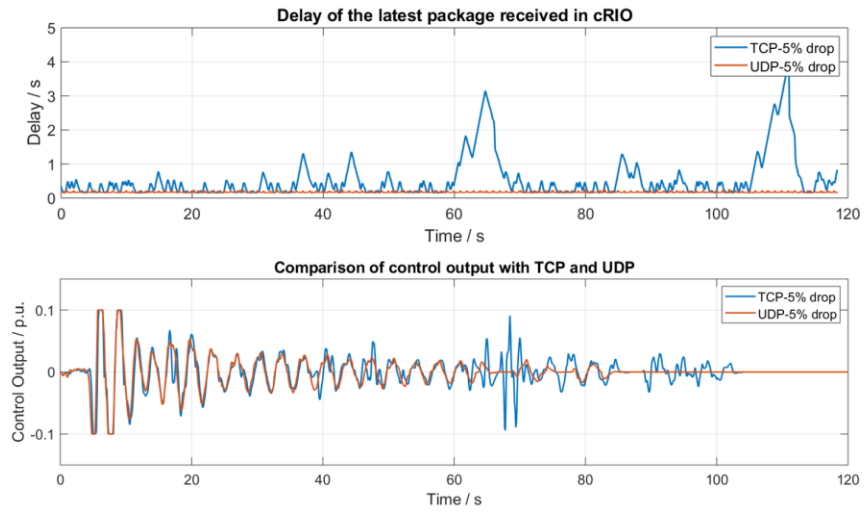


Figure 3-26 Actual delay and control output under 5% data drop

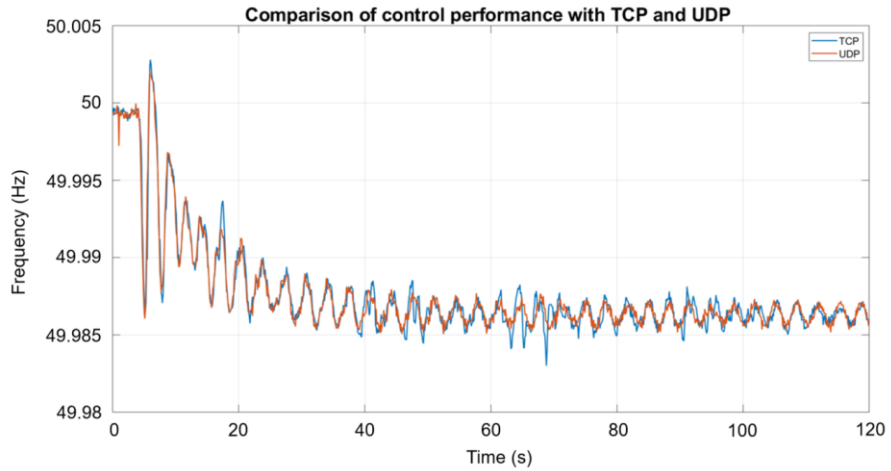


Figure 3-27 Control performance with TCP and UDP under 5% data drop

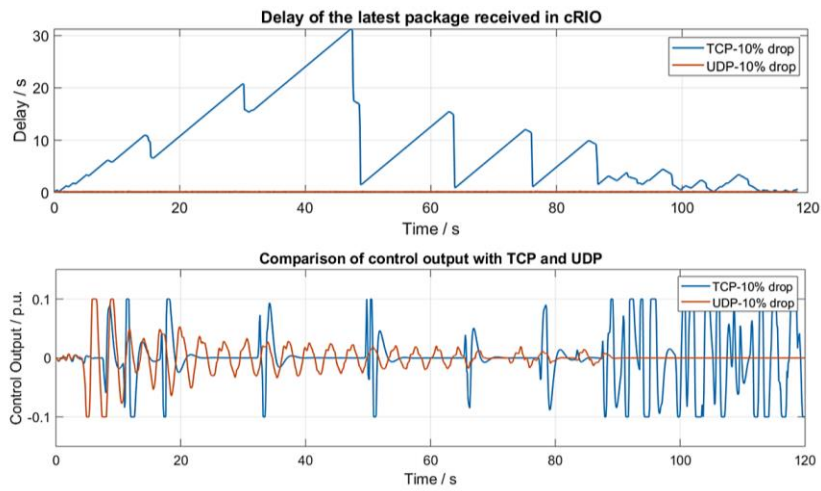


Figure 3-28 Actual measured delay and control output under 10% data drop

3.5 Summary

With the increasing renewable integration and declining inertia level, the Continental Europe Synchronous Area power interconnection has been faced with more frequent inter-area oscillations, especially during light-load high-renewable periods. The increasing deployment of synchronized phasor measurement devices and communication facilities opens the possibility for wide-area damping control schemes to improve the damping of interarea oscillations. This chapter presented a comprehensive method for measurement-based wide-area oscillation damping, including the selection of optimal observation points, the choice of optimal actuator locations, and the design of controller parameters. The controller has been implemented on hardware and a hardware-in-the-loop testing platform is constructed for testing the performance of the controller under realistic environments. The 2067-bus Continental Europe Synchronous Area model is implemented on the real-time simulator. Comprehensive testing scenarios derived from real-world consecutive generator trips and incorporating various network uncertainties have been conducted. The controller improved the damping ratio of the target mode from negative to 12% in the base test case. A variety of communication uncertainties including delays, data drops, and channel loss are simulated through a network impairment simulator in the HIL. The controller maintained its performance by handling the uncertainties with its adaptive delay compensator and supervisory control modules. The performance of the WADC under TCP/IP and UDP/IP is also compared and recommendations are made for future deployment in the field.

CHAPTER 4. MEASUREMENT-BASED VOLTAGE AND FREQUENCY CONTROL WITH IBRS

4.1 Introduction

With the increasing integration of IBRs, power systems are facing challenges from deteriorating frequency and voltage response characteristics. For example, the reducing and uneven distribution of inertia brings challenges to regional dynamics, and the volatility in the operation conditions, load forecast, and RES generation forecast pose threats to the effective formulation and optimization of voltage control schemes.

However, these inverter-based resources have the actual potential to be valuable assets in frequency and voltage regulation by providing fast active and reactive power controls once a robust, reliable frequency/voltage regulation mechanism is designed and implemented. This requires enhanced measurement feedback for the controllers to have increased visibility of the system and reduced reliance on model parameters. The frequency and voltage control schemes designed for NY State Grid in this chapter aim at leveraging synchronous measurement for fast, frequency/voltage recovery, which at the same time, flexibly coordinates control areas and various resources.

It should be noted that part of the content in this chapter is from the author's paper submitted to the 2023 IEEE PES General Meeting [77]. Also, sensitive information such as bus numbers is altered in compliance with confidentiality requirements.

4.1.1 Hierarchical-Local Frequency Control

Traditional frequency control in a power system consists of mainly three stages: the inertial response, primary frequency response, secondary frequency response, and tertiary

frequency response [26]. The inertial response and primary frequency response are posed to decline with the increasing renewable integration. In addition, the changes in these frequency response sources are not even across the interconnection as a result of the uneven deployment of renewables [78]. Traditional secondary frequency regulations through the automatic generation control system are based on coordination between generation resources' frequency response characteristics, which is executed by adjusting frequency-responsive generators' droop curve setpoints. However, the coordination is on the time scale of tens of seconds to ten minutes, and it requires delicate tuning of the automatic generation control system to achieve satisfactory transient and steady-state performance.

With the increasing availability of inverter-based resources, fast frequency control schemes have been utilized for providing fast responses to disturbances [79-81]. A majority of the fast response methods are open-loop control that is triggered by either frequency deviation or rate-of-change-of-frequency thresholds. Once the thresholds are violated, the inverter-based actuators quickly inject a certain amount of active power to stabilize the frequency dynamics. While the open-loop control avoids stability issues, it is usually not able to accurately compensate for the power imbalance and leads to over- or under-compensation.

Other methods include the wide-area-measurement-based, centralized control that takes advantage of the increasing deployment of PMUs [82]. These methods adjust the power output of participating resources based on the feedback from the synchronized measurements. However, despite the feedback measurements from various regions across the grid, the solution did not consider the uneven distribution of inertia and inverter-based resources and requires observability across the grid.

In an effort to address the increasing volatility in the load and generation, as well as the uneven distribution of inertia and inverter-based resources, reference [7] proposed a hierarchical-local fast frequency control scheme that incorporates the inverter-based resources and prioritizes local compensations, of which the overall structure is shown in Figure 4-1.

The scheme is composed of two levels to realize a local-global fast frequency control. On the local level, each local control area is assigned a local controller. The local controller takes measurements from their regions through local communications, including power measurements on tie-lines encompassing the area and active power outputs of the IBRs within the area. The disturbance size can be estimated as in (4-1):

$$\mathbf{P}_d = \mathbf{P}_e - \Delta\mathbf{P}_{tie} + \Delta\mathbf{P}_{IBR} - \Delta\mathbf{P}_{load} \quad (4-1)$$

where \mathbf{P}_d is the disturbance size to be estimated, \mathbf{P}_e is the total active power deviation in all synchronous generators, $\Delta\mathbf{P}_{tie}$ is the total tie-line power deviation, $\Delta\mathbf{P}_{IBR}$ is the total IBR power deviation, and $\Delta\mathbf{P}_{load}$ is the total load power deviation due to frequency deviations. In a large-scale interconnection like EI, the frequency deviation caused by events is small (1000MW leads to ~0.0006 p.u. of frequency deviation). Hence, the change in loads and generator output in the small region (especially in the first few seconds) can be negligible for the purpose of fast frequency recovery.

Hence, equation (4-1) can be simplified as in (4-2) to reduce measurements needed on generators and loads.

$$\mathbf{P}_d = -\Delta\mathbf{P}_{tie} + \Delta\mathbf{P}_{IBR} \quad (4-2)$$

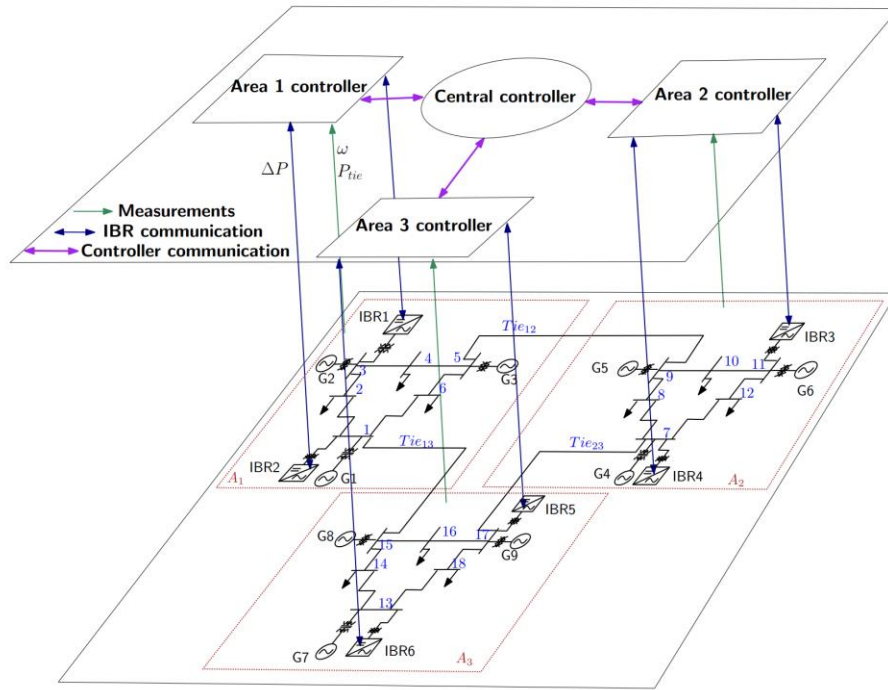


Figure 4-1 Structure of the hierarchical-local frequency control [7]

The amount of active power imbalance caused by the disturbance is then distributed to the available inverter-based resources according to their available headroom.

For small disturbances, the local mobilization of the resources might be enough to compensate for the imbalance and correct the frequency deviation. This avoids inter-area dispatch of power and unnecessary exchange of information. However, in situations where the local resources are insufficient for full compensation for the disturbance, inter-area dispatch of resources becomes necessary.

To minimize increased losses due to the inter-area power dispatch, the electrical distance between the area and neighboring areas is assessed using effective impedance. For the protection of information privacy in the local areas, the alternating direction method of multipliers (ADMM) is leveraged to break down the optimization into smaller pieces by an iterative process and to keep information about the inverter-based resources in the local areas [7].

4.1.2 Gradient-Based Voltage Control

The integration of inverter-based resources also poses challenges to traditional voltage regulation schemes. The volatility in the generation of these resources makes voltage limit violations more frequent and intricate to manage. However, if properly controlled, these resources can be valuable assets in assisting voltage regulation with the fast response capability of their inverters.

Conventional voltage regulation methods integrate various resources including inverter-based ones and seek reactive power flow solutions to schedule the dispatch. However, this relies on reliable load and generation forecasting, which is becoming more volatile nowadays due to variations in the renewables [83]. Hence, researchers developed

closed-loop control methods that take advantage of real-time measurement feedback from PMUs [84]. Reference [8] further improved the closed-loop control philosophy by including the gradient method to find the appropriate resource commands to compensate for the reactive power disturbances with an approximated model. The voltage regulation problem is formulated as an optimization problem [8]:

$$\begin{aligned} & \min_{\mathbf{u} \in U} f + h_v(\mathbf{v}_l) + h_q(\mathbf{q}_v) \\ f &= (\Delta \mathbf{q}_i)^T \mathbf{R}_c (\Delta \mathbf{q}_i) + (\Delta \mathbf{q}_g)^T \mathbf{R}_g (\Delta \mathbf{q}_g) + (\Delta \mathbf{q}_s)^T \mathbf{R}_s (\Delta \mathbf{q}_s). \\ & \text{s. t. } (\mathbf{q}, \mathbf{v}_l) = \mathbf{g}(\mathbf{u}, \mathbf{w}) \end{aligned} \quad (4-3)$$

where $\mathbf{q} = [\mathbf{q}_i^T, \mathbf{q}_g^T, \mathbf{q}_s^T]^T$ are reactive power of the inverter-based resources, generators, and SVCs. $h_v(\mathbf{v}_l)$ and $h_q(\mathbf{q}_v)$ are penalty functions representing the violations of load-bus voltages and the reactive power output limits of the resources. The factors $\mathbf{R}_c, \mathbf{R}_g, \mathbf{R}_s$ are weights that indicate the priority indices of the different kinds of resources. The control commands \mathbf{u} can be solved step by step:

$$\mathbf{u}(k+1) = P_U \left[\mathbf{u}(k) - \tau \left(\Pi_1^T \nabla f(k) + \Pi_2^T \nabla h_v(k) + \Pi_3^T \nabla h_q(k) \right) \right] \quad (4-4)$$

where $\Pi_1^T, \Pi_2^T, \Pi_3^T$ are the Jacobian matrices calculated from the system admittance matrices.

This work targets the implementation and testing of the frequency and voltage control proposed in references [7] and [8] on the large-scale 5000-bus New York State Grid system administered by the New York Power Authority (NYPA). The controllers are implemented on National Instruments' CompactRIO hardware controller system, and a hardware-in-the-loop (HIL) testing platform is constructed with a power system simulator to provide the testing environment where the 5000-bus NYPA system is simulated in real time.

4.2 Implementation of the Control Schemes on Hardware

The frequency and voltage control schemes are implemented on a hardware controller platform and tested on an OPAL-RT-based HIL testing environment with a realistic 5000-bus NYPA system constructed on the real-time simulator. This section discusses the implementation of the hardware controller, the NYPA model on the real-time simulator, and the structure of the HIL testing platform.

4.2.1 Hardware Implementation of the Controllers

The voltage and frequency controllers have been implemented on National Instruments' hardware controller platform CompactRIO 9035. As the voltage control is a centralized, gradient-descent-based control algorithm, it is implemented through MATLAB code adjusted for real-time execution on CompactRIO. The frequency control, however, was first converted to C code and then compiled as a "shared library" that can be called upon by the CompactRIO hardware as the optimization algorithms could not be directly implemented through the CompactRIO programming language LabVIEW. Figure 4-2 shows the structure of the frequency controllers and the communication as an example.

The communication between the controllers and the OPAL-RT real-time simulator is realized by the C37.118 protocol over TCP/IP. The C37.118-based measurement receiving function and control command sending functions are implemented on CompactRIO, as shown in the right half of Figure 4-3 with the built-in user interface of the real-time simulator on the left.

4.2.2 Real-time Simulation of the 5000-bus New York State Grid

The 5000-bus NYPA model is used for testing the hardware voltage and frequency controllers. The original NYPA model was built in PSS/E for offline simulation and

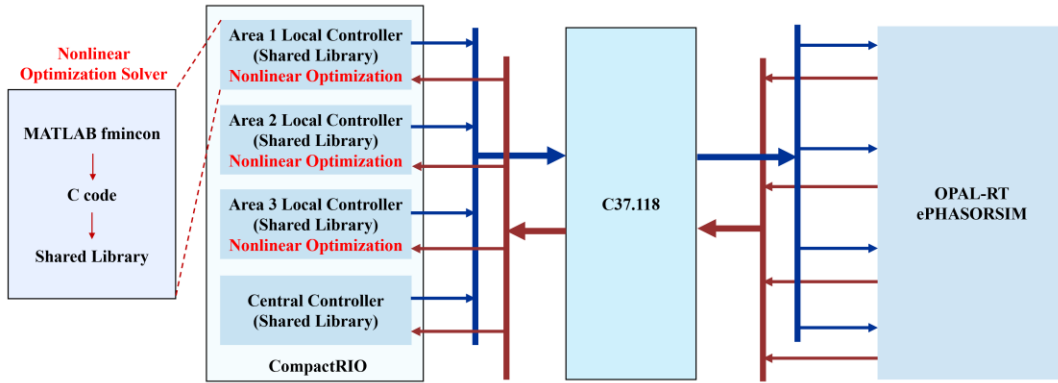


Figure 4-2 Structure of the HIL platform

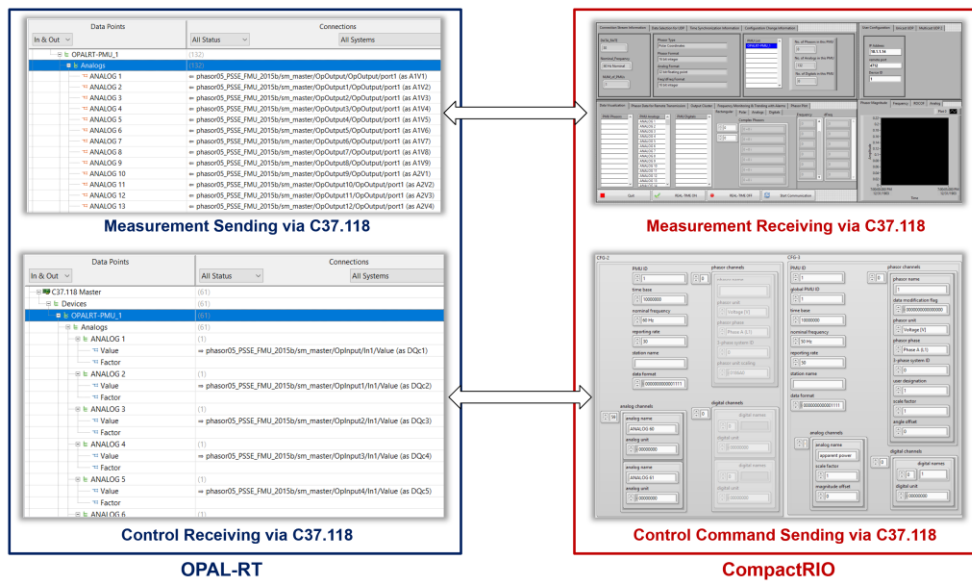


Figure 4-3 Implementation of C37.118 communication within the HIL platform

studies. To achieve real-time simulation and controller testing, the model has been implemented on ePhasorSim for OPAL-RT real-time execution.

Since OPAL-RT ePHASORSIM does not have built-in inverter-based systems with both active and reactive power control capabilities, a user-defined model has been constructed on OpenModelica, as shown in Figure 4-4 [85]. Figure 4-5 shows the overall structure of the ePHASORSIM model structure with measurements and control interfaces for the voltage control. The frequency control implementation has a similar structure.

Before any real-time hardware-in-the-loop testing can be conducted with the OPAL-RT model, its steady-state (power flow) and dynamic response should be validated to ensure proper operation of the real-time implementation of the NYPA model. Table 4-1 shows the comparison of power flow results on the real-time simulator OPAL-RT and the offline simulator PSS/E. On voltage levels of 500 kV, 345 kV, and 230 kV, the buses with maximum voltage phasor differences, along with four randomly chosen buses are presented in the table. It is noticed that the real-time simulator gave precise voltage magnitude initial values as compared to the offline simulation, with a maximum difference of 0.0018 p.u. on the 345 kV network. The maximum angle difference on the three voltage levels is 0.4481 degrees. This corresponds to 0.18% and 0.12% of errors in voltage magnitude and angle between the real-time and offline simulators. Hence, the power flow result on OPAL-RT is considered accurate for providing good initial conditions for the dynamic simulations.

The verification of dynamic transients on the real-time simulator OPAL-RT is done through two perspectives: the frequency and voltage dynamics and the response of the user-defined inverter-based resource model.

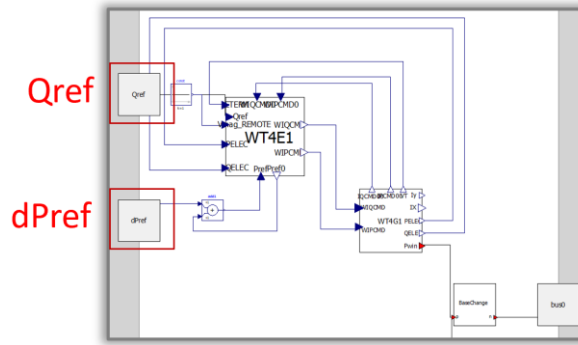


Figure 4-4 The IBR model on OpenModelica

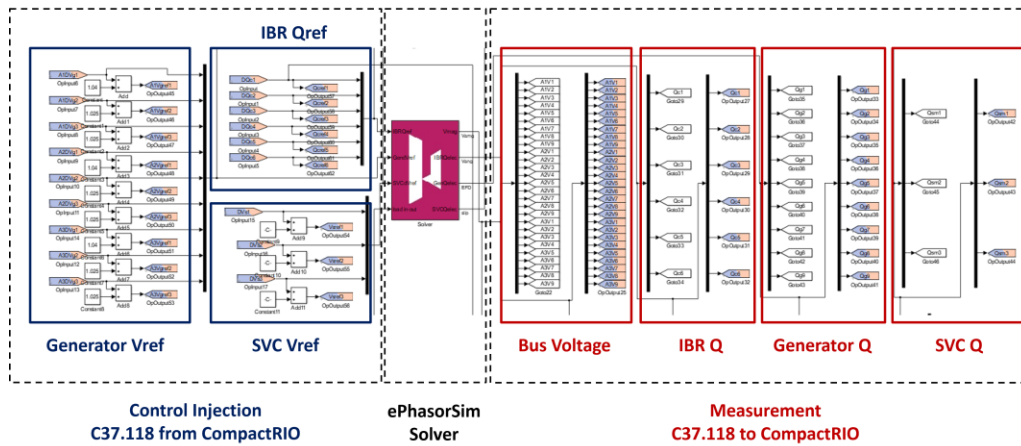


Figure 4-5 OPAL-RT ePHASORSIM implementation structure

Table 4-1 Comparison of power flow results in OPAL-RT and PSS/E

Bus Number	Base Voltage (kV)	Area Name	Voltage Magnitude (p.u.)		Voltage Angle (deg.)		Magnitude Difference (p.u.)	Angle Difference (deg.)
			OPAL-RT	PSS/E	OPAL-RT	PSS/E		
360090	500	TVA	1.0294	1.0295	-32.1030	-28.8905	-0.0001	0.2092
235103	500	AP	1.0448	1.0445	-80.9900	-77.4997	0.0003	-0.0685
200094	500	PJM	1.0261	1.0272	-111.4260	-108.0605	-0.0011	0.0563
156000	500	IESO	1.0524	1.0524	-59.6320	-56.2400	0.0000	0.0298
314916	500	DVP	1.0535	1.0534	-91.9740	-88.5323	0.0001	-0.0199
190416	345	NB	1.0262	1.0262	-26.7780	-23.8043	0.0000	0.4481
348850	345	AMIL	1.0372	1.0365	-37.5460	-33.7400	0.0007	-0.3842
345046	345	AMMO	1.0167	1.0167	-29.8110	-26.1418	0.0000	-0.2475
253027	345	DAY	1.0010	0.9992	-67.9820	-64.3504	0.0018	-0.2099
532796	345	WERE	1.0014	1.0014	-38.1900	-34.6500	0.0000	-0.1182
147846	230	NYISO	1.0293	1.0293	-45.7820	-42.6400	0.0000	0.2798
130768	230	NYISO	1.0173	1.0174	-79.8110	-76.5500	-0.0001	0.1607
213586	230	PECO	1.0167	1.0168	-111.6930	-108.3600	-0.0001	0.0888
336137	230	EES	0.9820	0.9818	-33.1220	-29.7500	0.0002	0.0498
204502	230	METED	1.0119	1.0120	-99.0240	-95.6500	-0.0001	0.0478

The frequency response after a load pickup of 800 MW active power is shown in Figure 4-6. (a). The real-time and offline simulation match well both in steady state and during transients. The largest difference in frequency is less than 1 mHz, which is less than the typical tolerable error of synchrophasor devices and is caused by differences in the modeling of generator exciters and power system stabilizers. This is also visible in the voltage magnitude plots in Figure 4-6. (b) and Figure 4-6. (c). These minor differences are acceptable in the hardware-in-the-loop testing as the purpose of the NYPA model migration is for testing the controllers instead of a perfect match of simulation results. Meanwhile, since the frequency and voltage controllers are measurement-based, they are adaptive to various scenarios by adjusting their control outputs automatically based on feedback signals.

In addition, the user-defined model built for inverter-based resources is tested individually in the hardware-in-the-loop testing platform. This helps verify the response of the IBR models to control commands, and at the same time, helps identify the closed loop time delay in the HIL setup. Figure 4-7 shows the timeline of signals being exchanged between the real-time simulator and the hardware controller.

The testing begins with an IBR active power reference being sent at t_0 from the real-time simulator to the hardware controller through C37.118 over TCP. At $t = t_1$, the reference is received by the controller. At $t = t_2$, the reference is sent out from the controller back to the simulator and it is received by the simulator at $t = t_3$. As the final step, the active power reference is injected into the activation IBR and the moment the active power change in the output of the IBR happens is recorded as t_4 .

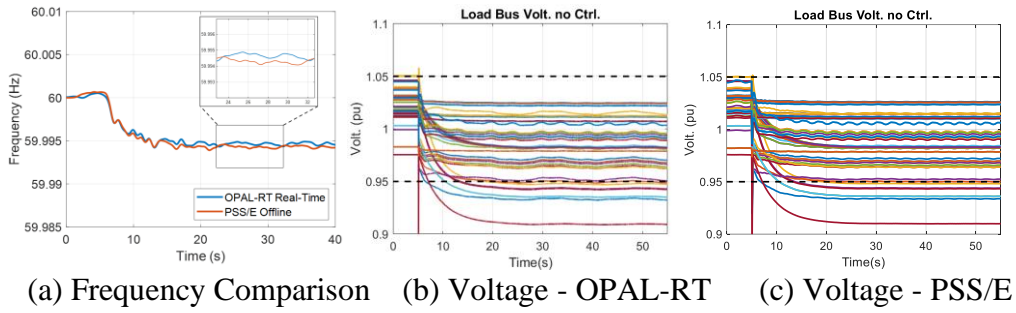


Figure 4-6 Comparison of load bus voltages

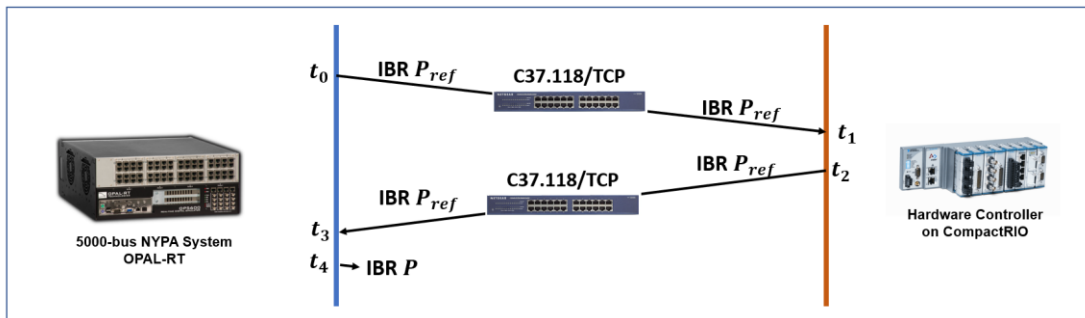
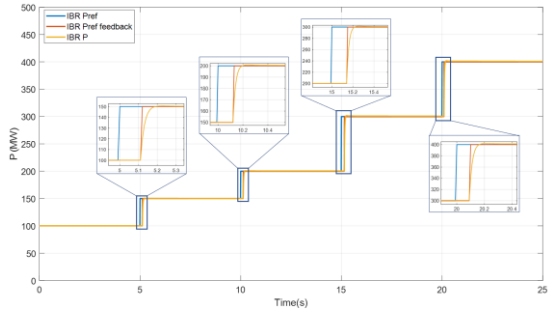


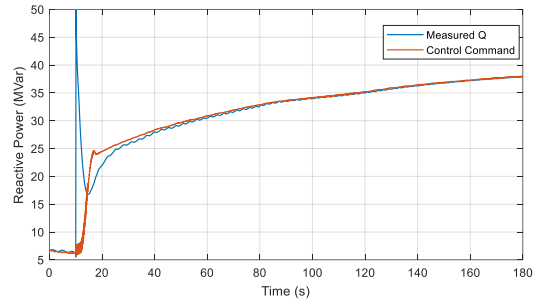
Figure 4-7 Timeline of IBR control and communication delay testing

With real-time data logging in the simulator, t_0 , t_3 , and t_4 are accurately recorded. The difference between t_0 and t_3 reflects the closed-loop communication and execution delay Δt_{comm} ; the difference between t_0 and t_4 is the closed-loop delay between observation and actuation; the difference between t_3 and t_4 is the delay of the inverter-based resources to fully execute the control commands.

The IBR actuator outputs 100 MW in its initial state before the testing. During the testing, four step increases in the active power reference were issued consecutively with 5-second intervals. The first two increases are 50 MW and the following two increases are 100 MW each. Figure 4-8 (a) plots the data-logging results of the initial active power reference sent from the real-time simulator (blue), the reference feedback from the controller as received at the simulator (orange), and the measured active power output of the actuator IBR (yellow). Table 4-2 summarizes the communication/controller execution delay and the IBR response time results obtained from the four step changes. The average closed loop delay due to communication and controller execution is 125 ms. The control execution cycle of the hardware controller is 40 ms, which introduces a 40 ms uncertainty into this closed-loop delay as the testing can fall at any phase in the control cycle. Taking this into consideration, it is safe to assume that the closed-loop delay is about 100 ms. Another delay measured in the testing is the time that the IBR took to follow the commands. After receiving the step change in the control commands of active power, the IBR took consistently 80 ms to reach to designated new output level with minimum overshoot. Since the IBR model in the New York State Grid model is active power prioritized, and its reactive power control takes both the Q command and the auxiliary input based on terminal voltage, the validation of reactive power is confirmed by comparing the measured reactive



(a) Active power test



(b) Reactive power test

Figure 4-8 Closed-loop testing of IBR control and communication delay

Table 4-2 Closed-loop IBR response and communication delay

Step Signal	Time (s)	MW Change (MW)	$\Delta t_{comm} = t_3 - t_0$ (s)	$\Delta t_{IBR} = t_4 - t_3$ (s)
#1	5	50	120	80
#2	10	50	130	80
#3	15	100	150	80
#4	20	100	100	80
Average	-	-	125	80

power and the command from the controller, as shown in Figure 4-8 (b). The reactive power output of the IBR accurately followed the control command, except for a spike at the beginning of the disturbance. This is because the IBR is designed to quickly respond to large voltage deviations through auxiliary reactive power modulation for improved voltage transients. The performance of the IBR actuator model is satisfactory in following the control accurately and promptly.

4.3 Hardware-in-the-Loop Testing Results

4.3.1 Frequency Control

In the testing of the frequency control, three areas with existing or planned IBR deployment that can be utilized for these controls are identified, namely areas I (Dunwood), J (New York City), and K (Long Island) in Figure 4-9. Six plants with inverter-based resources in these areas are utilized for fast frequency recovery. The information about the IBRs used for actuation is listed in Table 4-3.

To verify the ability of the controller to promptly mobilize IBRs in response to frequency disturbances, a step change in load is introduced by picking up active power load in an area with varying sizes to create frequency fluctuations. For brevity, two representative cases are presented here: a 300 MW and an 800 MW active power load pickup in Area J (New York City) at bus 234352 (bus number altered to comply with confidentiality requirements). Considering the total headroom available under this frequency control scheme in Area J is 500 MW, the first disturbance shall be compensated with solely IBRs within the area, while the second disturbance requires additional support from neighbor areas.

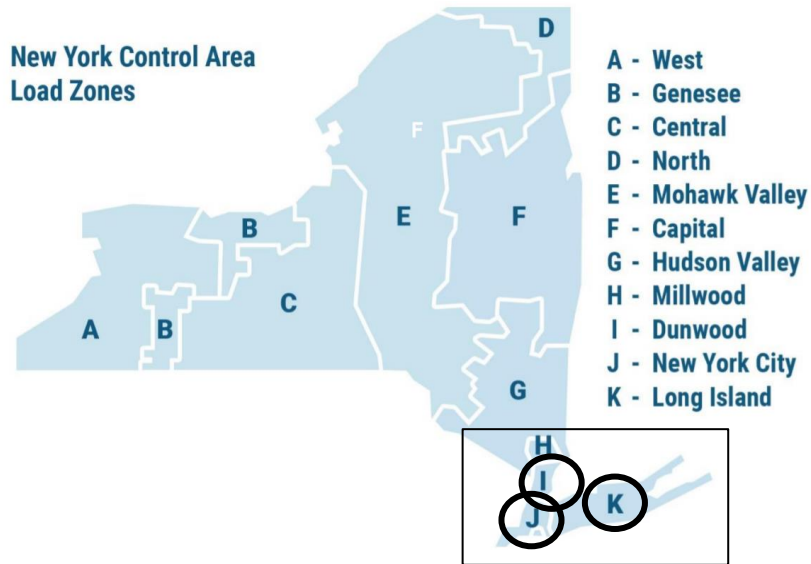


Figure 4-9 Areas identified for frequency and voltage control actuators

Table 4-3 IBRs in Areas I, J, and K

Area	IBR Bus	IBR Capacity (MVA)	IBR Headroom (MW)	IBR Initial Output (MW)
I (Dunwood)	249724	500	400	50
	249737	500	100	50
J (New York City)	320359	1300	400	100
	255743	1272	100	150
K (Long Island)	529382	880	400	200
	382923	150	100	50

*Bus numbers have been altered to comply with confidentiality requirements

(a) 300 MW Active Power Load Pickup

Area J is one of the load centers in the NYPA system. In this testing, a 300 MW active power load pick is used to test the response of the control scheme. The two actuators in Area J, IBRs at buses 320359 and 255743, have capacities of 1300 MVA and 1272 MVA, among which 400 MW and 100 MW were assigned as headroom for this control scheme. The control command, IBR active power output, and area frequencies are shown in Figure 4-10.

The central controller only mobilized IBR resources within Area J, as shown in Figure 4-10. (a) and Figure 4-10. (b), where the disturbance occurred since the size of the disturbance can be covered with a total headroom of 500 MW in the area. While the no control case (blue dash line) saw frequency decline and stabilized at 59.995 Hz after 10 seconds of the event occurrence, the case with frequency control had the frequency recovered back to pre-disturbance levels within 1 second. The steady-state frequency deviations in all areas are smaller than 0.0005 Hz.

Figure 4-11 shows the control flag within the central controller. There are four statuses of the central controller control flag: Status 0 – Control not enabled; Status 1 – Control enabled, local IBR support only (no inter-area support not initiated); Status 2 – Control enabled, inter-area IBR support in progress; Status 3 – Control enabled, inter-area IBR support reached a steady state and is sustained.

Since the size of the disturbance (300 MW) was covered by the two actuators within the area, the central controller control flag stayed at status 1 throughout the testing.

During the mobilization of the IBRs in Area J, the controller actively controlled the sharing of the loading among the two IBRs. Table 4-4 shows the initial values and changes

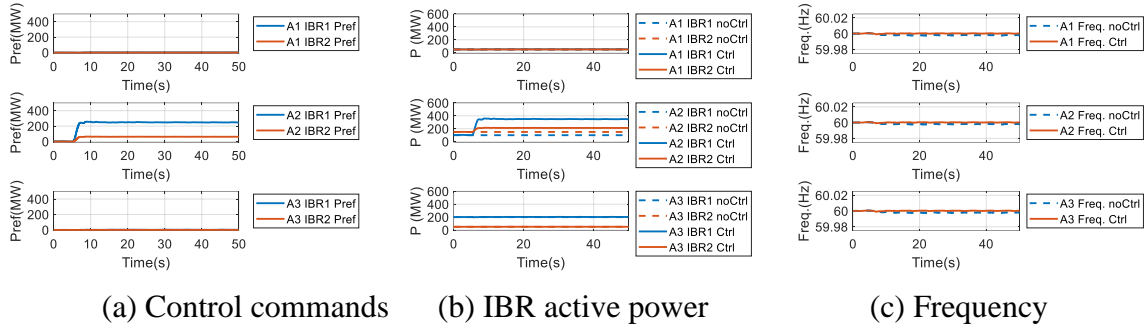


Figure 4-10 Control commands, active power, and frequency

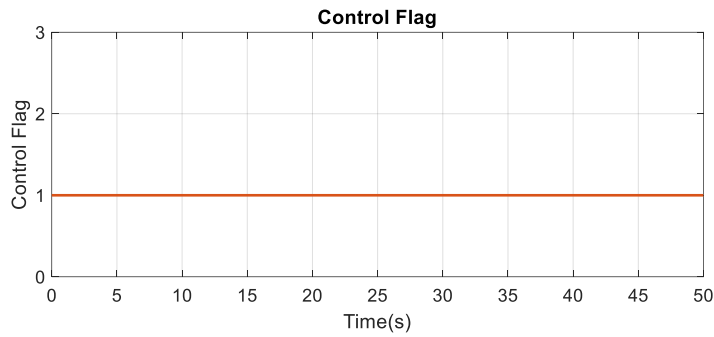


Figure 4-11 Control flag in the central controller (300 MW)

Table 4-4 IBR active power output in the 300 MW disturbance testing

	Area I IBR 1	Area I IBR 2	Area J IBR 1	Area J IBR 2	Area K IBR 1	Area K IBR 2
Before Disturbance	50 MW	50 MW	100 MW	150 MW	200 MW	50 MW
After Disturbance	50 MW	50 MW	350 MW	212 MW	200 MW	50 MW
Change	0 MW	0 MW	250 MW	62 MW	0 MW	0 MW

in the active power output of the IBRs. It is noted that the IBR 1 and IBR 2 in Area J shared the load proportionally to their headroom available (400 MW / 100 MW).

(a) 800 MW Active Power Load Pickup

In this testing case, the disturbance was increased to 800 MW, which is larger than the total headroom within the area (500 MW) – support from neighboring areas will be required. Table 4-5 shows the active power output from the actuators, and Figure 4-12 shows the power and frequency. As the 800 MW disturbance is larger than the total headroom in Area J, the central controller mobilized all actuators across the three areas.

The IBR 1 and 2 in Area J, where the disturbance occurred, were immediately controlled to quickly ramp up their active power output from 100 MW and 150 MW to 500 MW and 250 MW, respectively, to make use of all their headroom. As this is not sufficient to recover the frequency to the pre-disturbance level, IBRs in areas I and K are also activated to support Area J. As Area I is electrically closer to Area J, IBRs in Area I are taking up a larger share of the power deficiency (228 MW) compared to that in Area K (88 MW). Within each area, the sharing of the MW among the actuators is still based on the headroom available from the IBRs. With the instant support from local IBRs and fast inter-area support from neighboring areas, the frequency recovered within 4 seconds. The steady-state frequency deviation post-disturbance in all areas are smaller than 0.0005 Hz (8e-6 p.u.).

The control flag in the central controller is shown in Figure 4-13. Although the frequency recovered quickly, the central controller control flag has been alternating between statuses 2 (initiated mobilizing inter-area support) and 3 (inter-area support realized) continuously. This is because the frequency has tiny fluctuations (less than 1 mHz)

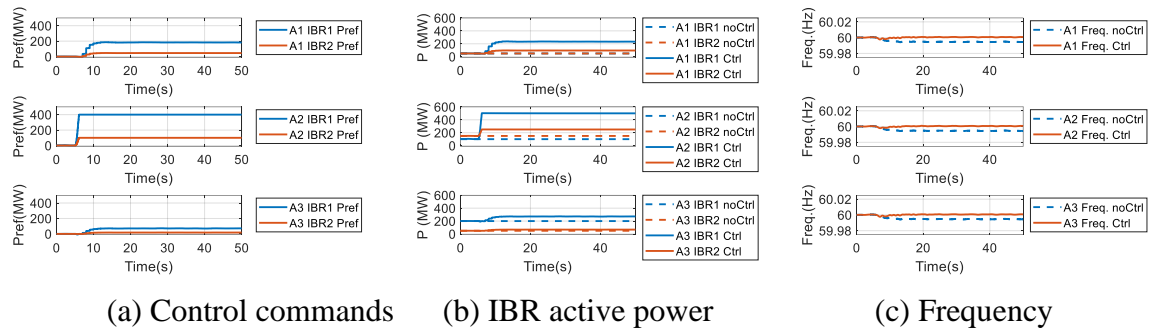


Figure 4-12 Control commands, active power, and frequency

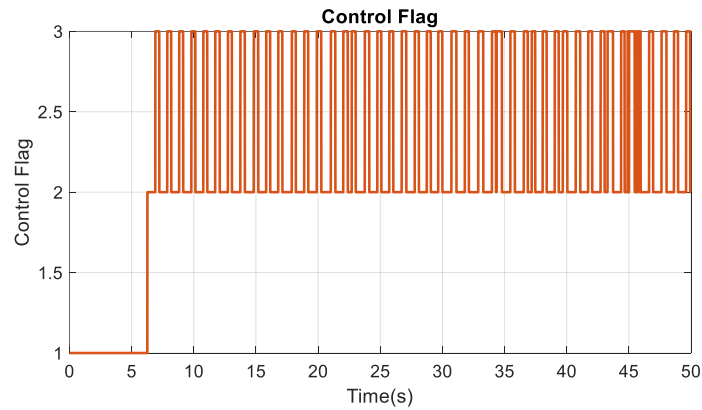


Figure 4-13 Control flag in the central controller (800 MW)

Table 4-5 IBR active power output in the 800 MW disturbance testing

	Area I IBR 1	Area I IBR 2	Area J IBR 1	Area J IBR 2	Area K IBR 1	Area K IBR 2
Before Disturbance	50 MW	50 MW	100 MW	150 MW	200 MW	50 MW
After Disturbance	233 MW	95 MW	500 MW	250 MW	270 MW	68 MW
Change	183 MW	45 MW	400 MW	100 MW	70 MW	18 MW

so the central controller continuously optimizes the inter-area dispatch and ensures a stable system frequency.

4.3.2 Voltage Control

As discussed in section 4.1.2, the voltage controller coordinates three types of reactive power resources, IBRs, generators, and SVCs. The built-in flexibility of the gradient-descent-based voltage control scheme enables a variety of coordination strategies that can be used according to the needs of application scenarios. For example, the steady-state reactive power response sharing can be coordinated by assigning different weight combinations to \mathbf{R}_c , \mathbf{R}_g , and \mathbf{R}_s in equation (4-3). To coordinate the transient response, heterogeneous gradient-descent step sizes are assigned to the three types of resources by configuring the step size matrix $\boldsymbol{\tau}$ in equation (4-4). Two testing scenarios are presented in this section, the generator priority case where the generators take the responsibility for steady-state reactive power output and the IBR priority case where the IBRs take responsibility for the steady-state outputs. The disturbance used in both testing cases is a 300 MVar step change in a reactive load.

(a) Generator Priority Case

In this testing case, \mathbf{R}_g in equation (4-3) is set to \mathbf{I} , and \mathbf{R}_c , \mathbf{R}_s are set to $100 \cdot \mathbf{I}$ (\mathbf{I} stands for the identity matrix) such that the generators are prioritized to maintain steady-state reactive power compensation when the objective function is minimized. The gradient-descent step sizes for the generators, IBRs, and SVCs are 0.0000025, 0.00001, and 0.0000025.

A comparison is made for load bus voltages with and without the voltage controller being enabled. Voltage violation is defined as voltage excursion from the range 0.95 to 1.05.

As shown in Figure 4-14, several load buses violated the limit without the controller, while all of them are regulated back above the lower limit within 10 seconds when the proposed controller is enabled.

As the generators are prioritized to support the reactive power needed to regulate the voltage, the generators experienced an increase in their terminal voltages because of the control commands injected into their exciters, as shown in Figure 4-15. (a). The eight generators participating in the voltage control scheme increased their reactive power output by 91.5 MVar, as shown in Figure 4-15. (b).

As expected, the IBRs and SVCs quickly responded to the voltage transient by rapidly injecting reactive power in the first few seconds following the disturbance, as shown in Figure 4-16. However, they soon leveled down their output since the control prioritizes the generators to support the steady-state need for the reactive power deficiency. In this way, the IBRs, SVCs, and traditional generators are coordinated to provide satisfactory transient and steady-state reactive power regulation amid disturbances.

(b) IBR Priority Case

In this testing case, the IBRs are not only expected to provide a fast response during transient but also prioritized to sustain steady-state reactive power support after the disturbance. This coordination can be used when BESSs have high state-of-charge levels, or it is favorable to make use of spare capacity in renewable generation. The coordination parameter matrices are set as: $\mathbf{R}_c = \mathbf{I}$, $\mathbf{R}_g = \mathbf{R}_s = 100 \cdot \mathbf{I}$, which will allow the IBRs to take the most steady-state reactive power responsibilities when the objective function is minimized. The gradient-descent step size for the generators, IBRs, and SVCs are 0.000001, 0.00004, and 0.000001.

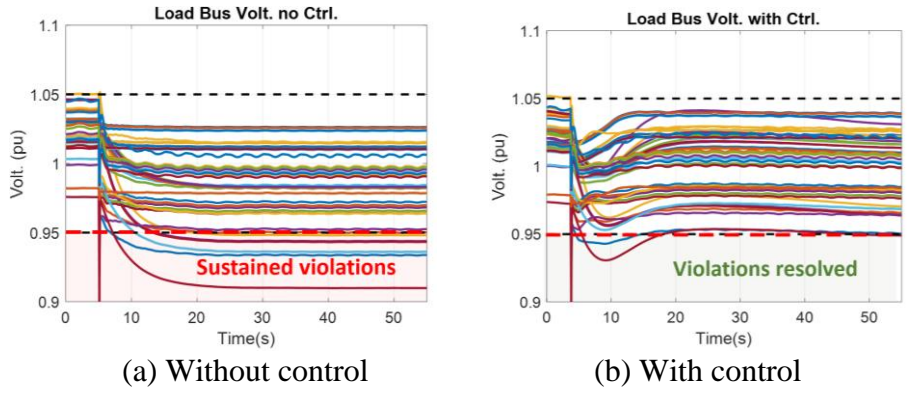


Figure 4-14 Load bus voltages with and without control

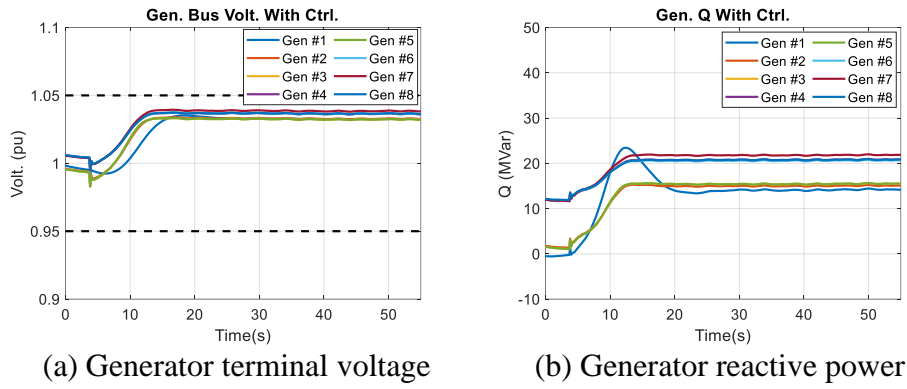


Figure 4-15 Voltage and reactive power at participating generators

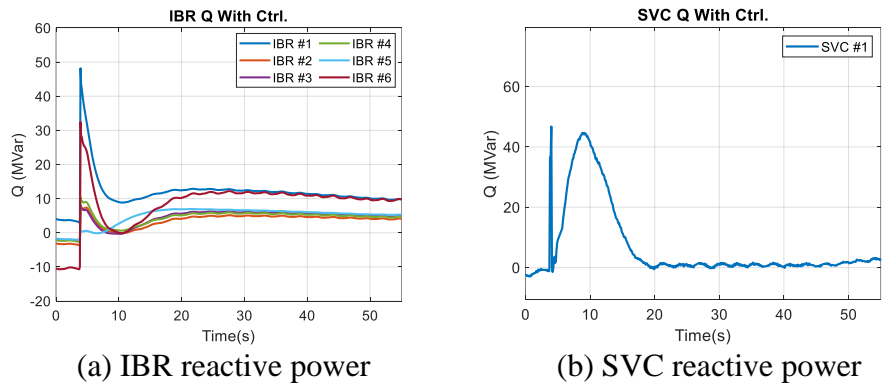


Figure 4-16 Reactive power of IBRs and the SVC

As shown in Figure 4-17, with the fast and lasting IBR response to the voltage transients, the violations at load buses were resolved within 5 seconds, which was faster than the generator priority case. As the controller puts generators at a lower priority, the changes in generator voltage and reactive power are minimal (Figure 4-18). As can be seen in Figure 4-19, the IBRs participated in fast response instantly after the disturbance and provided a 150 MVar of steady-state reactive power support. The SVC provided a transient response to the voltage dip with minimal sustained reactive power support as expected.

4.4 Summary

The voltage and frequency controllers are designed for the New York State Grid to take advantage of synchronized measurements and inverter-based resources, which expedites the recovery process and increases flexibility in the coordination of IBRs with traditional resources. The frequency controller actively estimates the power disturbances in each controlled area through measurements on IBRs and tie-lines. This facilitates accurate frequency recovery to the nominal value. The control prioritizes local compensation for quick and efficient frequency recovery, but it can also mobilize resources from neighboring areas when local support is not sufficient. The voltage controller uses the gradient method to flexibly coordinate a mix of resources for containing target load bus voltages within a pre-defined range

A 5000-bus NYPA system is implemented on the real-time simulator for testing the voltage and frequency controllers. Both the steady-state power flow results and frequency/voltage dynamics are verified before the real-time model is used for hardware-in-the-loop testing of the controllers. Both the voltage and frequency controllers are implemented on hardware (the CompactRIO system). In the testing, the frequency

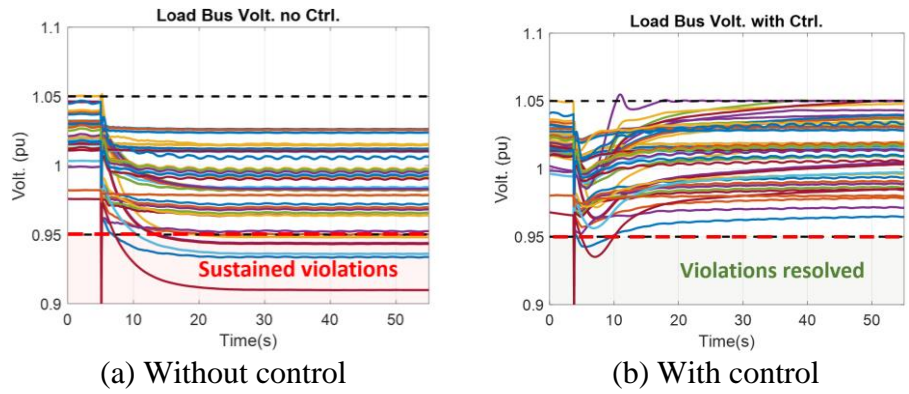


Figure 4-17 Load bus voltages with and without control (IBR priority)

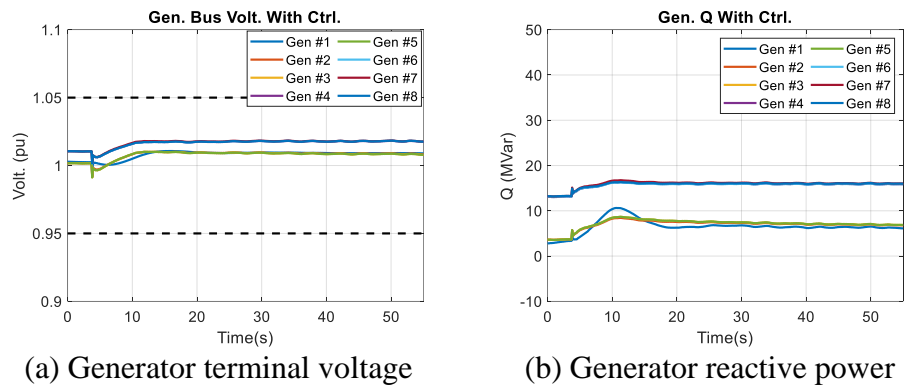


Figure 4-18 Voltage and reactive power at participating generators

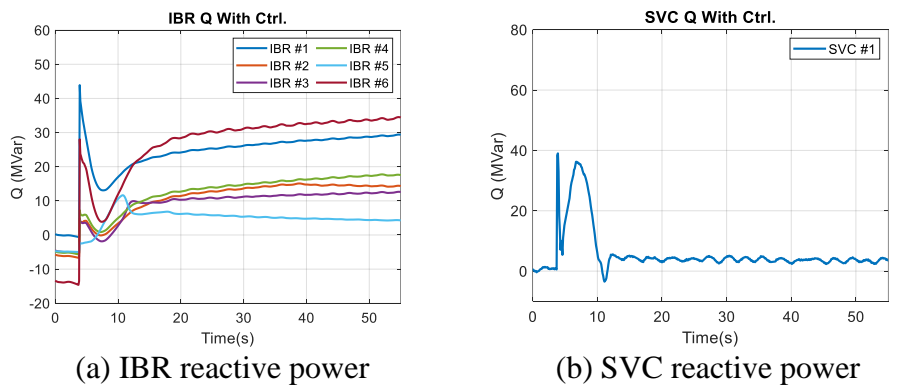


Figure 4-19 Reactive power of IBRs and the SVC

controller accurately recovered system frequency to the nominal within 1 second when only local response is leveraged and 4 seconds when inter-area support is needed. The voltage control successfully coordinated different resources according to the given priority indices and contained the voltage deviation within the pre-defined limits of (0.95, 1.05) on all load buses.

In future work, the coordination of the frequency and voltage controller with traditional frequency/voltage control strategies is to be investigated. In addition, strategies to adaptively compensate for communication uncertainties will be developed to enhance the robustness of the controllers.

CHAPTER 5. MEASUREMENT-BASED REAL-TIME POWER MANAGEMENT FOR MICROGRIDS WITH DYNAMIC BOUNDARIES

While the rapid increase of renewable resources at the distribution level brings volatility and challenges to the operation of distribution networks, the development in measurement, communication, and remotely controllable smart switches opens the possibility to more efficient and resilient operation of distribution feeders. This section proposes a measurement-based real-time power management design for the operation of utility-owned feeder microgrids with dynamics boundary capabilities for increased flexibility and reduced deployment cost.

It should be noted that part of the content in this chapter is from the author's journal paper published in the IEEE Access journal in 2022 [11].

5.1 Introduction

To increase the efficiency and reliability of distribution network services, microgrids have been promoted in recent years as a highly controllable entity in grid-connected mode and a measure to reduce service disruptions in islanded mode, especially for critical loads. This has become practical with the rapid deployment of distributed energy resources (DERs) of various kinds, such as photovoltaic (PV) systems, wind turbines, backup generators, and battery energy storage systems (BESSs). Microgrids started with a fixed electric boundary and fixed point of common coupling (PCC), which establish a clear electric boundary between the utility and the microgrid. Microgrids were also designed to sustain self-sufficiency when islanded [86], [87]. This philosophy puts strict requirements

on the sizing and operation planning of BESSs as they are expected to handle the intermittency in other DERs and loads that are stochastic in nature.

Microgrids with dynamic boundaries, on the other hand, enable more flexible operations by altering the electric boundaries to accommodate changes in loads, generation availability, and faults. With the increasing deployment of sectionalizing smart switches that are originally installed for fault isolation and load restoration, researchers envision more proactive control over the electric boundaries by fully utilizing the potential of these smart switches' capability of measurement, communication, and control. This enables increased utilization of renewables with reduced size of energy storage systems [9].

Related investigations on increasing flexibility during load restoration and island formation have drawn attention in the research community. A flexible island-forming strategy through clustering methods is proposed in [10] with consideration of the stochastic variations in loads and DERs. A load restoration strategy is given in [88] to mitigate the impact of fault events with active control over the operation modes of distributed generations (DGs) and the determination of appropriate boundaries. Microgrid formation is further formulated as an optimization problem in [89] to maximize service to critical loads and to maintain frequency and voltage in appropriate ranges. In addition, strategies are proposed to improve system reliability and performance by taking advantage of operation modes and controls over DERs [90-92]. However, these studies are focused on the optimization of the formation and economic operation of microgrids, instead of real-time islanded control of dynamic-boundary microgrids.

The restoration and control procedure proposed in [93] accommodates the concept of dynamic boundary in practical restoration and operation, but it requires heavy involvement

of operator decisions and actions in the selection and implementation of boundary changes. The energy management tool developed in [94] incorporates the automated shedding of non-critical loads and PV curtailment, but the procedure is highly specific for certain operating scenarios and lacks the adaptability to dynamically changing topologies in dynamic-boundary microgrids. To enable adaptive, automated dynamic boundary changes in real-time operation, a topology-adaptive controller is proposed in [87], [95-98], which maximizes the utilization of renewable energy sources by handling rapid changes with real-time (on a time scale of seconds) boundary shrinking and expansion capabilities. However, it is assumed that there is only one source location accompanying the critical load section in the microgrid.

With the rapidly dropping price of DERs, a pronounced need for new DER deployment has been shown, and the reprioritization of more load sections is made possible by such developments. The need for multiple source locations, combined with the requirement for dynamic boundaries and adaptability to arbitrary non-mesh topologies, drastically increases the complexity of topological variations, the change in operation modes, and the coordination between different islands and sources. When islanded from the grid, a dynamic-boundary microgrid with multiple source locations can be operated as multiple single-source-location islands, a mix of multiple-source-location islands and single-source-location islands, or a single merged microgrid with multiple source locations. At the same time, all islands are capable of expanding/shrinking their electric boundaries and merging/separating with/from other islands, leading to a wide variety of operation conditions and transitions. Research and development are lacking on measurement-based, adaptive power management modules that are aimed at handling, in real-time, the

increasingly complex topology changes and operation transitions arising from multiple-source-location dynamic-boundary microgrids.

In addition, the coordination among DERs on power sharing becomes essential in microgrids with multiple source locations. Researchers investigated automated methods to fulfill power sharing objectives for interconnected microgrids, in both traditional AC microgrids [99], [100] and AC/DC hybrid microgrids [101], [102]. While these studies provided advanced solutions for power sharing in AC and hybrid microgrids with multiple source locations by dispatching power through advanced secondary controls over DERs or interlinking converters, they typically have dedicated designs for specific microgrids with fixed boundaries and lack the flexibility to topology variations. As the islands forming around multiple source locations expand, shrink, merge, or separate freely during islanded operation, the power sharing and frequency regulation functions should also be able to handle such increased topological and operational variations with the assistance of various measurement feedback.

To address the needs discussed above, a power management module is proposed and implemented to enable fully automated, highly adaptive, and real-time management of microgrids with dynamic boundaries and multiple source locations. For brevity, the term ‘sub-MG’ will be used in the following text to represent any partial islands in a microgrid, including both single-source-location islands and multiple-source-location islands. The module addresses the following challenges:

- a) The increased complexity of operation scenarios and transitions accompanying the topological changes in the operation of microgrids with dynamic boundaries and multiple source locations. This affects all functions in the module, including

dynamic boundary, sub-MG merging/separation, and power sharing.

- b) The flexibility requirement on the algorithms to be automatically adaptable to arbitrary non-mesh topologies for handling wide variations in the topology in multiple-source, dynamic-boundary microgrids. This also facilitates expedited, low-cost deployment of the controller with a reduced cost at new microgrid sites with different topological configurations.
- c) The real-time execution requirement on practical hardware controllers.

Correspondingly, the power management module is equipped with the following novel features:

- a) Topology awareness and analysis based on linear programming, which is suitable for practical hardware implementation to support real-time, simultaneous management of dynamic boundaries of multiple sub-MGs forming around multiple source locations.
- b) Automatic merging and separation of the sub-MGs and adaptability to topology variations under various operation conditions and transitions.
- c) Automatic power sharing and secondary frequency regulation with real-time adaptability to topological variations
- d) Fast, low-cost deployment at new microgrid sites as a result of the built-in adaptability of the module to arbitrary non-mesh topologies.

5.2 Structure of the Flexible Microgrid Controller

The microgrid controllers developed at the University of Tennessee aim to facilitate fast, scalable, and low-cost deployment of microgrid solutions [103]. The control solution is hierarchically structured with a microgrid central controller (MGCC) and several local

controllers (MGLC) depending on the number and location of controllable DERs. The MGCC has a comprehensive set of function modules to cover the operation of a microgrid with dynamic boundaries, including model management, topology identification, black start, power management, planned/unplanned islanding, reconnection, PV/load forecasting, energy management, relay protection, data logging, etc. Figure 5-1 shows an overview of the function modules in the MGCC, where they are categorized into four groups based on their functionalities, namely communication, situational awareness, control, and auxiliary modules. The data flow between these categories is indicated by arrows of different colors.

More details about the design of the central controller, the data flow, and the coordination among the function modules can be found in the reference [12]. A few modules related to real-time control are introduced as follows:

- *Topology Identification.* The flexible operation of the microgrid starts from the real-time topology awareness made possible by the Topology Identification module. It automatically updates (sub-)MG topology matrices based on the statuses of smart switches. These matrices will be fed to other real-time control modules like power management, reconnection, planned islanding, etc.
- *Power Management.* The power management module is designed to maintain the balance of active and reactive power by managing the dynamic boundaries and the operation of DERs. The module takes various inputs from topology identification, power/voltage measurements on smart switches and DERs, and commands from the finite state machine to provide real-time, coordinated power management.
- *Planned Islanding.* The Planned Islanding module separates a microgrid from grid

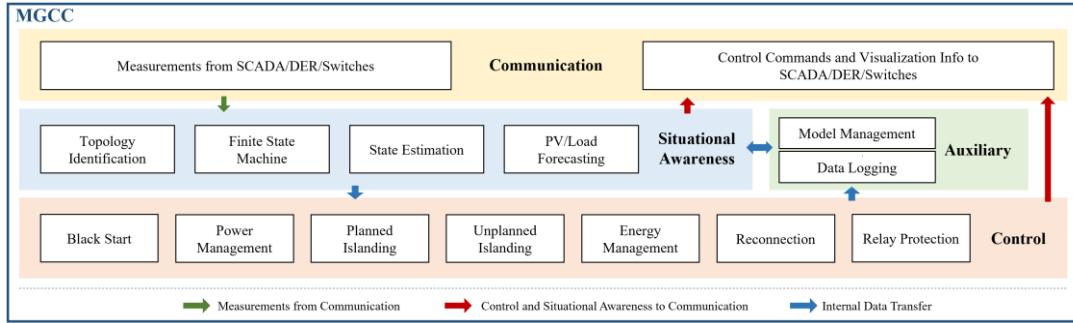


Figure 5-1 Function modules in the microgrid central controller

- interfaces with minimal transients. It also coordinates with the power management module to split a (sub-)MG into multiple sub-MGs when the total generation is insufficient to support the merged operation.
- *Reconnection*. The Reconnection module resynchronizes a (sub-)MG to a grid interface through an available grid interface. It also coordinates with the power management module to merge multiple (sub-)MGs when necessary.

The MGLCs are designed to bridge the MGCC and various commercial DER installations, including PVs, BESSs, backup generators, etc. MGLCs perform local active and reactive power control, signal conversion, data acquisition, and data logging.

The controllers have been implemented on the National Instruments' CompactRIO systems (MGCC on cRIO 9039, MGLC on cRIO 9035), which are controller platforms for prototyping and testing of various engineering systems [74]. Such hardware controller platforms provide precise real-time control capabilities, come in a compact size for quick deployment, and can withstand harsh environments in the field. The compromise, however, is the limited computational resources as compared to professional purpose-built workstations. Considering the computational complexity elicited by the adaptability to arbitrary topologies, the controller algorithms should be designed with efficient algorithms to meet the real-time execution requirement. The benefit from the arbitrary topology capability, on the other hand, is significant – the controller can be deployed at new sites with less time, effort, and reduced cost, compared to traditional controllers designed for specific microgrid sites.

5.3 The Power Management Module

In this section, the structure and algorithms of the power management module will be introduced in detail, including the overall data flow and details about the real-time topology-adaptive load combination algorithm to accommodate multiple source locations and facilitate flexible topological variations and mode transitions.

5.3.1 Structure of the Power Management Module

As a core module of the microgrid controller solution, the power management module is responsible for managing the dynamic boundaries and operation of DERs to balance the active and reactive power in all (sub-)MGs. It also controls PV curtailment/release and initiates the merging/separation process of (sub-)MGs when necessary. An overview of the module is depicted in Figure 5-2, where the solid boxes indicate function blocks in the power management module and the dash boxes indicate function blocks from other modules that coordinate with power management.

- The ‘Topology Awareness and Analysis’ block provides its downstream function blocks with real-time matrices that contain topological information about the controllable areas. In case of fault events, the block will exclude areas locked out for isolating the fault, which helps coordinate the power management with protection systems [104].
- The ‘Merging Initiation’ and ‘Separation Initiation’ blocks monitor the topological and generation/demand information to initiate merging when multiple sub-MGs share boundary switches, or separation when the generation becomes insufficient to support a merged operation. The merging and separation initiation commands

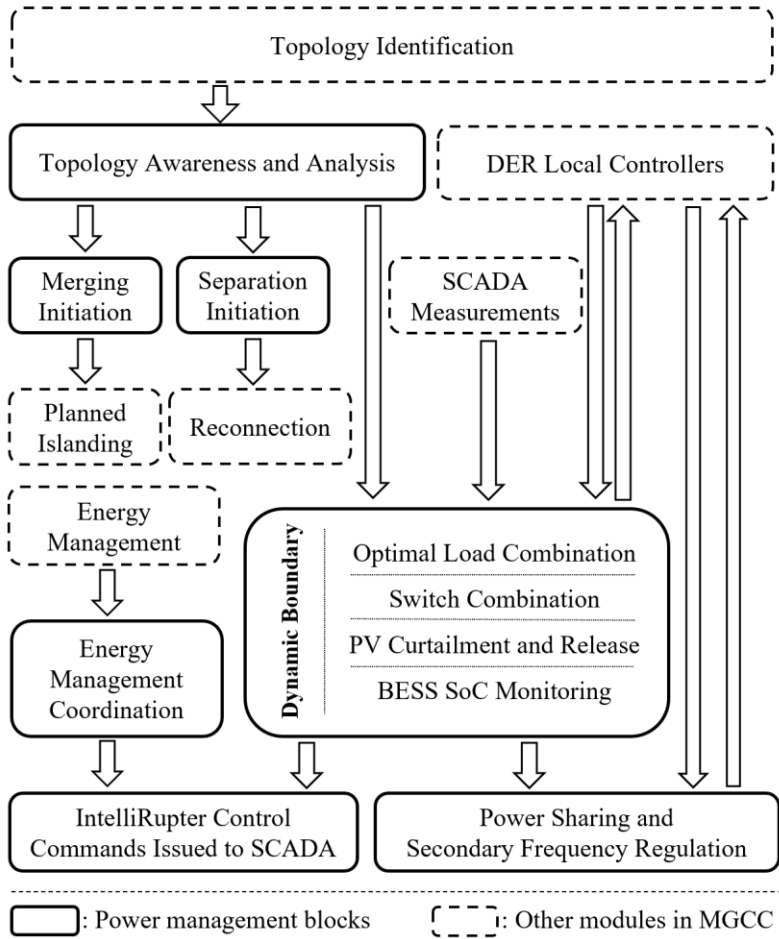


Figure 5-2 Data flow of the power management module

are sent to the Reconnection and Planned Islanding modules, respectively, to implement the process. The Reconnection and Planned Islanding modules were originally designed to synchronize or island from the grid interface. In the latest controller updated for multiple source locations, they have been enhanced with the capability to merge multiple sub-MGs or separate merged (sub-)MGs [105].

- The ‘Dynamic Boundary’ block chooses optimal load combinations for all controllable sub-MGs to balance their active/reactive power by controlling the smart switches and the DERs. The block is triggered by boundary change criteria detailed in section 5.3.2.
- The ‘Energy Management Coordination’ block fetches recommended load (switch) combinations from the Energy Management module based on its long-term optimization plans. When the recommended load (switch) combinations meet the short-term constraints defined in power management, the coordination block overwrites the switch commands from the Dynamic Boundary block to facilitate the long-term energy management goals.
- The Power Sharing and Secondary Frequency Regulation block is introduced to the power management module to a) keep the system frequency at 60 Hz, and b) actively control the sharing of loads across the participating sources in a (sub-)MG. This becomes feasible because of the communication readily available between the central controller and local controllers. The block adjusts the droop settings of various sources participating in frequency regulation based on their topological locations, power capacities, and energy availabilities.

Although the primary frequency control is not listed as a block in the power management module, it is implemented in frequency-responsive DERs either as built-in or in the lower-level local controllers. The power management module introduced in this dissertation, as part of the higher-level central controller, includes only the secondary frequency control in terms of frequency regulation, and the coordination with the primary control is accomplished among the central controller and the local controllers. These function blocks are coordinated in a logic flow shown in Figure 5-3. Details of the algorithms for determining the optimal load/switch combination, power sharing and secondary frequency regulation, PV curtailment, BESS SoC considerations, etc., will be discussed in III.B.

5.3.2 Dynamic Boundary Algorithms for Arbitrary Topologies

Since the controller targets a highly flexible and low-cost solution, the Dynamic Boundary block in the power management module is designed to be adaptable to arbitrary non-mesh topologies. A generalized, topology-adaptive algorithm is highly desirable since: a) The controller can be quickly deployed at new microgrid sites at a lower cost than comparable site-specific designed controllers; b) Capability to handle complex topology changes due to merging and separation of sub-MGs when there are multiple source locations; c) High adaptability in extreme operation conditions where there are topology changes due to a fault, maintenance, etc.

It should be noted that the adaptability of the power management module introduced in this dissertation is limited to non-mesh topologies for two reasons: a). Most of the distribution networks are radial. Even if some of the networks have loop topological structures, they are typically operated under non-mesh topologies to avoid circulating

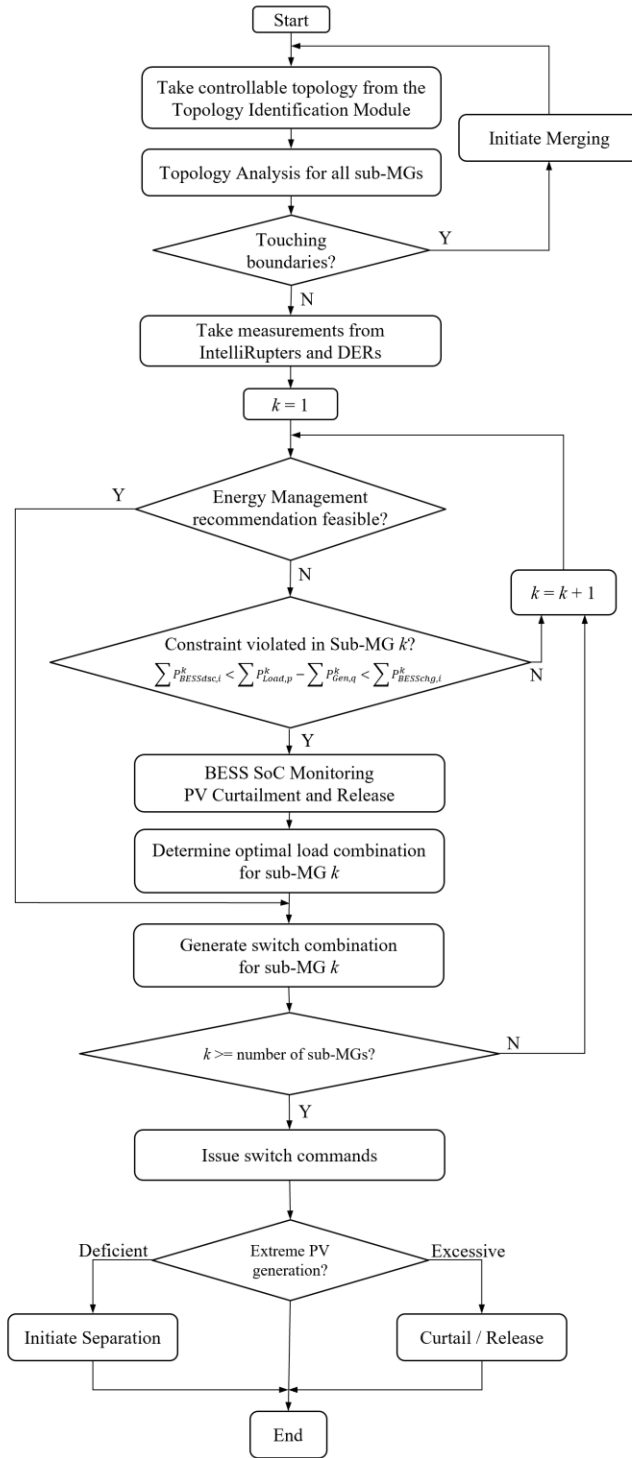


Figure 5-3 Flowchart of the power management module

current and power; b). Designing the function for meshed topologies will greatly increase the complexity of the algorithm, which is unnecessary in most cases and impedes real-time implementation in hardware controllers. For microgrids with a particular need for meshed topologies, a rule-based algorithm can be integrated into the power management as a designated add-on to operate the loop. The loop will be treated as an equivalent node with an interface to the larger adaptively controlled microgrid.

To comprehend arbitrary topologies, the power management module first generates a load combination list that covers all combinations of load sections to be energized. Assuming the total number of non-critical load sections is n , the number of combinations will be 2^n since every load section has a binary status of either picked up or shed offline. However, not all these load combinations are feasible, depending on the real-time topology of the (sub-)MG at the time of decision-making. All switches that connect the load section to a source location have to be closed before the load section can be picked up. For example, in Figure 5-4 (a), the load combination 2-3-4-5-10 is not feasible since load section 10 requires at least load sections 2, 4, and 6 to be energized (corresponding switches to be closed). Figure 5-4 (b) is a possible load combination since all load sections energized have routes to access the source location 1.

While such discretion is natural to human eyes, the controller should be carefully designed to understand arbitrary topologies and rule out infeasible topology variations efficiently considering the limited calculation resources and the real-time requirement. To this end, the shortest route algorithm is implemented as the first step to establishing the mapping between switch combinations and load combinations. This sets a foundation for screening the topological variations and determining the optimal boundaries.

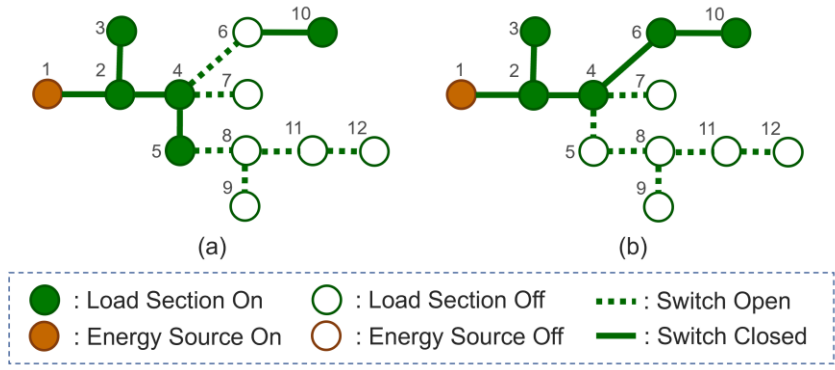


Figure 5-4 Feasibility of load combinations

5.3.2.1 Shortest Route Algorithm

The shortest route algorithm searches for paths from one location to another with linear programming techniques [106], [107]. Applying the shortest route algorithm to find the routes between source locations and load locations allows us to establish the mapping between switch combinations and load combinations. To start with, an input topology matrix from the Topology Identification module is obtained by the power management module for real-time awareness of the controllable area and assets.

The matrix is in the format in Table 5-1, where each row represents a smart switch between the “from” node and “to” node. Property “Type” and “Status” indicate the type of connection (to load, BESS, PV, GEN, etc.), and the “Status” indicates the real-time on/off status if it is a smart switch. The algorithm translates the matrix in Table 5-1 into an incidence matrix as in Figure 5-5, where the numbering of rows represents the nodes, and the numbering of columns represents the switches. The entries in the matrix indicate the direction of the connection in relation to the nodes, with “1” indicating “from” the node, “-1” indicating “to” the node, and “0” indicating no connection to the node.

To find the shortest route in sub-MG k from node i to j , it can be formulated as an optimization problem with the incidence matrix:

$$\mathbf{x}_{ij}^k = \min(f^k) = \min(\mathbf{W}^k \mathbf{x}^k) = \min(w_1^k x_1^k + w_2^k x_2^k + \dots + w_q^k x_q^k) \quad (5-1)$$

such that,

$$\mathbf{A}^k \cdot \mathbf{x}_{ij}^k = \mathbf{b}_{ij}^k \quad (5-2)$$

where \mathbf{W}^k is the weight vector indicating the priority of the switches (and corresponding load sections), \mathbf{A}^k is the incidence matrix of sub-MG k , $\mathbf{x}_{ij}^k = [x_1^k, x_2^k, \dots, x_q^k]$ is the vector

Table 5-1 Format of a topology matrix of a controllable area

From	To	Type	Status
<i>l</i>	<i>2</i>	1-4	0/1
<i>m</i>	<i>n</i>	1-4	0/1
...
<i>2</i>	<i>i</i>	1-4	0/1
<i>j</i>	<i>m</i>	1-4	0/1

$$\mathbf{A} = \begin{matrix} & \begin{matrix} \text{Switch 1} & \text{Switch 2} & & \text{Switch p} & \text{Switch q} \end{matrix} \\ \left[\begin{array}{ccccc} 1 & 0 & \dots & 0 & 0 \\ -1 & 0 & \dots & 1 & 0 \\ \dots & \dots & \dots & \dots & \dots \\ 0 & 1 & \dots & 0 & 1 \\ 0 & -1 & \dots & 0 & 0 \end{array} \right. & \begin{matrix} \text{Node 1} \\ \text{Node 2} \\ \\ \text{Node m} \\ \text{Node n} \end{matrix}
 \end{matrix}$$

Figure 5-5 Incidence matrix identifying connections in the microgrid

consisting of the on/off status of the switches, and $\mathbf{b}_{ij}^k = [0, 0, \dots, b_i^k = 1, 0, \dots, b_j^k = -1, 0, \dots, 0]$ is the constraint vector for the directed path i to j . Setting i to be a source location and j to be a load section allows the algorithm to find the route between the two locations. By applying such a technique to all source locations to all load sections, a complete mapping between the switch combinations and load combinations can be established.

For areas where there are multiple source locations operated as a merged (sub-)MG, the shortest route algorithm is also leveraged to find the path between the source locations. This is to find the switches and load sections on the critical path that connects the source locations. These sections will be prioritized to keep the (sub-)MGs merged for higher reliability and efficiency. For example, the MG in Figure 5-6 has a critical path 1-2-4-5-13 with load sections L2, L4, and L5 on the route. When there are more than two source locations, the algorithm iterates to include them in the critical path. The resulting critical path will be treated as an equivalent node during the merged operation. The power management will maintain the merged operation until the generation available drops to a level where it is insufficient to support all load sections on the path (L2, L4, and L5). In that case, a separation command will be sent to the Planned Islanding function to initiate the separation process, after which the original (sub-)MG will be operated as two separate sub-MGs.

5.3.2.2 Generating Load and Switch Combination List

After applying the shortest route algorithm to all load sections and sources, each load section is designated a specific route that connects it to a source location or an equivalent

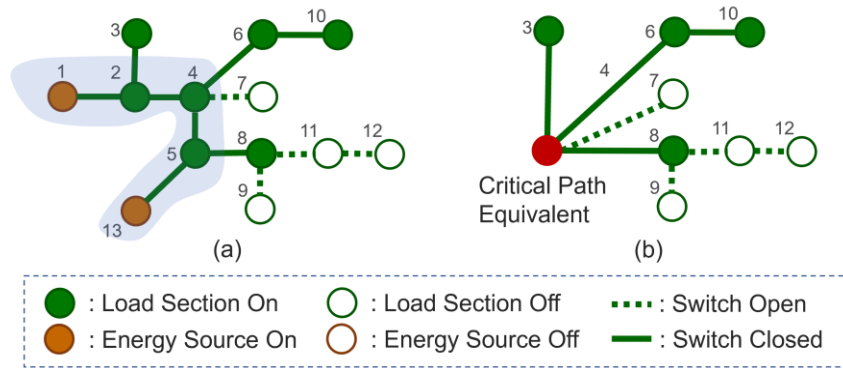


Figure 5-6 Topological treatment for merged (sub-)MGs

node representing a critical path. With such routes available, upstream switches and load sections can be identified for a target load section. The switch combination and load combination list can then be screened to ensure the effective connection of all selected load sections to at least one of the source locations. These load combinations, together with load data (real-time measurement for energized sections and load forecasting from the Energy Management module for de-energized ones), provide the dynamic boundary block with a list of boundary options with estimated active and reactive power demands. The power management further filters out boundary options with active power imbalance larger than a predefined threshold (detailed in the following content), or an unacceptable level of reactive power violating the BESS apparent power thresholds. The remaining boundary options after such a screening process are added to the boundary change candidate list.

5.3.2.3 Boundary Change Trigger and Determination

To reduce unnecessary disturbances to the load sections, the boundary change is only triggered when certain criteria are met. In the controller, the trigger is set to be the active power mismatch between the demands and generation that is being buffered by the BESSs. Violation of the following inequivalent constraints will trigger the boundary change:

$$\sum P_{BESSdsc,i}^k < \sum P_{Load,p}^k - \sum P_{Gen,q}^k < \sum P_{BESSchg,i}^k \quad (5-3)$$

where $P_{BESSdsc,i}^k$ and $P_{BESSchg,i}^k$ are the discharging and charging power thresholds for BESS i in (sub-)MG k . $P_{Load,p}^k$ and $P_{Gen,q}^k$ are load sections and distributed generations in the (sub-)MG. This criterion is being applied to all (sub-)MGs, and it requires real-time power measurements from all BESSs. In cases where there is no DER participating in secondary frequency regulation, the criterion can be further simplified to a formulation that

requires only the measurement of frequency. For (sub-)MG k , the boundary change is triggered when the following is violated:

$$-\frac{1}{\left(\sum_i R_i^{k-1}\right)} \sum_i P_{BESSdsc,i}^k < \Delta f^k < -\frac{1}{\left(\sum_i R_i^{k-1}\right)} \sum_i P_{BESSchg,i}^k \quad (5-4)$$

where the notations used are the same as (3), and R_i^k is the slope reflecting the frequency droop sensitivity for DER i in (sub-)MG k . Reasons why this formulation is not recommended for (sub-)MGs where there are secondary frequency regulations include: 1) the frequency measurement error will have a large impact on the accuracy of the calculation due to the smaller frequency deviation achieved by the secondary frequency regulation; 2) the MGCC will have to collect information about the real-time droop characteristics from all generation sources participating in the secondary frequency regulation.

Once a boundary change is triggered, the controller will choose the switch (load) combination with minimum active power mismatch and no reactive power violations in the feasible boundary candidate list. In cases where the BESSs in the (sub-)MG have extreme SoCs, either near fully charged or fully discharged, the dynamic boundary block will prioritize load combinations that assist in the recovering of SoC to a normal range.

Other considerations the power management takes when determining the boundary include the coordination with the Energy Management module and microgrid protection systems. When the boundary candidate recommended by the Energy Management module falls within the feasible boundary change list, the power management module will prioritize the one recommended to facilitate the long-term goal of the Energy Management module. The adopted boundary will be maintained until it violates the short-term constraint, equation (5-3), because of variations in generation and demand during operation.

The coordination with microgrid protection systems, on the other hand, is accomplished through the Topology Identification module. Once the microgrid protection system detects a fault, it will send a lockout signal to the Topology Identification. The Topology Identification module will automatically exclude the switches being locked out due to the fault. With the updated real-time topology matrices, the power management will temporarily withhold its control over the affected switches to prioritize the actions from the protection system until the fault is removed.

5.3.3 Power Sharing and Secondary Frequency Regulation

Although the majority of the power imbalance is significantly reduced by changing the (sub-)MG boundaries, a minor power mismatch may still remain between the generation and demand. Such a mismatch will create a frequency deviation from 60 Hz because of the droop characteristics of the primary frequency response implemented in the local controllers or as built-in functionalities in the internal control system of the DERs. Secondary frequency regulation function is necessary to bring the system frequency back to 60 Hz by coordinating the primary frequency response characteristics in frequency-responsive DERs. It is noted that the power sharing and secondary frequency response function in this power management module inherits the built-in adaptability and flexibility to the variations in topology and operating conditions. Since the BESSs are the frequency regulating sources, in this case, the secondary frequency regulation signals are distributed to them to move their droop curves up/down in a coordinated manner. This enables not only the frequency regulation but also active control of load sharing among the participating BESSs at the same time.

Figure 5-7 shows a group of power-frequency droop curves that can be used in a frequency-responding BESS i in sub-MG k . They can be described as in (5-5) with different power references.

$$f^k - f_0 = R_i^k (P_i^k - P_{ref,i}^k) \quad (5-5)$$

where f^k is the frequency of (sub-)MG k , f_0 the nominal frequency (60 Hz), R_i^k the droop slope, and $P_{ref,i}^k$ the power reference point of BESS i in (sub-)MG k .

Suppose the curve crossing $P_{ref,i}^k$ in Fig. 7 is the original power reference, moving it up to $P_{ref,i}^{k''}$ or down to $P_{ref,i}^{k'}$ will increase or decrease the load sharing of the BESS, respectively. In a (sub-)MG, the following equations and constraints shall be satisfied at all times:

$$\left\{ \begin{array}{l} f^k - f_0 = R_1^k (P_1^k - P_{ref,1}^k) \\ \vdots \\ f^k - f_0 = R_i^k (P_i^k - P_{ref,i}^k) \\ \vdots \\ f^k - f_0 = R_n^k (P_n^k - P_{ref,n}^k) \\ P_{ref,1}^k + \dots + P_{ref,n}^k = \sum P_{Load,p}^k - \sum P_{Gen,q}^k \\ f_0 = 60 \text{ Hz} \\ P_{BESSdsc,i}^k < P_{ref,i}^k < P_{BESSchg,i}^k \end{array} \right. \quad (5-6)$$

where f^k , R_i^k , P_i^k , $P_{ref,i}^k$, $P_{BESSdsc,i}^k$, $P_{BESSchg,i}^k$ are nominal frequency of sub-MG k , the droop slope, power output, power reference point, discharging and charging power limit of BESS i in sub-MG k ; $P_{Load,p}^k$ and $P_{Gen,q}^k$ represent the power demand of load sections and generation of non-frequency-responsive DERs in sub-MG k . To dispatch the frequency-responsive BESSs' loading based on their ratings, the power reference points of the frequency-responding BESSs can be determined by minimizing the following objective function through simple linear optimization:

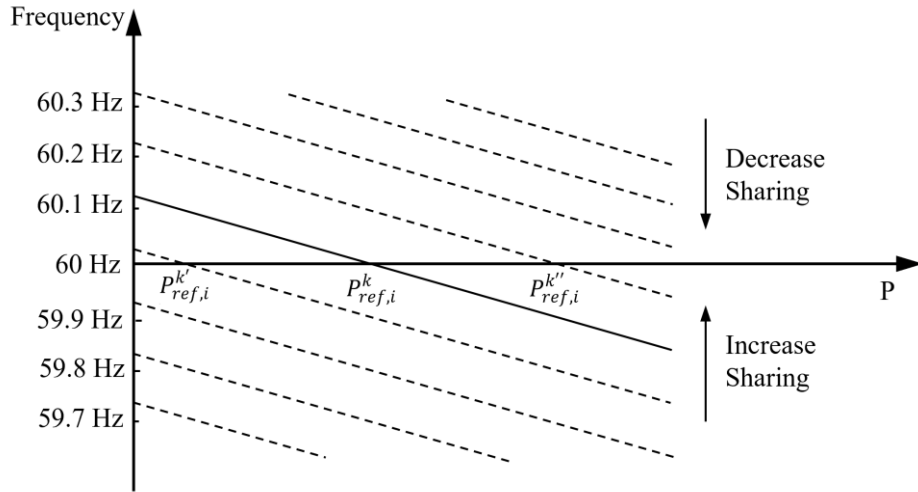


Figure 5-7 A group of P-f droop curves

$$\min F = \sum_i \left(P_i^k - \frac{P_{max,i}^k}{\sum P_{max,i}^k} \left(\sum_p P_{Load,p}^k - \sum_q P_{Gen,q}^k \right) \right) \quad (5-7)$$

where $P_{max,i}^k$ equals either $P_{BESSdsc,i}^k$ when demand exceeds generation, or $P_{BESSchg,i}^k$ vice versa. The power management in MGCC periodically executes the power sharing and secondary frequency regulation block and distributes the updated droop curve parameters to MGLCs. As a result, the frequency responding BESSs will share the loading in proportion to their power ratings, as long as their outputs are within rated capacities, and they collectively compensate the total power mismatch required to maintain the (sub-)MG frequency at close to 60 Hz.

5.3.4 Extreme Power Imbalance Conditions

In addition to the power sharing and secondary frequency regulation functions above, the power management module has built-in functions to handle extreme conditions, including PV curtailment and release, separation initiation, and SOC emergency control.

When all sub-MGs have expanded to their maximum boundaries and all mergeable sub-MGs have been merged, the microgrid will no longer be able to expand its boundaries to accommodate a further increase in irradiance. If not properly controlled, the over-current protection in BESSs may be triggered as a built-in protection mechanism to avoid asset damage. Hence, the power management module will activate the PV curtailment function to temporarily reduce the charging power and prevent the BESSs from tripping themselves in such extreme conditions. The amount of PV generation curtailed is:

$$C_{PV}^k = \frac{P_{PV-f}^k - \sum P_{Load,p}^k + \sum P_{Gen,q}^k}{P_{PV-f}^k} \quad (5-8)$$

where C_{PV}^k is the amount of curtailment in percentage for PV generation units in sub-MG

k , P_{PV-f}^k is the full PV generation potential if not curtailed in sub-MG k , $\sum P_{Load,p}^k$ and $\sum P_{Gen,q}^k$ are the total load and total generation (except PV) in sub-MG k . The reason why the PV curtailment is designed to bring the BESS output to zero, instead of the maximum allowable BESS charging power, is that PV curtailment often happens when the solar generation ramps up rather quickly, and thus, the BESS should have enough safety margin under such extreme conditions. The power management, being a short-term balancing module, prioritizes the safe operation of the equipment and prevents BESS and other resources from tripping themselves under extreme conditions. Under normal operation, though, the power management will take recommendations from the Energy Management module to facilitate long-term goals, including desirable BESS SoCs. The curtailment will be released when the PV generation decreases to an acceptable level for the BESSs.

On the contrary, when the PV generation becomes too low to support a merged island on its minimum boundary, the power management will initiate the separation process to shed more load sections (those on the critical route that connects multiple source locations). The separation-related information about the relevant source locations, source types, and critical routes will be shared with the Planned Islanding module to complete the separation process. Details about the separation process can be found in the paper [105].

5.4 Testing Platform and Results

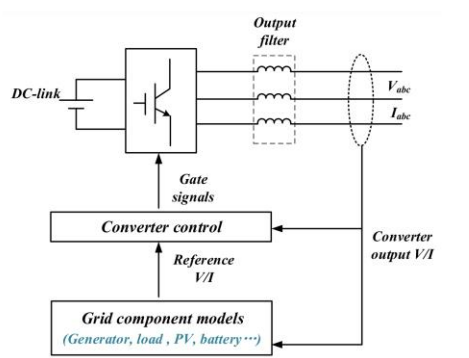
5.4.1 Converter-based Hardware Testbed (HTB)

The MGCC and MGLCs are implemented on NI's real-time controller system, CompactRIO. Debugging and validation of the controllers are conducted on a converter-based hardware testbed (HTB). The HTB is comprised of a number of converters that are

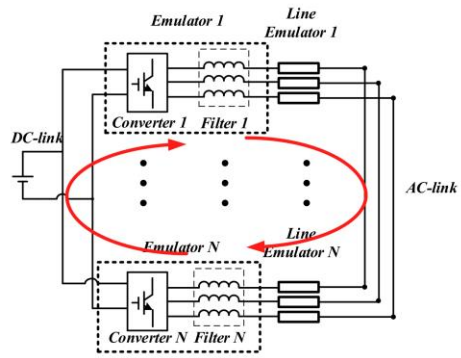
used to emulate various components, including generators, BESSs, PV systems, and loads (Figure 5-8 (a)). All converters share the DC link, and the connection on their AC side can be configured as needed to represent the power network the HTB attempts to emulate (Figure 5-8 (b)). The power flow in the HTB circulates through the DC link, generation emulating converters, AC link, load emulating converters, and back to the DC link. A picture of the HTB cabinets and the structure of the HTB testing platform are shown in Figure 5-9.

By design, the HTB provides real current, voltage, and power in the hardware testing setup to mimic a real-world operation environment including measurement errors and physical communication networks. More details can be found in references [108-111]. This opens opportunities for not only the validation of control functions but also the measurement and communication systems. The testing results obtained in the testing are collected with hardware current/voltage sensors placed on terminals on the converters that emulate the generators, BESSs, PV, and loads. The data are transferred to the microgrid controllers where they are logged and stored for extraction and analysis. Oscilloscope probes are also placed on critical points on the HTB to monitor and log the current and voltage waveforms.

The testing microgrid emulated on the HTB is a modified model based on the EPB microgrid at Chattanooga Airport, as shown in Figure 5-10. The main modification is the addition of a second source location to mimic potential multiple source developments, which requires the microgrid controllers to handle multiple sub-MGs and the associated topological variations/operations. The power base of the testing microgrid is 1 MW. The voltage base is 12.47 kV on the medium voltage side and 480 V on the low voltage side.



(a) Structure of a converter in the HTB



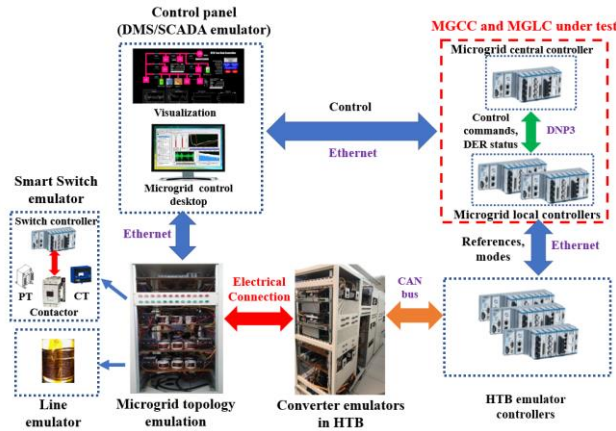
(b) Connection of converters in the HTB

Figure 5-8 Structure of the converter-based hardware testbed (HTB) [110]



(a) Converter-based HTB cabinets

Figure 5-9 Converter-based HTB testing platform



(b) Structure of the converter-based HTB testing platform

Figure 5-9 Continued

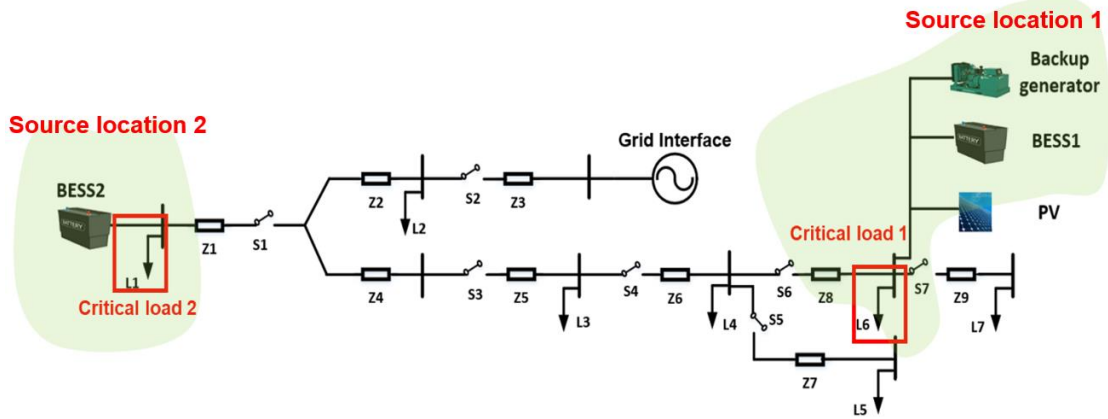


Figure 5-10 HTB microgrid circuit model

Source location 1 in Figure 5-10 is the existing source location in the EPB microgrid, where there is a BESS system of 510 kWh/560 kW, a PV farm of 2 MW, and a backup generator of 423 kW. Source location 2 has initially been a grid interface and is now modified to be the second source location with another BESS system of 510 kWh/560 kW. Load sections L1 and L6 are critical load sections with a size of 50 kW each and are accompanied by the DERs. Load sections L2, L3, L4, L5, and L7 are load sections of lower priorities that can be picked up or shed offline during islanded operation. The sizes of L2, L3, L4, L5, and L7 are 150kW, 150kW, 150kW, 100kW, 100kW. The parameters are downscaled accordingly based on the ratings of the converters in the HTB platform, where the DC link voltage is 200 V for each converter, the AC voltage base is 100 V, and the AC power base is 1.732 kW.

Note that, while the generation sources in this testing setup are consistent with those in the field of the Chattanooga Airport microgrid, the topology and the PV generation profile used in this testing have been altered to create as many operating scenario variations as possible within the capability of the converter-based hardware testbed. The boundary change trigger thresholds based on BESS charging and discharging power, as defined in equation (3), are also intentionally set to a lower level (± 200 kW) compared to the capacity to create operation scenarios of various boundary changes and operation transitions. These modifications enable comprehensive activation and validation of the functionalities of the power management module. The actual design of the microgrid in the field, however, is an overarching effort that covers all subsystems, including recloser placement, resource sizing, grounding system, and protection system design, to achieve a balance between cost and reliability. We have had publications and are preparing a dedicated manuscript

regarding the design topic to address specific concerns and opportunities in microgrid design arising from multiple-source-location dynamic-boundary microgrids [95], [103].

A graphical user interface has been developed to show the real-time status and measurement in the converter-based HTB on a desktop for monitoring and operation purposes, as shown in Figure 5-11. The visualization presents load sections, lines, switches, and sources with blocks and bars that change their colors to indicate their operation status. There are also LED indicators and buttons for the status and initiation/termination of function modules in the MGCC and MGLCs. At the bottom of the visualization are scopes that plot real-time voltage, power, and frequency measurements collected from the sensors in the converter-based HTB. The testing results are recorded by the data logging module in the controllers, and oscilloscope probes are connected to the converters for the real voltage and current waveforms in the testing platform.

5.4.2 Testing Scenarios and Results

To cover various operating conditions in the field, the test case was designed to have the PV generation ramp up and down to trigger actions from the power management module. The test case started with two separate sub-MGs and proceeded through boundary expansion, merging, PV curtailment and release, boundary shrinking, and separation.

Figure 5-12 shows a simplified representation of the initial topology of the MG with critical loads at locations 1 and 6. Critical load section L1 is accompanied by BESS-2 at location 12, and critical load section L6 is accompanied by BESS-1 at location 9, PV at location 10, and backup generator at location 11.

The designed testing scenario was driven by variations in the PV generation, which can be divided into a few stages as shown in Figure 5-13.

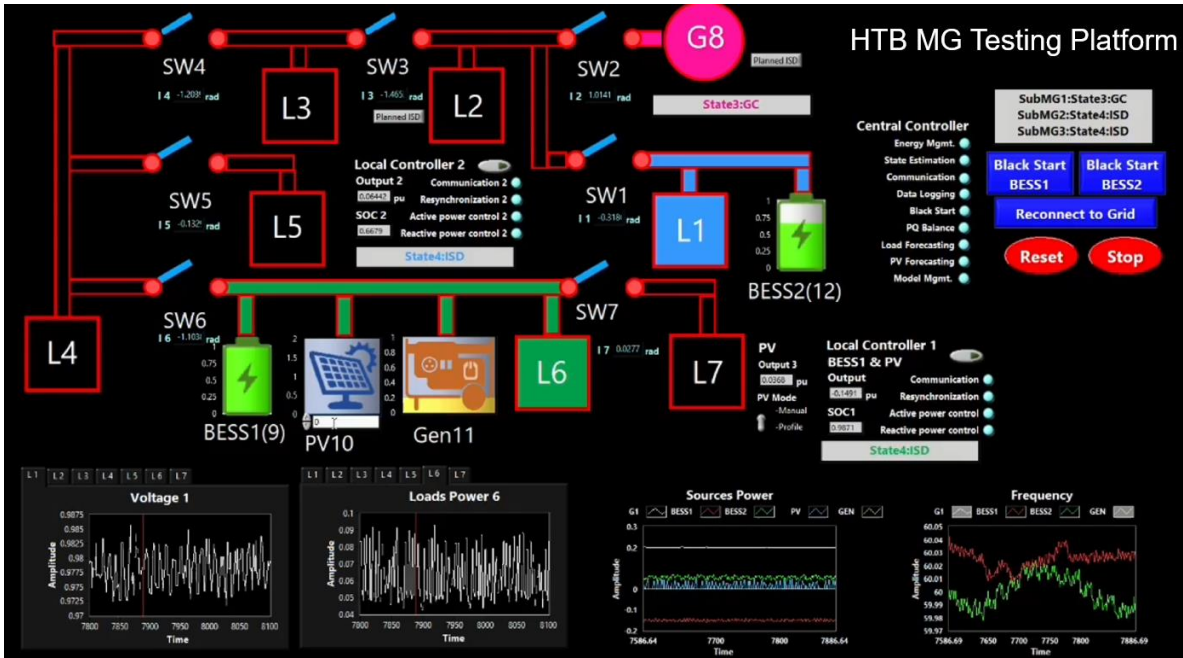
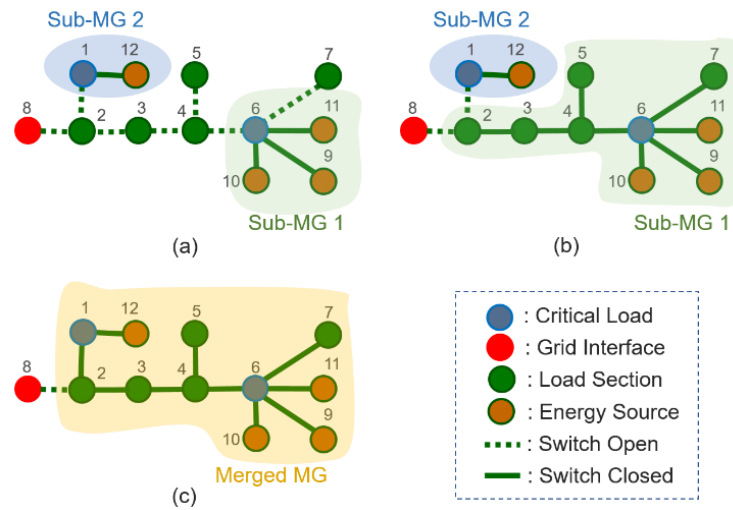


Figure 5-11 Visualization interface of the HTB microgrid testing platform



(a) Initial topology after black start; (b) Topology before merging; (c) Merged microgrid.

Figure 5-12 Topology variations of the MG

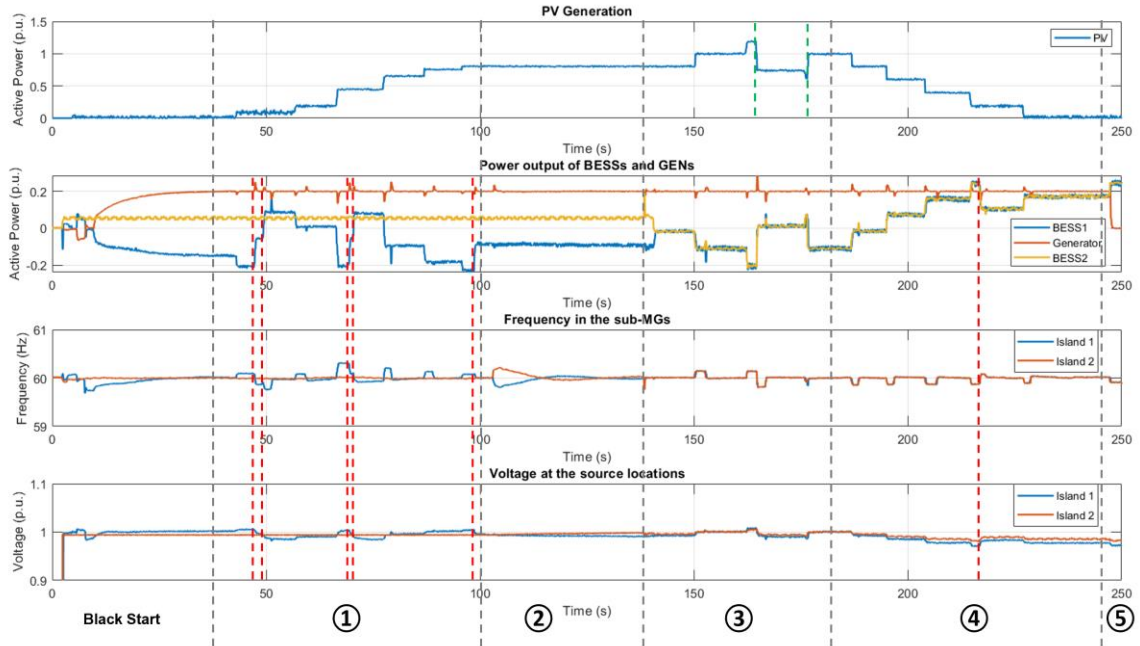


Figure 5-13 Power, frequency, and voltage during the HTB testing

Stage 1: Operation of separate sub-MGs – Boundary Expansion. After a black start, the MG is operated as two sub-MGs with minimum boundaries, where only the critical load L1 in sub-MG 2 and critical load L6 in sub-MG 1 are served. As the PV generation in sub-MG 1 ramps up, the BESS charging power equation (5-3) reaches 210 kW at $t = 43$ s (Figure 5-13), which is larger than the boundary change trigger threshold $\sum P_{BESSchg,1}^1$ of 200 kW. The power management takes the real-time topology matrices and determines the optimal boundary to include load sections L4 and L5 to lower the power imbalance. Hence, the commands are issued through communication to close switches S6 and S5 to expand the boundary of sub-MG 1. The PV generation continues to climb quickly and pushes more power into BESS 1. At $t = 67$ s, the total BESS charging power reaches 205 kW, which is larger than $\sum P_{BESSchg,i}^1 = 200$ kW. It triggers another round of boundary change that leads to the pickup of load sections L3 and L7 at $t = 69$ s. L2 is picked up at $t = 98$ s as a response to the BESS charging power trigger threshold being crossed at $t = 96$ s. Figure 5-14 shows the voltage and current waveforms captured by the oscilloscope during the boundary expansion of sub-MG 1. The green waveform is the current of the BESS 1, and the blue is that of the PV. Each time the PV power ramps up, the PV current increases and pushes more power into the BESS1. When the power intake of BESS1 reaches the threshold, the power management module issues commands to pick up additional load sections in sub-MG 1 in order to reduce the power imbalance absorbed by the BESS, as indicated by the reduced BESS current (the green waveform) magnitude.

Stage 2: Merging. As a result of the expansion of sub-MG 1, the boundaries of the two sub-MGs reach each other at smart switch S1. The power management module detects

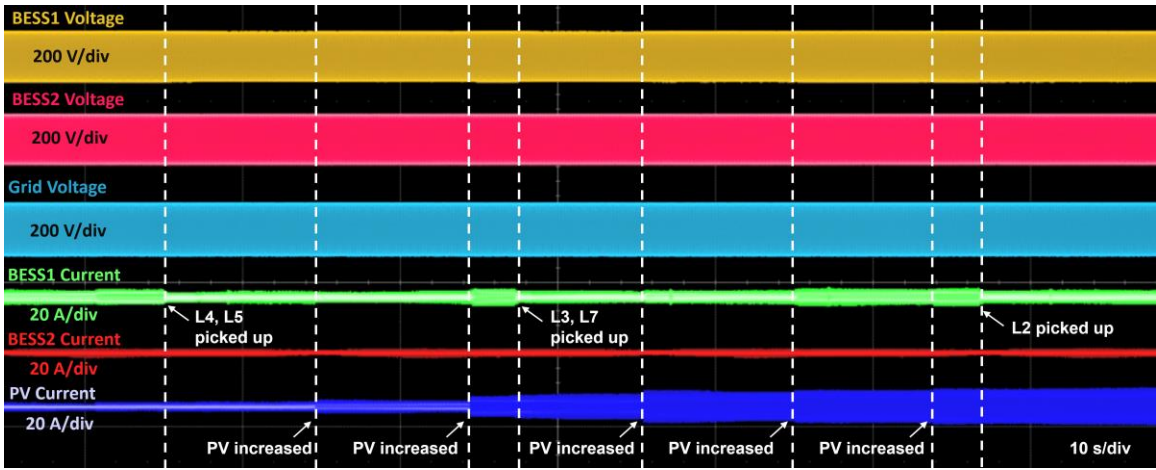


Figure 5-14 Voltage and current waveforms during the boundary expansion

the bordering boundaries and issues commands to the Reconnection module at $t = 103$ s to initiate the merging process on S1. The Reconnection module actively adjusts the frequency and voltage of the two sub-MGs to synchronize the voltages on the two sides of S1 until it can be closed with a minimal angle and magnitude difference. This can be observed by the weaving frequency curves of the two sub-MGs starting from $t = 103$ s, which indicates that the sub-MGs are adjusting their frequencies to synchronize the two islands. The merging process was completed at $t = 139$ s (36 s elapsed time).

Stage 3: Operation of merged sub-MGs – PV curtailment and release. The merged MG is operated as a single MG and the topology is handled as discussed in section 5.3.2. After the merging, the critical path connecting the source locations of the two sub-MGs, 1-2-3-4-6, will be treated as an equivalent node, of which the concept was explained in Figure 5-6. As the PV continues to increase and the BESS power intake exceeds the total charging power threshold $\sum P_{BESSchg,i}^{merged} = 400$ kW at $t = 163$ s, the MGCC curtails the PV output at $t = 165$ s since the microgrid has reached the maximum electric boundary available. The percentage of curtailment is calculated with equation (8), which gives a result of $C_{PV}^{merged} = 38.33\%$. The PV curtailment persisted for 12 seconds, as indicated by the two green dashed lines in the PV active power output plot in Figure 5-13. The dip in PV power output at $t = 176$ s (the second green dashed line in the PV power plot) is a result of a decrease in PV irradiance. The PV active power output, however, ramps up immediately after the dip, at $t = 177$ s. This is the power management releasing the PV curtailment ($C_{PV}^{merged} = 0\%$) because the reduced irradiance led to an acceptable level of PV generation for the BESSs (total charging power of 350 kW, less than the total threshold

$\sum P_{BESSch,i}^{merged} = 400 \text{ kW}$). The power management prioritizes full utilization of PV generation whenever it is safe for the operation of other microgrid assets. Figure 5-15, with the explanatory labels and texts, shows the voltage and current waveforms captured during the PV curtailment and release process described above.

Stage 4: Operation of merged sub-MGs – boundary shrinking. After the release of PV curtailment at $t = 177 \text{ s}$, the PV generation continues the reduction to enable the testing of boundary shrinking and island separation. At $t = 215 \text{ s}$ the total BESS power output in the island, 505 kW, exceeds the discharging threshold $\sum P_{BESSdsc,i}^{merged} = 400 \text{ kW}$. Since the two sub-MGs are operated as a merged island, the MGCC prioritizes the service to load sections L2, L3, and L4 on the critical path 1-2-3-4-6. To reduce the BESS active power output, the power management shrinks the boundary by shedding load sections outside the critical path, L5 and L7 as indicated by the red dashed lines at $t = 217 \text{ s}$ in Figure 5-13.

Stage 5: Separation Initiation. To mimic scenarios where the DER generation falls to a level that cannot support the minimum load sections required to sustain the critical path (in this case, L2, L3, L4), the backup generator was manually shut off after the PV generation fell to zero. This created an insufficiency in the generation, and the total BESS discharging power (490 kW) exceeded the merged island's boundary change trigger threshold $\sum P_{BESSdsc,i}^{merged} = 400 \text{ kW}$. The separation initiation block in the power management module hence sends the separation initiation command, along with relevant energy source information to the Planned Islanding module for further separation actions [105].

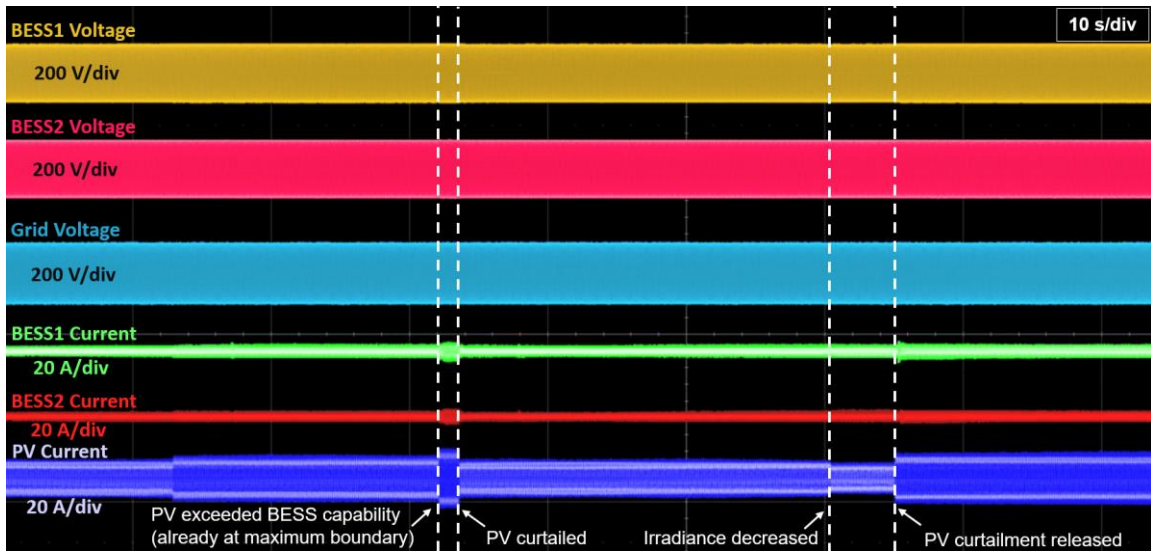


Figure 5-15. Voltage and current waveforms during the PV curtailment

The maximum frequency deviation during the whole test happened at $t = 77.8$ s with $f = 60.30$ Hz when the two sub-MGs were operated separately, and the system frequency was more sensitive to disturbances because of smaller generation source capacities. The maximum frequency deviation is determined by the boundary change trigger threshold and the droop slopes, which can be adjusted to meet the conditions and requirements of specific sources and application sites.

It should be noted that the power sharing and frequency regulation block actively controls the sharing of power among participating DERs and regulates the frequency of the sub-MGs (or the merged MG) throughout the testing at a predefined time interval (every two seconds in the test cases). While in operation as two separate sub-MGs, the power sharing and frequency regulation block recognizes two individual groups of resources and regulates the frequency and power sharing in each island. When the sub-MGs are merged as one island, the power sharing and frequency regulation block regroups the frequency-responsive resources and executes regulations on all resources available in the merged MG.

Take the merged operation for example, as shown in Figure 5-16. The PV generation dropped three times consecutively, at $t = 187$ s, $t = 195$ s, and $t = 204$ s, with 0.2 p.u. (200 kW) in magnitude each time. Since the two source locations are merged as one island, the impact of such a decrease is not as significant because the power deficiency was shared by the two BESSs, and thus no boundary change was triggered. Each 0.2 p.u. (200 kW) of power change led to a dip in frequency of ~ 0.15 Hz, but the frequency was quickly brought back to 60 Hz as the secondary frequency regulation issued commands to MGLCs to adjust the droop curves. This, at the same time, also controlled the load sharing among the two BESSs according to their power ratings.

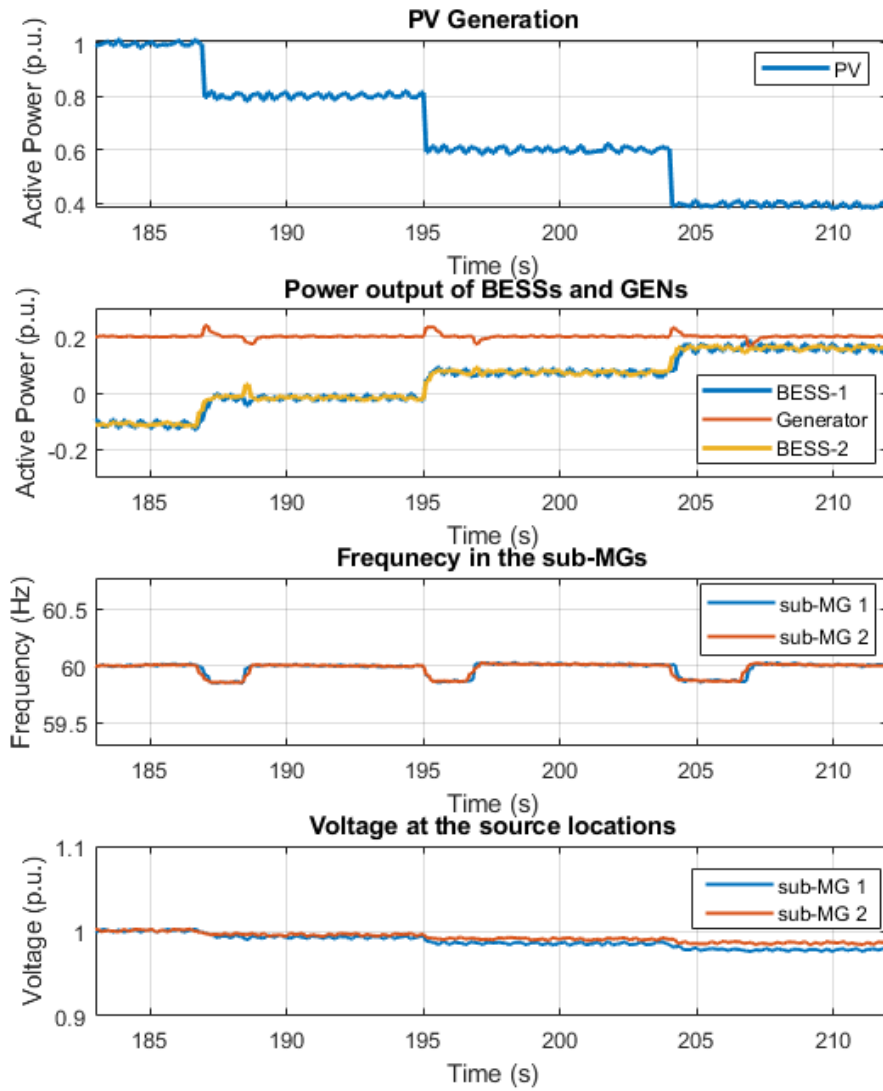


Figure 5-16. Power sharing and secondary frequency regulation

In the HTB testing, the controller reacted as desired to the PV generation change that triggered a comprehensive set of operating conditions and transitions, including the boundary expansion, merging of sub-MGs, PV curtailment, PV curtailment release, boundary shrinking, and separation of sub-MGs. The controller maintained its situational awareness by automatically monitoring the topology of all sub-MGs. In addition to the automatic management of electric boundaries for multiple sub-MGs (or merged sub-MGs), the controller also automatically coordinated DERs in every sub-MG (merged sub-MGs) to regulate the island frequency. Instead of being hardcoded for a specific microgrid topology, the controller is designed to automatically adapt to arbitrary non-mesh topologies in real-time operations, which also makes the deployment of the controller at new microgrid sites fast and efficient with a lower cost due to the enhanced flexibility.

5.5 Summary

The power management module, with real-time measurement feedback and smart switching devices, handles complex topology variations and operation scenarios associated with dynamic boundaries and multiple source locations. It automatically adapts to arbitrary non-mesh topologies so that the deployment process at new microgrid sites can be accelerated with reduced effort and cost. The built-in flexibility in algorithms allows a high degree of topological awareness, simultaneous operation of multiple sub-MGs, and automatic initiation of merging/separation of (sub-)MGs under varying operation conditions and topological changes. The module manages the dynamic boundaries for all (sub-)MGs based on the real-time active and reactive power generation/demand within the islands. In addition, a power sharing and secondary frequency regulation block has been integrated into the module. It adaptively groups and coordinates DERs based on the real-

time topology and minimizes the system frequency deviations for each (sub-)MG. At the same time, it proactively distributes the loading across the participating sources within the corresponding (sub-)MGs in accordance with their ratings.

The controller described in this dissertation has been tested on a converter-based power-in-the-loop testing setup. The controller automatically adjusted the boundaries of islands according to the variations in the microgrid. In cases where the renewable generation is beyond what the dynamic boundaries can accommodate, the controller automatically activated resource curtailment to assure safe operation. System frequency in each island is maintained at 60 Hz throughout the operation despite topology changes and the varying generation/demand mismatch. The controller has also been deployed at a community microgrid operated by EPB near the Chattanooga, TN airport [103]. The controller continues to improve and cover more emerging needs from the field application, such as load imbalance monitoring and control, proactive reactive power balancing through switching capacitor banks, and coordination with utility SCADA/DMS and existing protection schemes.

CHAPTER 6. CONCLUSIONS AND FUTURE WORK

6.1 Conclusions

It is important to leverage the increasingly available measurements and communication facilities for enhanced monitoring and control as power systems around the world are experiencing changes in their generation mixes. This dissertation focuses on using real-time and historical power system measurement data, together with newly available inverter-based resources, for monitoring system dynamics and improving control schemes. A detailed list of contributions of this dissertation is as follows:

- Trending analysis for the inertial response and primary frequency response has been conducted for the Eastern Interconnection from 2012 to 2021. An event filtering method is proposed to improve the accuracy and consistency of the evaluation of frequency response across the years. The analysis reveals a decrease in inertia of at least 10% and an unexpected increase in the primary frequency response, for which an explanation is provided based on the large-scale replacement of coal-fired generators with gas-fired units.
- The correlations between the observed primary frequency response (β) and two factors, the event starting frequency and MW size, are analyzed through curve fitting. The correlation is then used for the formulation of an improved event MW size estimation strategy using the Newton-Raphson method as its solver. The proposed estimation method improved the estimation accuracy by 31%.
- Regional frequency dynamics are analyzed for a variety of areas within the Eastern Interconnection. The Upper Midwest region is most prone to insufficient local

inertial response (2% of the interconnection inertia) and the Florida area is most prone to post-event oscillations. Local RoCoFs can be close to resource RoCoF protection triggers in inertia-deficient areas, but the frequency nadir is kept safe from the under-frequency load shedding setting of 59.50 Hz (59.70 Hz in Florida) because of the inter-area inertial support that arrives within 2 seconds.

- A measurement-based wide-area oscillation damping controller is designed for the Continental Europe Synchronous Area power interconnection, which is faced with oscillation challenges as the renewable integration accelerates in the system, especially during midnights with a light load and high renewable generation. A low-order transfer function is used for modeling the latest system dynamics with minimal reliance on accurate system parameters. The controller is implemented on hardware and the 2000-bus CESA model is implemented on a real-time simulator for HIL testing. The controller successfully changed the negatively damped oscillation mode to have a 12% damping ratio in the base test case, and its performance withstood a variety of communication uncertainties thanks to the adaptive delay compensator and supervisory modules.
- A measurement-based frequency and voltage control scheme is designed for the New York State Grid taking advantage of existing and planned inverter-based resources. The frequency controller is able to accurately estimate area power mismatches with measurement feedback from the IBRs and tie-line powers. The controller is able to prioritize local IBR resources to recover system frequency while maintaining the ability to mobilize inter-area support. The voltage controller flexibly coordinates the IBRs with traditional resources like generators and SVCs.

Both controls are verified through hardware-in-the-loop testing where the 5000-bus New York State Grid is modeled on a real-time simulator. The frequency controller accurately recovered system frequency to the nominal within 1 second when only local response is leveraged and 4 seconds when inter-area support is mobilized. The voltage control successfully coordinated difference resources according to the given priority and contained the voltage deviation within the pre-defined limits of (0.95, 1.05) on all load buses.

- A measurement-based power management module for multiple-source-location dynamic-boundary microgrids is designed to take advantage of the IBR development on distribution levels for more flexible and efficient operations. The module manages in real-time the dynamic boundaries, the merging and separation of multiple islands, and the frequency regulation based on the measurement feedback from SCADA and generation resources. All algorithms within the module (and the controller) are designed to be automatically adaptable to arbitrary non-mesh topologies. This not only enables the controller to handle complicated topological variations brought by the existence of multiple source locations but also significantly expedites the deployment process of the controller at a new microgrid site and lowers the deployment cost thanks to its built-in adaptability. The proposed power management module, as part of the flexible, low-cost controller, has been implemented on hardware and tested on a hardware/power-in-the-loop testing platform, the hardware-testbed (HTB) at UT-Knoxville, as well as a field community microgrid operated by EPB near the Chattanooga Airport. The module successfully optimizes the dynamic boundaries for the microgrid islands, enables

resource curtailment as necessary, maintains island frequencies despite topology changes and generation/demand variations, and migrated flexibly among different microgrids with reduced effort.

6.2 Future work

While the mild inertia decline is not yet an immediate threat to the Eastern Interconnection, regional inertia can be a more imminent challenge for power system operations since renewable integrations are often uneven across a power interconnection. As discussed in this dissertation, some areas may experience more severe local frequency dynamics due to their nature of generation mix and diversity in connections to the rest of the system.

Developing accurate measurement-based regional inertia monitoring methods could significantly improve system operators' awareness of the safety margins that are specific to the regions and be informative for system planners in future planning decisions. While there have been theoretical investigations about ambient measurement-based and probing-based regional inertia estimation, efforts are needed for effective regional inertia estimation methods in real-world large-scale power systems. This includes the appropriate definition of a region in not only the geological sense, but also in the administrative and electrical sense, the choice and measurements needed in terms of locations and measurement types, the inertia identification algorithms, and data pre-processing strategies.

In addition to regional inertia estimation, it is also important to further investigate the impact of fast frequency response on interconnection-level frequency recovery and stability. Whereas leveraging IBRs in inertia-deficient areas for fast response could be beneficial to mitigating local dynamics, the interaction of such injection with the rest of

the interconnection has yet to be further studied. Specifically, the location of the power disturbance, the location of the responding sources, the interaction with existing oscillation modes, as well as the delay caused by network uncertainties need to be considered in the assessment of the performance and stability of regional fast response strategies. In addition, the coordination of the fast-acting IBRs and traditional frequency response schemes (inertial, primary, secondary, and tertiary) needs to be investigated before these controls can be safely deployed in the field.

REFERENCES

- [1] "Electricity data browser." U.S. Energy Information Administration. <https://www.eia.gov/electricity/data/browser/> (accessed July 26, 2022, 2022).
- [2] L. Zhu, S. You, H. Yin, Y. Zhao, F. Li, W. Yao, C. O. Reilley, W. Yu, C. Zeng, X. Deng, Y. Zhao, Y. Cui, Y. Zhang, and Y. Liu, "FNET/GridEye: a tool for situational awareness of large power interconnection grids," in *Proc. 2020 IEEE PES Innovative Smart Grid Technologies Europe (ISGT-Europe)*, The Hague, Netherlands, 2020, pp. 379-383.
- [3] Q. Bin, C. Ling, V. Centeno, D. Xuzhu, and L. Yilu, "Internet based frequency monitoring network (FNET)," in *Proc. 2001 IEEE Power Engineering Society Winter Meeting. Conference Proceedings*, Columbus, OH, USA, 2001, vol. 3, pp. 1166-1171 vol.3.
- [4] "Oscillation event 03.12.2017," European Network of Transmission System Operators for Electricity (ENTSOE). [Online]. Available: <https://www.entsoe.eu/publications/system-operations-reports>
- [5] M. R. Younis and R. Iravani, "Wide-area damping control for inter-area oscillations: a comprehensive review," in *Proc. 2013 IEEE Electrical Power & Energy Conference*, Halifax, NS, Canada, 2013, pp. 1-6.
- [6] L. Zhu, Y. Zhao, Y. Liu, E. Farantatos, M. Patel, P. Dattaray, D. Ramasubramanian, L. Michi, E. Carlini, G. Giannuzzi, and R. Zaottini, "Oscillation damping controller design using ringdown measurements for the Italian power grid," in *Proc. 2019 IEEE Milan PowerTech*, Milan, Italy, 2019, pp. 1-6.
- [7] E. Ekomwenrenren, Z. Tang, J. W. Simpson-Porco, E. Farantatos, M. Patel, and H. Hooshyar, "Hierarchical coordinated fast frequency control using inverter-based resources," *IEEE Transactions on Power Systems*, vol. 36, no. 6, pp. 4992-5005, 2021.
- [8] Z. Tang, E. Ekomwenrenren, J. W. Simpson-Porco, E. Farantatos, M. Patel, and H. Hooshyar, "Measurement-based fast coordinated voltage control for transmission grids," *IEEE Transactions on Power Systems*, vol. 36, no. 4, pp. 3416-3429, 2021.
- [9] X. Hu, T. Liu, C. He, Y. Ma, Y. Su, H. Yin, F. Wang, L. M. Tolbert, S. Wang, and Y. Liu, "Real-time power management technique for microgrid with flexible boundaries," *IET Generation, Transmission & Distribution*, vol. 14, no. 16, pp. 3161-3170, 2020.
- [10] M. E. Nassar and M. M. A. Salama, "Adaptive self-adequate microgrids using dynamic boundaries," *IEEE Transactions on Smart Grid*, vol. 7, no. 1, pp. 105-113, 2016.
- [11] C. Zhang, Y. Su, D. Li, L. Zhu, H. Yin, Y. Ma, I. Ray, F. Wang, L. M. Tolbert, and Y. Liu, "Real-time power management for microgrids with dynamic boundaries and multiple source locations," *IEEE Access*, vol. 10, pp. 84120-84134, 2022.
- [12] C. Zhang, M. Baldwin, H. Li, Z. Jiang, W. Wang, C. Zeng, C. Chen, H. Yin, and Y. Liu, "Appropriate evaluation of primary frequency response and its applications," in *Proc. 2023 IEEE PES GT&D Conference & Exposition*, Istanbul, Turkey, 2023, pp. 1-5.
- [13] C. Zhang, M. Baldwin, H. Li, Z. Jiang, W. Wang, C. Zeng, C. Chen, H. Yin, and Y. Liu, "Trends of inertia and primary frequency response in the Eastern Interconnection with field measurement data of FNET/GridEye," *IEEE Access*, 2023.
- [14] P. Kundur, N. J. Balu, and M. G. Lauby, *Power system stability and control*. McGraw-hill New York, 1994.
- [15] "Frequency response standard background document," NERC, 2012.
- [16] "Variable renewable generation can provide balancing control to the electric power system (fact sheet)," Office of Scientific and Technical Information (OSTI), 2013. [Online]. Available: <https://dx.doi.org/10.2172/1094877>
- [17] "Coal fleet transition: retirement impacts in the eastern interconnection," Department of Energy Office of Fossil Energy, 2015.
- [18] "Reliability guideline - primary frequency control," North American Electric Reliability Corporation, 2019.
- [19] M. J. Till, Y. Liu, Y. Liu, M. Patel, and T. King, "Frequency response of the Eastern Interconnection due to increased wind generation," in *Proc. 2014 IEEE PES General Meeting*, National Harbor,

- MD, USA, 2014, pp. 1-5.
- [20] G. Kou, Y. Liu, S. White, S. Hadley, and T. King, "Inertial response study on the year 2030 U.S. Eastern Interconnection (EI) high wind scenario," in *Proc. 2016 IEEE/PES Transmission and Distribution Conference and Exposition (T&D)*, Dallas, TX, USA, 2016, pp. 1-5.
- [21] Y. Liu, S. You, J. Tan, Y. Zhang, and Y. Liu, "Frequency response assessment and enhancement of the U.S. Power grids toward extra-high photovoltaic generation penetrations—an industry perspective," *IEEE Transactions on Power Systems*, vol. 33, no. 3, pp. 3438-3449, 2018.
- [22] S. You, Y. Liu, X. Zhang, M. T. Gonzalez, and Y. Liu, "U.S. Eastern Interconnection (EI) electromechanical wave propagation and the impact of high PV penetration on its speed," in *Proc. 2018 IEEE/PES Transmission and Distribution Conference and Exposition (T&D)*, Denver, CO, USA, 2018, pp. 1-5.
- [23] J. W. Ingleson and E. Allen, "Tracking the Eastern Interconnection frequency governing characteristic," in *Proc. IEEE PES General Meeting*, Minneapolis, MN, USA, 2010, pp. 1-6.
- [24] M. G. Lauby, J. J. Bian, S. Ekisheva, and M. Varghese, "Eastern interconnection frequency response trends," in *Proc. 2013 IEEE Power & Energy Society General Meeting*, Vancouver, BC, Canada, 2013, pp. 1-5.
- [25] M. G. Lauby, J. J. Bian, S. Ekisheva, and M. Varghese, "Frequency response assessment of Eastern and Western Interconnections," in *Proc. 2014 North American Power Symposium (NAPS)*, Pullman, WA, USA, 2014, pp. 1-5.
- [26] *Frequency Response Standard Background Document*, NERC, 2012.
- [27] R. J. Best, P. V. Brogan, and D. J. Morrow, "Power system inertia estimation using HVDC power perturbations," *IEEE Transactions on Power Systems*, vol. 36, no. 3, pp. 1890-1899, 2021.
- [28] J. Zhang and H. Xu, "Microperturbation method for power system online model identification," *IEEE Transactions on Industrial Informatics*, vol. 12, no. 3, pp. 1055-1063, 2016.
- [29] J. Zhang and H. Xu, "Online identification of power system equivalent inertia constant," *IEEE Transactions on Industrial Electronics*, vol. 64, no. 10, pp. 8098-8107, 2017.
- [30] N. Zhou, J. W. Pierre, and J. F. Hauer, "Initial results in power system identification from injected probing signals using a subspace method," *IEEE Transactions on Power Systems*, vol. 21, no. 3, pp. 1296-1302, 2006.
- [31] J. W. Pierre, D. Trudnowski, M. Donnelly, N. Zhou, F. K. Tuffner, and L. Dosiek, "Overview of system identification for power systems from measured responses," *IFAC Proceedings Volumes*, vol. 45, no. 16, pp. 989-1000, 2012.
- [32] F. Zeng, J. Zhang, G. Chen, Z. Wu, S. Huang, and Y. Liang, "Online estimation of power system inertia constant under normal operating conditions," *IEEE Access*, vol. 8, pp. 101426-101436, 2020.
- [33] F. Zeng, J. Zhang, Y. Zhou, and S. Qu, "Online identification of inertia distribution in normal operating power system," *IEEE Transactions on Power Systems*, vol. 35, no. 4, pp. 3301-3304, 2020.
- [34] A. Chakraborty, J. H. Chow, and A. Salazar, "A measurement-based framework for dynamic equivalencing of large power systems using wide-area phasor measurements," *IEEE Transactions on Smart Grid*, vol. 2, no. 1, pp. 68-81, 2011.
- [35] K. Tuttlberg, J. Kilter, D. Wilson, and K. Uhlen, "Estimation of power system inertia from ambient wide area measurements," *IEEE Transactions on Power Systems*, vol. 33, no. 6, pp. 7249-7257, 2018.
- [36] M. K. Erik Ørum, Minna Laasonen, Alf Ivar Bruseth, Erik Alexander Jansson, Anders Danell, Katherine Elkington, Niklas Modig, "Future system inertia," 2018. [Online]. Available: https://eepublicdownloads.entsoe.eu/clean-documents/Publications/SOC/Nordic/Nordic_report_Future_System_Inertia.pdf
- [37] Y. Bian, H. Wyman-Pain, F. Li, R. Bhakar, S. Mishra, and N. P. Padhy, "Demand Side Contributions for System Inertia in the GB Power System," *IEEE Transactions on Power Systems*, vol. 33, no. 4, pp. 3521-3530, 2018.
- [38] M. R. B. Tavakoli, M. Power, L. Ruttledge, and D. Flynn, "Load inertia estimation using white and grey-box estimators for power systems with high wind penetration," *IFAC Proceedings Volumes*, vol. 45, no. 21, pp. 399-404, 2012.
- [39] Y. Zhang, P. Markham, T. Xia, L. Chen, Y. Ye, Z. Wu, Z. Yuan, L. Wang, J. Bank, J. Burgett, R.

- W. Conners, and Y. Liu, "Wide-area frequency monitoring network (FNET) architecture and applications," *IEEE Transactions on Smart Grid*, vol. 1, no. 2, pp. 159-167, 2010.
- [40] Z. Zhian, X. Chunchun, B. J. Billian, Z. Li, S. J. S. Tsai, R. W. Conners, V. A. Centeno, A. G. Phadke, and L. Yilu, "Power system frequency monitoring network (FNET) implementation," *IEEE Transactions on Power Systems*, vol. 20, no. 4, pp. 1914-1921, 2005.
- [41] L. Wang, J. Burgett, J. Zuo, C. C. Xu, B. J. Billian, R. W. Conners, and Y. Liu, "Frequency disturbance recorder design and developments," in *Proc. 2007 IEEE Power Engineering Society General Meeting*, Tampa, FL, USA, 2007, pp. 1-7.
- [42] L. Zhan, Z. Jianyang, J. Culliss, Y. Liu, Y. Liu, and G. Shengyou, "Universal grid analyzer design and development," in *Proc. 2015 IEEE Power & Energy Society General Meeting*, Denver, CO, USA, 2015, pp. 1-5.
- [43] T. Xia, H. Zhang, R. Gardner, J. Bank, J. Dong, J. Zuo, Y. Liu, L. Beard, P. Hirsch, G. Zhang, and R. Dong, "Wide-area frequency based event location estimation," in *Proc. 2007 IEEE Power Engineering Society General Meeting*, Tampa, FL, USA, 2007, pp. 1-7.
- [44] W. Yao, S. You, W. Wang, X. Deng, Y. Li, L. Zhan, and Y. Liu, "A fast load control system based on mobile distribution-level phasor measurement unit," *IEEE Transactions on Smart Grid*, vol. 11, no. 1, pp. 895-904, 2020.
- [45] L. Zhu, W. Yu, Z. Jiang, C. Zhang, Y. Zhao, J. Dong, W. Wang, Y. Liu, E. Farantatos, D. Ramasubramanian, A. Arana, and R. Quint, "A comprehensive method to mitigate forced oscillations in large interconnected power grids," *IEEE Access*, vol. 9, pp. 22503-22515, 2021.
- [46] J. Guo, Y. Zhang, M. A. Young, M. J. Till, A. Dimitrovski, Y. Liu, P. Williging, and Y. Liu, "Design and implementation of a real-time off-grid operation detection tool from a wide-area measurements perspective," *IEEE Transactions on Smart Grid*, vol. 6, no. 4, pp. 2080-2087, 2015.
- [47] C. Zhang, Y. Zhao, L. Zhu, Y. Liu, E. Farantatos, M. Patel, H. Hooshyar, C. Pisani, R. Zaottini, and G. Giannuzzi, "Implementation and hardware-in-the-loop testing of a wide-area damping controller based on measurement-driven models," in *Proc. 2021 IEEE Power & Energy Society General Meeting (PESGM)*, Washington, DC, USA, 2021, pp. 1-5.
- [48] Y. Zhao, Y. Dong, L. Zhu, K. Sun, K. Alshuaibi, C. Zhang, Y. Liu, B. Graham, E. Farantatos, B. Marshall, M. Rahman, O. Adeuyi, S. Marshall, and I. L. Cowan, "Coordinated control of natural and sub-synchronous oscillations via HVDC links in Great Britain power system," in *Proc. 2022 IEEE/PES Transmission and Distribution Conference and Exposition (T&D)*, New Orleans, LA, USA, 2022, pp. 1-5.
- [49] R. M. Gardner and Y. Liu, "Generation-load mismatch detection and analysis," *IEEE Transactions on Smart Grid*, vol. 3, no. 1, pp. 105-112, 2012.
- [50] T. Xia, Y. Zhang, L. Chen, Z. Yuan, P. N. Markham, Y. Ye, and Y. Liu, "Phase angle-based power system inter-area oscillation detection and modal analysis," *European Transactions on Electrical Power*, vol. 21, no. 4, pp. 1629-1639, 2011.
- [51] Y. Dong, Y. Zhao, K. Alshuaibi, C. Zhang, Y. Liu, L. Zhu, E. Farantatos, K. Sun, B. Marshall, M. Rahman, O. Adeuyi, S. Marshall, and I. Cowan, "Adaptive power oscillation damping control via VSC-HVDC for the Great Britain power grid," in *Proc. 2023 IEEE Power & Energy Society Innovative Smart Grid Technologies Conference (ISGT)*, Washington, D.C., USA, 2023, pp. 1-5.
- [52] Y. Zhao, K. M. Alshuaibi, X. Jia, C. Zhang, Y. Liu, D. Ramasubramanian, L. Zhu, and E. Farantatos, "Comparison of wide-area and local power oscillation damping control through inverter-based resources," in *Proc. 2023 IEEE Power & Energy Society Innovative Smart Grid Technologies Conference (ISGT)*, Washington, D.C., USA, 2023, pp. 1-5.
- [53] L. Zhu, Y. Zhao, Y. Cui, S. You, W. Yu, S. Liu, H. Yin, C. Chen, Y. Wu, W. Qiu, M. Mandich, H. Li, A. Ademola, C. Zhang, C. Zeng, X. Jia, W. Wang, H. Yuan, H. Jiang, J. Tan, and Y. Liu, "Adding power of artificial intelligence to situational awareness of large interconnections dominated by inverter-based resources," *High Voltage*, vol. 6, no. 6, pp. 924-937, 2021.
- [54] Y. Zhao, S. You, M. Mandich, L. Zhu, C. Zhang, H. Li, Y. Su, C. Zeng, Y. Zhao, Y. Liu, H. Jiang, H. Yuan, Y. Zhang, and J. Tan, "Deep learning-based adaptive remedial action scheme with security margin for renewable-dominated power grids," *Energies*, vol. 14, no. 20, p. 6563, 2021.
- [55] S. Liu, S. You, H. Yin, Z. Lin, Y. Liu, W. Yao, and L. Sundaresh, "Model-free data authentication for cyber security in power systems," *IEEE Transactions on Smart Grid*, vol. 11, no. 5, pp. 4565-

- 4568, 2020.
- [56] H. Xiao, S. Fabus, Y. Su, S. You, Y. Zhao, H. Li, C. Zhang, Y. Liu, H. Yuan, Y. Zhang, and J. Tan, "Data-driven security assessment of power grids based on machine learning approach: Preprint," in *Proc. 2019 CIGRE Grid of the Future Symposium*, Atlanta, GA, USA, 2019, Research Org.: National Renewable Energy Lab. (NREL), Golden, CO (United States), Sponsor Org.: USDOE Office of Energy Efficiency and Renewable Energy (EERE), Renewable Power Office. Solar Energy Technologies Office.
- [57] Z. Jiang, N. Tong, Y. Liu, Y. Xue, and A. G. Tarditi, "Enhanced dynamic equivalent identification method of large-scale power systems using multiple events," *Electric Power Systems Research*, vol. 189, p. 106569, 2020.
- [58] Y. Cui, W. Wang, Y. Liu, P. Fuhr, and M. Morales-Rodriguez, "Spatio-temporal synchrophasor data characterization for mitigating false data injection in smart grids," in *Proc. 2019 IEEE Power & Energy Society General Meeting (PESGM)*, Atlanta, GA, USA, 2019, pp. 1-5.
- [59] L. Chen, M. A. Gandhi, J. W. Hurtt, P. Markham, Y. Zhang, and Y. Liu, "Island grid modeling and validation using single phase phasor measurement data," in *Proc. 2011 IEEE Power and Energy Society General Meeting*, Detroit, MI, USA, 2011, pp. 1-7.
- [60] NERC, "Essential Reliability Services Task Force Measures Framework Report," 2015. [Online]. Available: <https://www.nerc.com/comm/Other/essntlrbltysrvcstskfrclDL/ERSTF%20Framework%20Report%20-%20Final.pdf>
- [61] "Essential reliability services and the evolving bulk-power system - primary frequency response," Federal Energy Regulatory Commission (FERC), Washington, DC, USA, 2018.
- [62] "Wind explained - where wind power is harnessed," U.S. Energy Information Administration, March 30, 2022. [Online]. Available: <https://www.eia.gov/energyexplained/wind/where-wind-power-is-harnessed.php>
- [63] "Solar explained - where solar is found and used," U.S. Energy Information Administration, April 6, 2022. [Online]. Available: <https://www.eia.gov/energyexplained/solar/where-solar-is-found.php>
- [64] H. Weber and S. Al Ali, "Influence of huge renewable power production on inter-area oscillations in the European ENTSO-E-System," *IFAC-PapersOnLine*, vol. 49, no. 27, pp. 12-17, 2016.
- [65] M. Parsa and J. Toyoda, "Implementation of a hybrid power system stabilizer," *IEEE Transactions on Power Systems*, vol. 4, no. 4, pp. 1463-1469, 1989.
- [66] H. Quinot, H. Bourlès, and T. Margotin, "Robust coordinated AVR+PSS for damping large scale power systems," *IEEE Transactions on Power Systems*, vol. 14, pp. 1446-1451, 1999.
- [67] M. E. Aboul-Ela, A. A. Sallam, J. D. McCalley, and A. A. Fouad, "Damping controller design for power system oscillations using global signals," *IEEE Transactions on Power Systems*, vol. 11, no. 2, pp. 767-773, 1996.
- [68] V. Terzija, G. Valverde, D. Cai, P. Regulski, V. Madani, J. Fitch, S. Skok, M. M. Begovic, and A. Phadke, "Wide-area monitoring, protection, and control of future electric power networks," *Proceedings of the IEEE*, vol. 99, no. 1, pp. 80-93, 2011.
- [69] B. Pierre, F. Wilches-Bernal, D. Schoenwald, R. Elliott, D. Trudnowski, R. Byrne, and J. Neely, "Design of the pacific DC intertie wide area damping controller," in *Proc. 2020 IEEE Power & Energy Society General Meeting (PESGM)*, Montreal, QC, Canada, 2020, pp. 1-1.
- [70] W. Yao and L. Jiang, "Wide-area damping controller of FACTS devices for inter-area oscillations considering communication time delays," in *Proc. 2014 IEEE PES General Meeting | Conference & Exposition*, National Harbor, MD, USA, 2014, pp. 1-1.
- [71] Y. Zhao, L. Zhu, H. Xiao, Y. Liu, E. Farantatos, M. Patel, A. Darvishi, and B. Fardanesh, "An adaptive wide-area damping controller via FACTS for the new york state grid using a measurement-driven model," in *Proc. 2019 IEEE Power & Energy Society General Meeting (PESGM)*, Atlanta, GA, USA, 2019, pp. 1-5.
- [72] K. Sun, W. Qiu, Y. Dong, C. Zhang, H. Yin, W. Yao, and Y. Liu, "WAMS-based HVDC damping control for cyber attack defense," *IEEE Transactions on Power Systems*, pp. 1-1, 2022.
- [73] I. A. S. Altarjami, E. Farantatos, H. Hooshyar, Y. Liu, M. Patel, H. Xiao, C. Zhang, Y. Zhao, and L. Zhu, "Methods, systems, and computer program products for adaptive wide-area damping control using a transfer function model derived from measurements," ed: Google Patents, 2022.

- [74] "LabVIEW for CompactRIO developer's guide." National Instruments Inc. <https://www.ni.com/en-us/shop/compactrio/compactrio-developers-guide.html> (accessed July 8, 2022).
- [75] OPAL-RT, "OP5600 real-time simulator," 2022.
- [76] "CompactRIO module 9263." National Instruments. <https://www.ni.com/en-us/support/model.ni-9263.html> (accessed July 12, 2022).
- [77] C. Zhang, Y. Zhao, Y. Liu, L. Zhu, E. Farantatos, A. Haddadi, M. Patel, A. Darvishi, and H. Hooshyar, "Measurement-based voltage control coordinating inverter-based resources and traditional resources - New York State Grid case study," in *Proc. 2023 IEEE Power & Energy Society General Meeting (PESGM)*, Orlando, FL, USA, 2023, pp. 1-5.
- [78] B. K. Poolla, S. Bolognani, and F. Dörfler, "Optimal placement of virtual inertia in power grids," *IEEE Transactions on Automatic Control*, vol. 62, no. 12, pp. 6209-6220, 2017.
- [79] P. Du, N. V. Mago, W. Li, S. Sharma, Q. Hu, and T. Ding, "New ancillary service market for ERCOT," *IEEE Access*, vol. 8, pp. 178391-178401, 2020.
- [80] S. S. Guggilam, C. Zhao, E. Dall'Anese, Y. C. Chen, and S. V. Dhople, "Engineering inertial and primary-frequency response for distributed energy resources," in *Proc. 2017 IEEE 56th Annual Conference on Decision and Control (CDC)*, Melbourne, VIC, Australia, 2017, pp. 5112-5118.
- [81] "Fast frequency reserve - solution to the Nordic inertia challenge," European Network of Transmission System Operators for Electricity (ENTSOE), 2019.
- [82] Q. Hong, M. Nedd, S. Norris, I. Abdulhadi, M. Karimi, V. Terzija, B. Marshall, K. Bell, and C. Booth, "Fast frequency response for effective frequency control in power systems with low inertia," *The Journal of Engineering*, vol. 2019, no. 16, pp. 1696-1702, 2019.
- [83] S. Bolognani, R. Carli, G. Cavraro, and S. Zampieri, "Distributed reactive power feedback control for voltage regulation and loss minimization," *IEEE Transactions on Automatic Control*, vol. 60, no. 4, pp. 966-981, 2015.
- [84] H. Chen, T. Jiang, H. Yuan, H. Jia, L. Bai, and F. Li, "Wide-area measurement-based voltage stability sensitivity and its application in voltage control," *International Journal of Electrical Power & Energy Systems*, vol. 88, pp. 87-98, 2017.
- [85] "Introduction to OpenModelica." OpenModelica. <https://www.openmodelica.org/> (accessed 2022).
- [86] "DOE microgrid workshop summary report," U.S. Department of Energy Office of Electricity, 2012. [Online]. Available: <https://www.energy.gov/oe/downloads/2012-doe-microgrid-workshop-summary-report-september-2012>
- [87] S. Parhizi, H. Lotfi, A. Khodaei, and S. Bahramirad, "State of the art in research on microgrids: a review," *IEEE Access*, vol. 3, pp. 890-925, 2015.
- [88] Y. Kim, J. Wang, and X. Lu, "A framework for load service restoration using dynamic change in boundaries of advanced microgrids with synchronous-machine DGs," *IEEE Transactions on Smart Grid*, vol. 9, no. 4, pp. 3676-3690, 2018.
- [89] C. Chen, J. Wang, F. Qiu, and D. Zhao, "Resilient distribution system by microgrids formation after natural disasters," *IEEE Transactions on Smart Grid*, vol. 7, no. 2, pp. 958-966, 2016.
- [90] T. Zhao, B. Chen, S. Zhao, J. Wang, and X. Lu, "A flexible operation of distributed generation in distribution networks with dynamic boundaries," *IEEE Transactions on Power Systems*, vol. 35, no. 5, pp. 4127-4130, 2020.
- [91] Y. Du, X. Lu, J. Wang, and S. Lukic, "Distributed secondary control strategy for microgrid operation with dynamic boundaries," *IEEE Transactions on Smart Grid*, vol. 10, no. 5, pp. 5269-5282, 2019.
- [92] T. Zhao, J. Wang, and X. Lu, "An MPC-aided resilient operation of multi-microgrids with dynamic boundaries," *IEEE Transactions on Smart Grid*, vol. 12, no. 3, pp. 2125-2135, 2021.
- [93] Y. Du, H. Tu, X. Lu, J. Wang, and S. Lukic, "Black-start and service restoration in resilient distribution systems with dynamic microgrids," *IEEE Journal of Emerging and Selected Topics in Power Electronics*, pp. 1-1, 2021.
- [94] S. K. Mumbere, A. Fukuhara, Y. Sasaki, A. Bedawy, Y. Zoka, and N. Yorino, "Development of an energy management system tool for disaster resilience in islanded microgrid networks," in *Proc. 2021 20th International Symposium on Communications and Information Technologies (ISCIT)*, Tottori, Japan, 2021, pp. 97-100.
- [95] J. Dong, L. Zhu, Y. Su, Y. Ma, Y. Liu, F. Wang, L. M. Tolbert, J. Glass, and L. Bruce, "Battery and backup generator sizing for a resilient microgrid under stochastic extreme events," *IET Generation*,

- Transmission & Distribution*, vol. 12, no. 20, pp. 4443-4450, 2018.
- [96] X. Hu, T. Liu, Y. Ma, Y. Su, H. Yin, L. Zhu, F. Wang, L. M. Tolbert, and Y. Liu, "Two-stage EMS for distribution network under defensive islanding," *IET Generation, Transmission & Distribution*, vol. 13, no. 18, pp. 4073-4080, 2019.
- [97] Y. Ma, X. Hu, H. Yin, L. Zhu, Y. Su, F. Wang, L. M. Tolbert, and Y. Liu, "Real-time control and operation for a flexible microgrid with dynamic boundary," in *Proc. 2018 IEEE Energy Conversion Congress and Exposition (ECCE)*, Portland, OR, USA, 2018, pp. 5158-5163.
- [98] H. Yin, Y. Ma, L. Zhu, X. Hu, Y. Su, J. Glass, F. Wang, Y. Liu, and L. M. Tolbert, "Hierarchical control system for a flexible microgrid with dynamic boundary: design, implementation and testing," *IET Smart Grid*, vol. 2, no. 4, pp. 669-676, 2019.
- [99] M. Grami, M. Rekik, and L. Krichen, "A power management strategy for interconnected microgrids," in *Proc. 2020 20th International Conference on Sciences and Techniques of Automatic Control and Computer Engineering (STA)*, Monastir, Tunisia, 2020, pp. 213-218.
- [100] S. M. S. Hosseinimoghadam, H. Roghanian, M. Dashtdar, and S. M. Razavi, "Power-sharing control in an islanded microgrid using virtual impedance," in *Proc. 2020 8th International Conference on Smart Grid (icSmartGrid)*, Paris, France, 2020, pp. 73-77.
- [101] P. Lin, P. Wang, C. Jin, J. Xiao, X. Li, F. Guo, and C. Zhang, "A distributed power management strategy for multi-paralleled bidirectional interlinking converters in hybrid AC/DC microgrids," *IEEE Transactions on Smart Grid*, vol. 10, no. 5, pp. 5696-5711, 2019.
- [102] Z. Li, Z. Cheng, J. Si, and S. Li, "Distributed event-triggered hierarchical control to improve economic operation of hybrid AC/DC microgrids," *IEEE Transactions on Power Systems*, pp. 1-1, 2021.
- [103] L. Zhu, C. Zhang, H. Yin, D. Li, Y. Su, I. Ray, J. Dong, F. Wang, L. M. Tolbert, Y. Liu, Y. Ma, B. Rogers, J. Glass, L. Bruce, S. Delay, P. Gregory, M. Garcia-Sanz, and M. Marden, "A smart and flexible microgrid with a low-cost scalable open-source controller," *IEEE Access*, vol. 9, pp. 162214-162230, 2021.
- [104] F. Wang, D. Li, Y. Liu, Y. Ma, I. Ray, L. M. Tolbert, H. Yin, and L. Zhu, "Methods, systems, and computer readable media for protecting and controlling a microgrid with a dynamic boundary," Patent U.S. Patent 20200350761A1, 2020.
- [105] H. Yin, L. Zhu, Y. Ma, C. Zhang, Y. Su, D. Li, I. Ray, Y. Liu, F. Wang, and L. M. Tolbert, "Planned islanding algorithm design based on multiple sub-microgrids with dynamic boundary," *IEEE Open Access Journal of Power and Energy*, vol. 8, pp. 389-398, 2021.
- [106] H. Taha, *Operations research: an introduction*. Upper Saddle River, NJ, USA: Pearson, 2017.
- [107] S. Jahan and M. Hasan, "A comparative study on algorithms for shortest-route problem and some extensions," *Int. J. Basic Appl. Sci*, vol. 11, no. 6, pp. 167-177, 2011.
- [108] L. Yang, Y. Ma, J. Wang, J. Wang, X. Zhang, L. M. Tolbert, F. Wang, and K. Tomsovic, "Development of converter based reconfigurable power grid emulator," in *Proc. 2014 IEEE Energy Conversion Congress and Exposition (ECCE)*, Pittsburgh, PA, USA, 2014, pp. 3990-3997.
- [109] Y. Ma, J. Wang, F. Wang, and L. M. Tolbert, "Converter-based reconfigurable real-time electrical system emulation platform," *Chinese Journal of Electrical Engineering*, vol. 4, no. 1, pp. 20-27, 2018.
- [110] D. Li, Y. Ma, C. Zhang, H. Yin, I. Ray, Y. Su, L. Zhu, F. Wang, and L. M. Tolbert, "Development of a converter based microgrid test platform," in *Proc. 2019 IEEE Energy Conversion Congress and Exposition (ECCE)*, Baltimore, MD, USA, 2019, pp. 6294-6300.
- [111] D. Li, Y. Ma, C. Zhang, H. Yin, Y. Su, L. Zhu, F. Wang, and L. M. Tolbert, "A converter-based battery energy storage system emulator for the controller testing of a microgrid with dynamic boundaries and multiple source locations," in *Proc. 2022 IEEE Energy Conversion Congress and Exposition (ECCE)*, Detroit, MI, USA, 2022, pp. 1-8.

VITA

Chengwen Zhang received his B.S. and M.S. degrees from Huazhong University of Science and Technology, P. R. China, in 2015 and 2018, respectively. He started his Ph.D. study in August 2018 at the Center for Ultra-Wide-Area Resilient Electric Energy Transmission Networks (CURENT), the University of Tennessee, Knoxville. His research interests include microgrid operation and control, large-scale power system dynamics, data analytics, simulation, control, and protection.